UTS UNIVERSITY OF TECHNOLOGY SYDNEY

Equivalent Circuit Models of the Permanent Magnet Synchronous Motor with Predictable Core Loss

by Xin Ba

Thesis submitted in fulfilment of the requirements for the degree of

Doctor of Philosophy

under the supervision of Professor Youguang Guo and Professor Jianguo Zhu

University of Technology Sydney
Faculty of Engineering and Information Technology
School of Electrical and Data Engineering
May 2022

Title of the thesis:

Equivalent Circuit Models of the Permanent Magnet Synchronous Motor with Predictable Core Loss

Ph.D. candidate:

Xin Ba
Email: Xin.BA@student.uts.edu.au

Principal Supervisor:

Professor Youguang Guo
Email: youguang.guo-1@uts.edu.au

Co-Supervisor:

Professor Jianguo Zhu
Emails: jianguo.zhu@sydney.edu.au, jianguo.zhu@uts.edu.au

Address:
School of Electrical and Data Engineering
Faculty of Engineering and Information Technology
University of Technology Sydney, 15 Broadway, Ultimo, NSW 2007, Australia

CERTIFICATE OF ORIGINAL AUTHORSHIP

I, Xin Ba declare that this thesis, is submitted in fulfilment of the requirements for the award of Doctor of Philosophy, in the School of Electrical and Data Engineering, at the University of Technology Sydney.

This thesis is wholly my own work unless otherwise referenced or acknowledged. In addition, I certify that all information sources and literature used are indicated in the thesis.

This document has not been submitted for qualifications at any other academic institution.

This research is supported by the Australian Government Research Training Program.

Signature: Production Note:
Signature removed prior to publication.

Date: November 2022

ACKNOWLEDGMENT

First and foremost, I would like to express special appreciate and heart felt thanks to my supervisors, Professor Youguang Guo, Jianguo Zhu and Chengning Zhang, for the continuous support in my research. Their mentorship, guidance and sincere encouragement were invaluable throughout the Ph.D. study.

The gratitude also goes to staff of the school, Mr. Russell Nicholson, Mr. Brett Lowder, Dr. Mike Zhong, A/Prof. Peter Watterson and Dr. Zhenjie Gong for their technical support and my fellow group-mates for the invaluable suggestions.

I would like to acknowledge University of Technology Sydney, Chinese Scholarship Council and Beijing Institute of Technology for the financial assistance to my research.

Finally, I appreciate my family for their cooperations, inspirations and supports during the entire course of my Ph.D.

LIST OF PUBLICATIONS

The following articles were published during the thesis work.

Peer reviewed international journal publications:

[1] **X. Ba**, Y. Guo, J. Zhu, and C. Zhang, “An equivalent circuit model for predicting the core loss in a claw-pole permanent magnet motor with soft magnetic composite core,” *IEEE Trans. Magn.*, vol. 54, no. 11, article 8105506, 2018.

[2] **X. Ba**, P. Wang, C. Zhang, J. G. Zhu, and Y. Guo, "Improved deadbeat predictive current control to enhance the performance of the drive system of permanent magnet synchronous motors," *IEEE Tran. Appl. Supercond.*, vol. 31, no. 8, pp. 1-4, article 0603004, Nov. 2021.

[3] **X. Ba**, Z. Gong, Y. Guo, C. Zhang, and J. Zhu, “Development of equivalent circuit models of permanent magnet synchronous motors considering core loss,” *Energies*, vol. 15, no. 6, p. 1995, Mar. 2022.

[4] Z. Gong, C. Zhang, **X. Ba** and Y. Guo, "Improved deadbeat predictive current control of permanent magnet synchronous motor using a novel stator current and disturbance observer," *IEEE Access*, vol. 9, pp. 142815-142826, 2021.

[5] Z. Gong, **X. Ba**, C. Zhang, and Y. Guo, “Robust sliding mode control of the permanent magnet synchronous motor with an improved power reaching law,” *Energies*, vol. 15, no. 5, p. 1935, Mar. 2022.

[6] **X. Ba**, Z. Gong, Y. Guo, C. Zhang, and J. Zhu, “A generalized per-phase equivalent circuit model of the PMSM considering the core loss and magnetic saturation effect,” submitted to *IEEE Trans. Transportation Electrification*.

[7] L. Liu, **X. Ba**, Y. Guo, G. Lei, X. Sun, and J. Zhu, “Improved iron loss prediction models for interior PMSMs considering coupling effects of multiphysics factors,” submitted to *IEEE Trans. Transportation Electrification*.

ABSTRACT

The core loss modeling in the equivalent circuit and developing regulation methods of the core loss are among the key technologies to analyze the performance and improve the efficiency of the permanent magnet synchronous motor (PMSM). Nowadays, understanding, modeling, and regulating the core loss of the PMSM play increasing crucial roles when developing high-speed, high-efficiency, high-torque density and high-power density motors. Therefore, this thesis aims to develop generalized equivalent circuit models (ECMs) of the PMSM with the predictable core loss, including per-phase ECM and *d*- and *q*-axis ECMs. Firstly, the core loss with the 3-dimensional rotating magnetic field is investigated, and the method of how to model the core loss into the ECM is developed, in which the equivalent core loss resistance is modelled as a function of the motor speed to achieve high accuracy over the entire speed operating range, and then an attempt of adopting the proposed ECM in deadbeat predictive current control to improve the dynamic response and robustness of the PMSM drive system is made. Secondly, to further increase the core loss prediction accuracy especially in load conditions, a novel generalized per-phase ECM of the PMSM with predictable core loss is proposed. Experimental tests of the PMSM prototype suggest that the prediction precision of both the core loss and the output electromagnetic characteristic is effectively enhanced over the entire speed and torque operating range. Finally, novel generalized *d*- and *q*-axis ECMs of the PMSM with predictable core loss are established to benefit motor control and enable the core loss management. Moreover, to make the most use of the stator current and decrease the electromagnetic loss of the PMSM, an improved maximum torque per ampere current control considering both the core loss and copper loss is carried out theoretically. The research results of this thesis will improve the accuracy of the ECMs and mathematical models of the PMSM, and hence provide theoretical and technical support for the improvement of the optimization methods and control strategies of the PMSM.

Keyword: Equivalent circuit model, core loss, permanent magnet synchronous motor, motor control.

Content

LIST OF FIGURES

LIST OF TABLES

ABBREVIATIONS

1-D	One-dimensional
2-D	Two-dimensional
3-D	Three-dimensional
AC	Alternating current
DC	Direct current
DPCC	Deadbeat predictive current control
ECM	Equivalent circuit model
EMF	Electromotive force
EV	Electric vehicle
FEA	Finite element analysis
FEM	Finite element method
HEV	Hybrid electric vehicle
IEEE	Institute of electrical and electronics engineers
IPMSM	Interior permanent magnet synchronous motor
MPC	Model predictive controls
MTPA	Maximum torque per ampere
PI	Proportional integral
PM	Permanent magnet
PMSM	Permanent magnet synchronous motor
PWM	Pulse width modulation
RMS	Root mean square
SMC	Soft magnetic composite
SPMSM	Surface-mounted permanent magnet synchronous motor
SVPWM	Space vector pulse width modulation

TFSM	Transverse flux synchronous motor
UTS	University of Technology Sydney
VVVF	Variable voltage variable frequency

LIST OF SYMBOLS

A	Wire cross sectional area (m^2)
B	Magnetic flux density (T)
$\boldsymbol{B}$	Magnetic flux density vector (T)
b	Thickness of the electrical steel sheet (m)
B_m	Peak value of the magnetic flux density (T)
B_{maj}	Major axis of elliptical $\boldsymbol{B}$ (T)
B_{min}	Minor axis of elliptical $\boldsymbol{B}$ (T)
B_r	Radial magnetic flux density (T)
B_z	Axial magnetic flux density (T)
B_θ	Circumferential magnetic flux density (T)
C_{aa}	Coefficient of the alternating anomalous loss
C_{ar}	Coefficient of the rotating anomalous loss
C_e	Coefficient of the eddy current loss
C_{ea}	Coefficient of the alternating eddy current loss
C_{er}	Coefficient of the rotating eddy current loss
C_{ha}	Coefficient of the alternating hysteresis loss
E_0	Back EMF of per-phase (V)
f	Flux density frequency (Hz)
h	Coefficient of the alternating hysteresis loss
H	Magnetic field strength (A/m)
$\boldsymbol{H}$	Magnetic field strength vector (A/m)
$\boldsymbol{H_1}$	Fundamental component of magnetic field strength vector (A/m)
H_{1maj}	Major axis of elliptical $\boldsymbol{H_1}$ (A/m)
H_{1min}	Minor axis of elliptical $\boldsymbol{H_1}$ (A/m)

* Symbols that are not listed are explained where they firstly appear

I_p	Phase current (A)
K_i	Integral coefficient
K_p	Proportion coefficient
k_{wa}	Winding factor of the phase winding
l	Total stator wire length (m)
L_{AA}	Self-inductance of phase A (H)
$L_{AB} = L_{BA}$	Mutual inductances of phase A and B (H)
$L_{AC} = L_{CA}$	Mutual inductances of phase A and C (H)
L_{BB}	Self-inductance of phase B (H)
$L_{BC} = L_{CB}$	Mutual inductances of phase B and C (H)
L_{CC}	Self-inductance of phase C (H)
L_d	*d*-axis inductance (H)
L_q	*q*-axis inductance (H)
L_s	Synchronous inductance (H)
N	Number of turns of the stator winding
n	Motor speed (r/min)
n_p	Number of phases
P_a	Alternating core loss (W)
P_{aa}	Alternating anomalous loss (W)
P_{ar}	Rotating anomalous loss (W)
P_{ea}	Alternating eddy current loss (W)
P_{em}	Electromagnetic power (W)
P_{er}	Rotating eddy current loss (W)
P_{ha}	Alternating hysteresis loss (W)
P_{hr}	Rotating hysteresis loss (W)
P_{in}	Input power (W)

P_{out}	Output power (W)
P_r	Rotating core loss (W)
R_{an}	Equivalent anomalous loss resistance at no-load conditions (Ω)
R_c	Equivalent core loss resistance (Ω)
R_e	Equivalent eddy current loss resistance at no-load conditions (Ω)
R_h	Equivalent hysteresis loss resistance at no-load conditions (Ω)
R_i	Equivalent core loss resistance at load conditions (Ω)
R_s	Stator winding resistance of one phase (Ω)
T	Time period (s)
T_{em}	Electromagnetic torque (Nm)
V_p	Phase voltage (V)
W_c	Magnetic co-energy (J)
X_s	Synchronous reactance (Ω)
η	Efficiency (%)
λ_f	Flux linkage of PMs (Wb)
ρ	Electrical resistivity of the stator winding (Ω·m)
ρ_m	Mass density of material (kg/m^3)
σ	Conductivity ($\Omega^{-1}\cdot m^{-1}$)
χ	Lagrange multiplier
ω_e	Rotor speed in electrical angular frequency (rad/s)
ω_m	Rotor speed in mechanical angular frequency (rad/s)

CHAPTER 1. INTRODUCTION

1.1 Background of the Research

Permanent magnet (PM) synchronous motor (PMSM) is a kind of synchronous motor with permanent magnets to provide the field excitation. Thus, the PMSM does not need a DC source for excitation, resulting in low copper loss, high reliability, high power density and torque density. Consequently, PMSMs have been widely used in industrial applications, such as the auxiliary power unit, solar power, medical instruments, robotic arms, electrical tools and so on [1-4]. Recently, the surge in demand for highly efficient PMSMs is mainly caused by electric vehicles (EVs) and hybrid electric vehicles (HEVs) [5-9]. The research hotspots of the PMSM may move toward high speed/power density, high torque density and high efficiency, and to achieve these goals, the core loss in the PMSM has to be appropriately calculated, modelled, and controlled.

The core loss which is caused by the motion of magnetic domain walls inside the magnetic materials is one of the main parts of the electromagnetic loss of the PMSM. Traditionally, the core loss is regarded to be a small part of the total loss compared with the copper loss. Therefore, the most common practice is to roughly estimate the core loss in the motor design and ignore the core loss in the motor control directly. However, the core loss is increasing with the motor speed and stator current, and it may even exceed the copper loss in the medium and high speed ranges. Thus, comprehensively understanding, modelling, optimising, and managing the core loss are necessary for the modern high-performance PMSM development.

The equivalent circuit models (ECMs) are the key to the PMSM. Specifically, the ECMs are the mathematical models of the PMSM in terms of the physical meaning, but they have different expressions. The ECM is able to provide a straightforward and clear expression of the energy conversion during the motor operation. For example, the power loss of the stator winding, the copper loss, is represented by resistance, while the magnetic energy stored in the stator winding is depicted by inductance. Although the structure of the ECM looks simple, it can achieve versatile performance evaluations with fast calculation and small amount of calculation burden, including input power, output

power/torque, efficiency, power factor, etc. In conclusion, the ECMs or mathematical models underpin the motor design, optimization, and control; therefore, any improvement in ECM can benefit all related areas of the PMSM. However, in the conventional ECM of the PMSM, the core loss is neglected, resulting in insufficient accuracy in motor performance predictions.

The mechanism of the core loss, especially the rotating core loss has not been fully understood until now; thus, the accurate core loss modelling with the rotating magnetic field deserves to be studied systematically. Generally, the research results of the core loss are displayed by a series of complex mathematical formulas, which are acceptable in motor design and optimization but hard to insert into the motor control and extend in engineering practical applications. However, the ECM is the bridge to solve the above difficulties. Modelling the core loss into the ECMs is the most effective way to expand applications in almost every related topic of the motor. Although many researchers have realized the importance of the core loss, the generalized ECMs of the PMSM with predictable core loss are still underdeveloped during the past decades. There are two crucial points in developing the ECM:

(1) Where the equivalent core loss resistance should be put, i.e., which branch the equivalent core loss resistance should be connected to predict the core loss in both no-load and loading conditions.

(2) How to identify the value of the equivalent core loss resistance, i.e., it should be a constant or a function of motor parameters.

Therefore, this thesis is devoted to establishing ECMs of the PMSM with predictable core loss, and exploring applications of the proposed ECMs for improving the performance of the motor design, optimization and control.

1.2 Research Gaps

In most cases, i.e., in conventional ECMs or mathematical models of the PMSM, the core loss is ignored, leading to some defects in the application, including insufficient support in core loss estimation, efficiency prediction, thermal calculation, electromagnetic torque computation, parameter sensitivity in the motor control, etc.

Although some scholars have engaged in core loss modelling in the ECM, there are still issues that need to be improved. In [10, 11], a single-valued equivalent resistance was adopted to represent the core loss of the PMSM in the per-phase ECM. In [12-17], two single-valued equivalent resistances were used to represent the core loss in *d*- and *q*-axis ECMs of the PMSM, respectively. However, nowadays PMSMs are also widely used in speed-varying situations, and the single-valued equivalent resistance model cannot correctly predict the core loss in a wide speed range. In order to express the core loss changes with the terminal voltage and current of the PMSM, [18, 19] incorporated two single-valued equivalent resistances to describe the voltage-dependent core loss and stator current-related core loss in the per-phase ECM, respectively. However, the impact of the magnetic saturation effect on the core loss is neglected. In [20], the authors of this thesis modelled the core loss of the PMSM in the per-phase ECM via a variable equivalent resistance, which is a function of the motor speed. This method achieves high performance prediction accuracy in a wide speed range, but the performance prediction error will increase when the motor operates at load, i.e., with large stator currents.

As for the equivalent core loss resistance identification in ECMs, there are two categories of methods, i.e., the finite element method and experimental tests. However, in the finite element methods in the previous studies of the equivalent core loss resistance identification [12, 21, 22], only the alternating core loss is taken into account, but more than 50% of the core loss in the PMSM is the rotating core loss, and hence the accuracy of the equivalent resistance is suffered. On the other hand, most researchers selected the core loss test result at the no-load condition with rated speed to fit the equivalent core loss resistance [11, 23, 24]. Actually, the core loss is sensitive to the motor speed and current, and the core loss at one point is hard to represent the core loss in the whole operation range. Moreover, until recently the measured core loss in both no-load and various loading conditions has not been reported systematically. Therefore, the equivalent core loss resistance identification methods need to be significantly improved.

In the last decades, model predictive controls (MPCs) have become hotspots of academic research and industrial application since they can provide superior dynamic and steady-state characteristics. In MPCs, ECMs of the PMSM, also known as the predictive model, are the essence for the further behaviour prediction of the control variables, such as the *q*-axis current. In other words, the accuracy of the ECM determines the accuracy of the

control variables. However, almost no record has adopted the core loss predictable ECM of the PMSM in MPCs to enhance prediction performance.

The original intention of the maximum torque per ampere (MTPA) current control is to decrease the copper loss for a given output electromagnetic torque. Due to the existence of the non-negligible core loss, the calculated current in the traditional MTPA deviates from the actual value. Therefore, the improved MPTA considering both the copper loss and core loss is needed to make the most use of the stator current.

1.3 Research Objectives

Based on the above-mentioned research background and research gaps, the main objectives of the study are as follows:

1. To fully understand the core loss with the alternating and rotating magnetic fields, as well as the relationship between the magnetic circuit and electrical circuit, and then model the core loss of the PMSM in equivalent circuit models.
2. To comprehensively explore the influencing factors of the core loss, and then develop generalized ECMs of the PMSM with the predictable core loss, including the per-phase ECM and *d*- and *q*-axis ECMs.
3. Experimental/simulated comparisons are carried out to evaluate the performance of the proposed ECMs not only in the core loss prediction but also in output characteristic predictions.
4. To improve the accuracy of the predictive model in the model predictive control of the PMSM, enhanced deadbeat predictive current control which involves the proposed ECM is developed.
5. To make the most use of the stator current and narrow the gap between the calculated current and the actual current, a modified maximum torque per ampere current control considering both the copper loss and core loss is constructed.

1.4 Contributions of the Research

Based on the above-mentioned research gaps and objectives, the contributions of this thesis are discussed below.

1. A novel equivalent core loss resistance identification method is proposed, whereby the 3-D rotating core loss in a wide speed range can be predicted accurately.

2. An improved deadbeat predictive current control with the ECM with predictable core loss is designed, and then the dynamic speed response and the torque robustness of the drive system are enhanced effectively.

3. A generalized per-phase ECM considering the core loss and magnetic saturation effect is proposed, resulting in higher prediction accuracy in both core loss and mechanical characteristics compared with traditional ones.

4. Generalized *d*- and *q*-axis ECMs with predictable core loss are established, which benefit the motor control by providing high-precision solutions in wide speed and torque ranges.

5. A novel maximum torque per ampere current control considering both the core loss and copper loss is illustrated to make the most use of the armature currents and improve the efficiency of the PMSM.

1.5 Thesis Outline

This thesis consists of six chapters where each chapter contains different contents of the research. Short descriptions of each chapter are discussed as follows:

Chapter 1 presents the background of the study which directs scopes of the study. In addition, the contributions of the research are included in this chapter. Moreover, the chapter presents outline of the thesis.

Chapter 2 gives the literature survey on previous works which are related with this study. The chapter includes the conventional ECMs, per-phase ECMs with predictable core loss, and *d*- and *q*-axis ECMs with predictable core loss in previous studies, as well as comparisons of them and some error corrections are presented. In addition, the core loss measurement techniques in terms of separation method and direct measurement methods are reviewed in this chapter.

In chapter 3, taking a claw pole PMSM with the soft magnetic composite as the example, a comprehensive analysis of the 3-dimensional rotating magnetic fields is illustrated, and hence the core loss mathematical models with the 3-dimensional rotating magnetic fields are established. Then, the detailed method of modelling the core loss in the equivalent circuit model is reported, and the identification methods of the equivalent core loss resistance, as well as other parameters in the circuit model, are discussed. Experimental tests of the claw pole PMSM verify the effectiveness of the proposed circuit model and the equivalent core loss resistance identification methods. Finally, an extended exploration of the proposed equivalent circuit model with predictable core loss in the model predictive control of the PMSM is carried out, and simulation experiments suggest that it has better dynamic performance than the traditional predictive model.

To further improve the accuracy of the circuit model in wide speed and current ranges, a generalized per-phase equivalent circuit model of the PMSM with predictable core loss is developed in chapter 4. Firstly, the limitation of the previous circuit model of core loss with large current/torque is analysed. Then, the improved generalized per-phase equivalent circuit model of the core loss considering the magnetic saturation effect, as well as the equivalent core loss resistances determination methods are established. Finally, performance comparisons of three kinds of equivalent circuit models with predictable core loss and the traditional circuit model which ignores the core loss are made. Experimental tests indicate that the proposed method is not only able to predict the core loss in both no-load and load conditions accurately but also can predict the motor output performance with the highest precision compared with its counterparts.

In motor control, the *d*- and *q*-axis equivalent circuit models are widely used since they are the foundation of the field oriented control. Therefore, chapter 5 explores the *d*- and *q*-axis equivalent circuit models of the PMSM with predictable core loss. Due to the salient effect, the *d*-axis inductance is smaller than the *q*-axis inductance in the interior PMSM, which makes this prototype suitable for validating the *d*- and *q*-axis equivalent circuit models. Firstly, the electromagnetic parameters of the interior PMSM are analysed by the finite element method. Then, the *d*- and *q*-axis equivalent circuit models considering both the core loss and the magnetic saturation effect are carried out. Finally, to accurately make the most use of the stator currents, an improved maximum torque per ampere current control, which incorporates both the core loss and copper loss, is proposed.

Chapter 6 presents the conclusion of this thesis. Possible future works are also included in this chapter.

CHAPTER 2. LITERATURE REVIEW

2.1 Introduction

Since electrical motors transform two thirds of industrial electric energy, one of the aims of electric device design and drive is to save energy and achieve high efficiency over a broad torque and speed range, especially in the applications where the motor is supplied by power limited batteries. Higher efficiency of electromagnetic devices means lower loss, whilst understanding and modelling all kinds of electromagnetic loss correctly are the basis of the loss minimization design and control strategies. In electrical machines, generally, there are three main types of loss, i.e., copper loss, core loss, and mechanical loss. The mechanical loss, also called friction and windage loss, is caused by the friction among mechanical parts and air. The physical size of the rotor, interfaces of rotor and stator, and the angular velocity of the rotor are the main factors affecting the value of the mechanical loss [25, 26]. The coil resistance is the main reason for the copper loss, and the copper loss is the principal loss in the machine under most operating conditions [27]. The core loss is caused by the motion of magnetic domain walls inside the magnetic materials, and increases with the motor speed and current. Undoubtedly, the core loss of PMSMs needs to be precisely calculated for high-performance design and control strategies.

The equivalent circuit model (ECM) is a widely used method for electric machine analysis because it provides good analysis results with fast calculation. By analysing the equivalent circuit model of the electrical machine, the machine performance and parameters, such as the relationship among currents and voltages, input power, output power, as well as the efficiency and power factor, can be calculated efficiently. Consequently, the equivalent circuit model lays the foundation of the electric machine control algorithms. However, in the conventional equivalent circuit model of electrical machines, the copper loss is modelled as a stator winding resistance, while the core loss of stator core material is neglected. Recently, increasing emphases have been put on the accuracy of torque control algorithm, loss minimization control algorithm, and high-speed motor control algorithm, resulting in the need to add the core loss component when modelling the equivalent circuit of electric machines. Thus, in this chapter, a review of

ECMs considering the core loss is established for both 3-phase stationary reference frame and 2-phase rotary reference frame.

The properties of core material are usually obtained from standard Epstein tests on samples that have undergone different treatments together with stress released annealing. The mechanical stress [28], heat treatment processes [29], and the assembly effects (clamping and welding) [30] on the stator core can increase the core loss of the electrical machines. Besides, the measurement of the core loss of PMSMs shows more challenges since one cannot “turn on” or “turn off” the flux linkage generated by the permanent magnets. Therefore, a review of core loss measurement methods of the PMSM is also presented in this chapter.

2.2 Prototypes and the Conventional ECMs of PMSMs

There are various types of PMSM prototypes, such as the surface-mounted PMSM [31], interior PMSM [32], claw-pole PMSM [33], transverse flux PMSM [34], and axial flux PMSM [35], as shown in Fig. 2-1. The structures of the prototypes show significant difference, but their operating principle in terms of electromagnetic energy conversion is same. Therefore, it is fundamental to extract the key electromagnetic parameters of the PMSM and present them in an ECM or mathematical equations to conduct motor performance analysis, control and optimization.

(a)

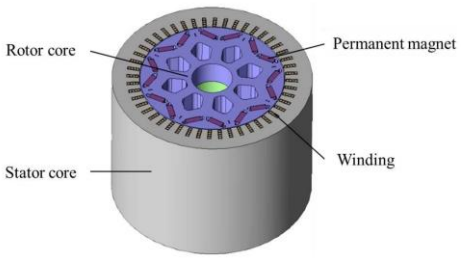

(b)

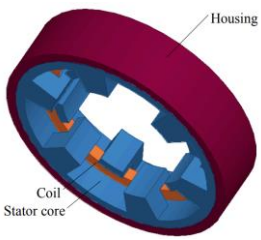

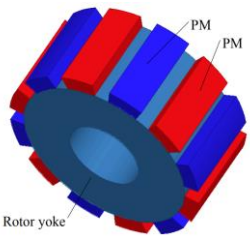

(c)

(d)

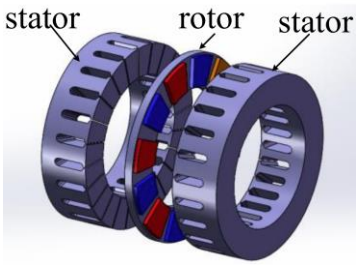

(e)

Fig. 2-1 Prototypes of the PMSM: (a) surface-mounted PMSM [31]; (b) interior PMSM [32]; (c) claw-pole PMSM [33]; (d) transverse flux PMSM [34]; (e) axial flux PMSM [35].

In the most studied cases of the PMSM, the per-phase ECM neglecting the core loss is illustrated in Fig. 2-2, while the *d*- and *q*-axis ECMs are demonstrated in Fig. 2-3. In Fig. 2-2, R_s is the winding resistance of per-phase, and the power loss of R_s presents the copper loss of the PMSM. L_s is the synchronous inductance, which is an equivalent inductance of self-inductance and mutual-inductance per phase. The PMSM is excited by PMs, and the PM flux is described by λ_f, while rotating PMs induce the back electromotive force E_0 in the phase winding, which is proportional to the rotor speed in electrical angular frequency, ω_e. Moreover, I_p and V_p are the phase current and voltage, respectively. To realize the vector control of the PMSM, ECM or mathematical model in the three-phase stationary reference frame needs to be transformed to the two-phase rotational reference frame, as shown in Fig. 2-3, where V_d and V_q are the *d*- and *q*-axis terminal voltages, I_d and I_q are the *d*- and *q*-axis armature currents, and L_d and L_q are the *d*- and *q*-axis inductances, respectively.

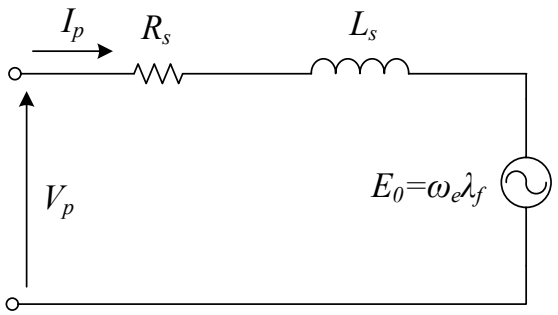

Fig. 2-2 Conventional per-phase ECM of PMSM.

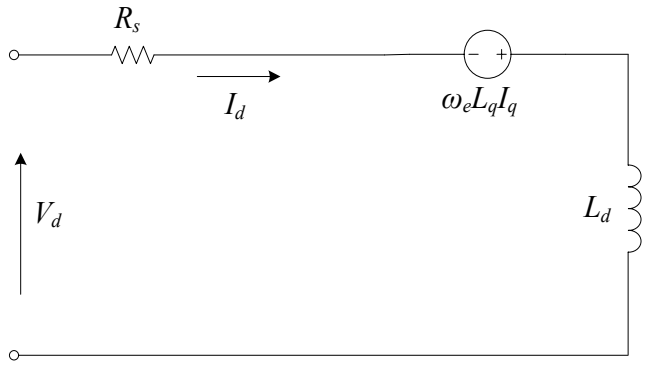

(a)

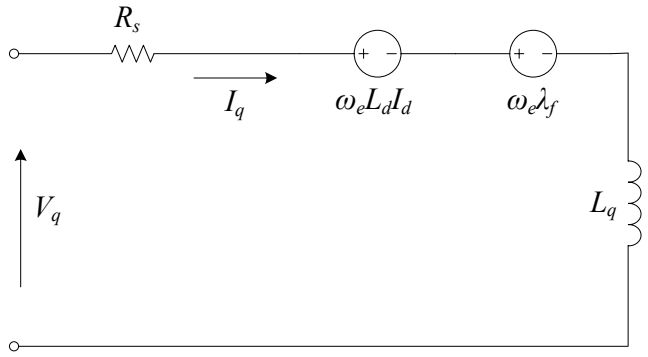

(b)

Fig. 2-3 Conventional *d* and *q* axis ECMs of PMSM: (a) *d*-axis; (b) *q*-axis.

The mathematical models of Figs. 2 and 3 can be written as follows

$$\boldsymbol{V_p} = \boldsymbol{E_0} + (R_s + \mathrm{j}\omega_e L_s)\boldsymbol{I_p} \tag{2.1}$$

$$\begin{bmatrix} V_d \\ V_q \end{bmatrix} = R_s \begin{bmatrix} I_d \\ I_q \end{bmatrix} + p \begin{bmatrix} L_d & 0 \\ 0 & L_q \end{bmatrix} \begin{bmatrix} I_d \\ I_q \end{bmatrix} + \begin{bmatrix} 0 & -\omega_e L_q \\ \omega_e L_d & 0 \end{bmatrix} \begin{bmatrix} I_d \\ I_q \end{bmatrix} + \begin{bmatrix} 0 \\ \omega_e \lambda_f \end{bmatrix} \tag{2.2}$$

The ECMs and mathematical models mentioned above cannot provide high-precision solutions during motor design, control and optimization due to the absence of the core loss. The copper loss can be estimated via the power loss in winding resistance R_s, while the core loss cannot be predicted from any parameters in these models. Actually, the core loss may rise significantly and exceed the copper loss when the motor speed increases and the load torque grows. Ignoring the core loss also leads to underestimation of other performance.

In conclusion, due to the neglecting of core loss component, the drawbacks of the conventional ECMs of the PMSM mainly contain:

(1) Inconvenience for core loss calculation, control, and optimization;
(2) Poor theoretical foundation to support the motor efficiency prediction, thermal management, and cooling design;
(3) Overestimation of the output electromagnetic torque and power for a given input current, resulting in lower control performance; and
(4) Exacerbation of the parameter sensitivity of the model-based motor control system, such as the model predictive control.

Therefore, further studying and establishing the ECM of the PMSM with predictable core loss has vitally important theoretical significance and engineering value.

2.3 Per-phase ECM with Predictable Core Loss

Due to the complex mechanism, the core loss modelling in the ECM is still a pending issue. Although incorporating the core loss in ECM is important, only a small amount of research works have been carried out in this area, and most of them were in the 1980s. This section and the next are to investigate the main publications with various topologies of ECM of PMSMs with predictable core loss, and all the ECMs describe the permanent magnet synchronous machine working as motor.

The earliest record of the ECM of PMSMs with predictable core loss may be in 1980 [10], when Honsinger reported an ECM of AC permanent magnet machines, as illustrated in Fig. 2-4. Strictly speaking, the core loss is comprised of three components: hysteresis loss, eddy current loss, and anomalous loss or excess loss. However, a considerable number of researchers divided the core loss just into two parts: hysteresis loss and eddy current loss. The eddy current loss simply varies with the square of the terminal voltage, whereas the empirical index for the hysteresis loss is in the range of 1.6-1.9 and that for the anomalous loss is 1.5. For different types of cores, these three components account for various proportions, e.g., in soft magnetic composite and amorphous magnetic alloy core, the hysteresis loss may be the dominant part, while in silicon steel core, the major component may be the eddy current loss. In a permanent magnet machine, the core loss appears due to the magnetizing flux and leakage flux, and the core loss caused by the leakage flux can

be neglected, especially under no-load condition. At fixed speed and frequency, the core loss can be considered approximately proportional to the square of magnetic flux or back electromotive force (EMF), one has

$$P_c \approx k_c E_i^2 \tag{2.3}$$

where k_c is a constant. Therefore, the equivalent core loss may be represented by a resistance in parallel with the magnetizing branch. As shown in Fig. 2-4, the core loss in the stator core is considered by a power loss consumed in an equivalent core loss resistance r_c placed across the internal voltage E_i. It is noted that the impedance Z_i may contain the synchronous inductance, as well as the distributed capacitance.

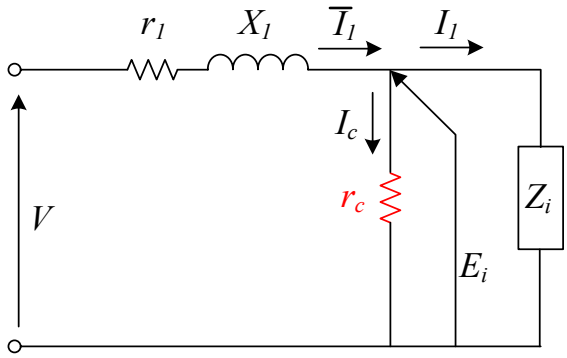

Fig. 2-4 Per-phase ECM with predictable core loss of PMSMs [10].

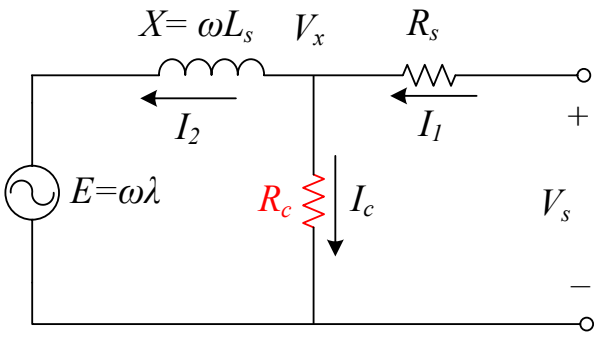

Fig. 2-5 Per-phase ECM with predictable core loss of PMSMs [11].

Fig. 2-5 proposed the most widely used per-phase ECM of PMSMs with predictable core loss, and this topology was first introduced by Colby and Novotny in 1987 [11]. The key to using ECM to predict the core loss of PMSMs is how to identify the value of the equivalent core loss resistance R_c, and a more accurate value of R_c can bring a better

analysis solution of PMSMs performance. In Colby and Novotny's original work, the equivalent core loss resistance R_c is modelled as a single-valued resistance, and it was evaluated by measuring the torque required to drive the PMSM as a generator at no load conditions.

However, the core loss is frequency dependent, i.e., the core loss varies with the motor speed, so the single-valued equivalent core loss resistance is insufficient to describe the whole speed range of the PMSM. To deal with this problem, the authors of this paper presented an ECM with variable core loss resistance as shown in Fig. 2-6 [20]. The model was used to analyse a permanent magnet motor with soft magnetic composite core, in which the hysteresis loss dominates, and reasonably accurate results were obtained.

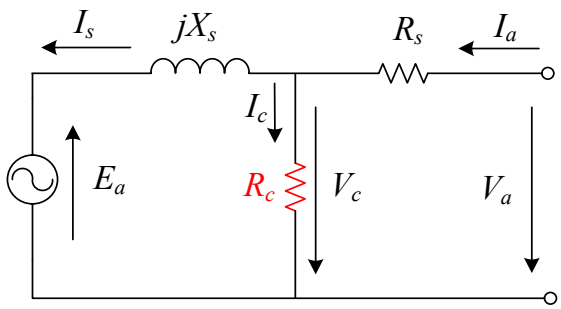

Fig. 2-6 ECM of PMSM with R_c as function of speed [20].

In order to express the core loss changes with the terminal voltage and current of the interior permanent magnet synchronous motor (IPMSM), Consoli and Renna [18] established an ECM with two equivalent core loss resistance, i.e., R_{c1} and R_{c2}, as illustrated in Fig. 2-7. The resistance R_{c2}, conventionally placed in parallel with the internal EMF of the motor, accounts for the small power which is lost in the motor at the no-load condition. This resistance is calculated through the values of voltage and current at this point and accounts for the voltage dependent core loss of the machine. On the other hand, R_{c1} is included which carries part of the input current to model the core loss component relevant to the stator current. Additionally, the *d*-axis inductance is different from the *q*-axis inductance in the IPMSM, and hence two parameters R and X are incorporated to represent the saliency of the motor, and $R=(X_d-X_q)\sin\gamma\cos\gamma$, $X=(X_d-X_q)\sin 2\gamma$, while γ is the reaction angle and X_d are X_q the *d*-axis and *q*-axis reactance, respectively. For the surface-mounted permanent magnet synchronous motor (SPMSM), $X_d=X_q$, and R and X are zero and the ECM as shown in Fig. 2-7 can also be adopted.

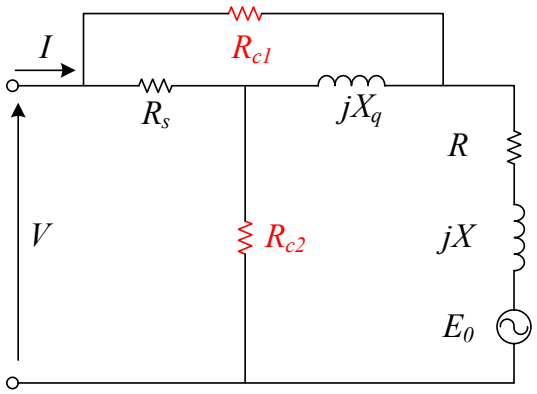

Fig. 2-7 Per-phase ECM with predictable core loss of PMSMs [18].

As a further step of Fig. 2-7, Consoli and Raciti [19] developed the ECM of PMSMs with salient-pole, as shown in Fig. 2-8. In this ECM, both the core loss and the saliency effects of the machine are taken into account by introducing parameters R_{cv}, R_{ci}, R, and X. To be more specific, the equivalent resistance R_{cv}, placed in parallel with the total voltage induced in the stator winding, accounts for the voltage-dependent core loss, while the equivalent resistance R_{ci}, carrying part of the phase stator current, accounts for the current-related core loss. The resistance R and the reactance X are introduced to describe the saliency effects of the machine, and they are zero when the machine has no saliency. Circuit parameter determination relies on experimental tests on the machine, and no-load as well as loaded conditions are analyzed. The main difference between Figs. 2-7 and 2-8 is where to place the equivalent current-related core loss resistance, and there is only slight difference for the results.

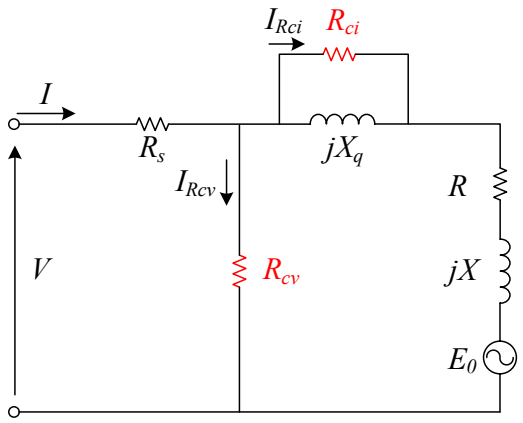

Fig. 2-8 Per-phase ECM with predictable core loss of PMSMs [19].

2.4 *d*- and *q*-axis ECM of PMSM with Predictable Core Loss

The most widely used ECM of PMSMs based on the synchronous *d*-*q* reference frame considering the core loss is presented in Fig. 2-9 [12-17]. In the figure, the equivalent core loss resistance R_c connected in parallel with the *d*- and *q*-axis magnetizing branch, respectively. Essentially, Fig. 2-9 can be regarded as the equivalent ECM of Fig. 2-2 after applying reference frame transformation.

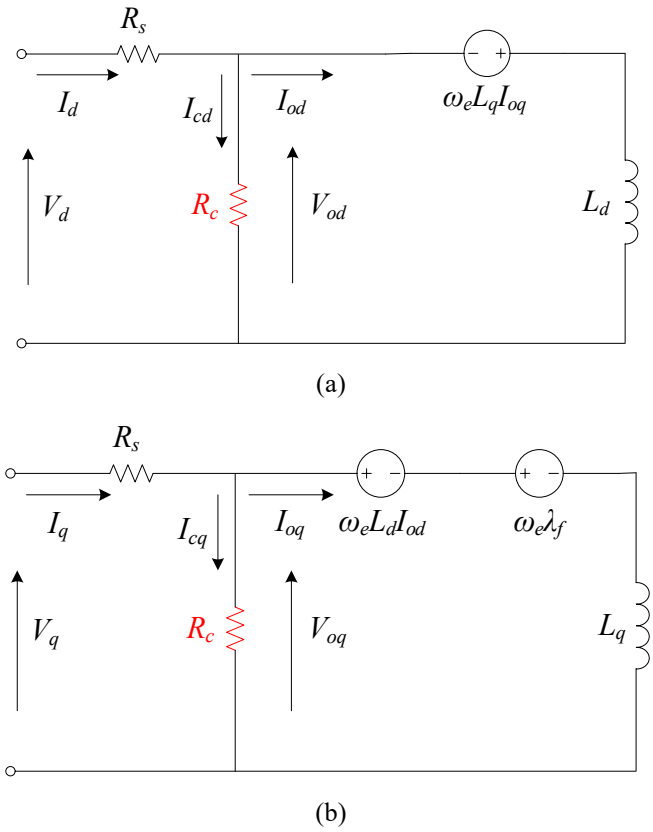

Fig. 2-9 ECM of PMSMs with predictable core loss: (a) *d*-axis; (b) *q*-axis.

Fig. 2-9 shows the most popular ECM of the PMSM, but its mathematical equations corresponding to the circuit model have some errors in [12-16]. Here, the mathematical models are modified as

$$\begin{bmatrix} V_d \\ V_q \end{bmatrix} = R_s \begin{bmatrix} I_{od} \\ I_{oq} \end{bmatrix} + (1 + \frac{R_s}{R_c}) \begin{bmatrix} V_{od} \\ V_{oq} \end{bmatrix} \tag{2.4}$$

$$\begin{bmatrix} V_{od} \\ V_{oq} \end{bmatrix} = \begin{bmatrix} 0 & -\omega_e L_q \\ \omega_e L_d & 0 \end{bmatrix} \begin{bmatrix} I_{od} \\ I_{oq} \end{bmatrix} + \begin{bmatrix} 0 \\ \omega_e \lambda_f \end{bmatrix} + p \begin{bmatrix} L_d & 0 \\ 0 & L_q \end{bmatrix} \begin{bmatrix} I_{od} \\ I_{oq} \end{bmatrix} \tag{2.5}$$

$$\begin{bmatrix} I_{od} \\ I_{oq} \end{bmatrix} = \begin{bmatrix} I_d \\ I_q \end{bmatrix} - \begin{bmatrix} I_{cd} \\ I_{cq} \end{bmatrix} \tag{2.6}$$

$$\begin{bmatrix} I_{cd} \\ I_{cq} \end{bmatrix} = \begin{bmatrix} -\omega_e L_q I_{oq} / R_c \\ \omega_e (L_d I_{od} + \lambda_f) / R_c \end{bmatrix} \tag{2.7}$$

where V_d and V_q are the *d*- and *q*-axis terminal voltages, I_d and I_q the *d*- and *q*-axis armature currents, V_{od} and V_{oq} the *d*- and *q*-axis internal voltages, I_{od} and I_{oq} the *d*- and *q*-axis magnetizing currents, I_{cd} and I_{cq} the *d*- and *q*-axis mechanical and core loss currents, and L_d and L_q are the *d*- and *q*-axis inductances, respectively. R_c is the equivalent core loss resistance, R_s the armature winding resistance per phase, λ_f the permanent magnet linkage, ω_e the rotor speed in electrical angular frequency, and p is the differential operator (=*d*/*dt*).

The electromagnetic torque T_{em} and electromagnetic power P_{em} of PMSMs can be determined as

$$T_{em} = \frac{3}{2} P\left(\lambda_f I_{oq} + \left(L_d - L_q \right) I_{od} I_{oq} \right) \tag{2.8}$$

$$P_{em} = T_{em} \omega_m \tag{2.9}$$

where P is the number of pole pairs of the PMSM, and ω_m is the rotor speed in mechanical angular frequency.

The copper loss P_{cu} and the core loss P_c can be estimated as

$$P_{cu} = \frac{3}{2} R_s (I_d^2 + I_q^2) = \frac{3}{2} R_s \left[(I_{od} - \frac{\omega_e L_q I_{oq}}{R_{m\&c}})^2 + (I_{oq} + \frac{\omega_e (L_d I_{od} + \lambda_f)}{R_{m\&c}})^2 \right] \tag{2.10}$$

$$P_c = \frac{3}{2} R_c (I_{cd}^2 + I_{cq}^2) = \frac{3}{2} \left[\frac{\omega_e^2 (L_q I_{oq})^2}{R_c} + \frac{\omega_e^2 (L_d I_{od} + \lambda_f)^2}{R_c} \right] \tag{2.11}$$

Then, the total main loss of the PMSM which consists of the copper loss, core loss and mechanical loss is expressed as

$$P_{loss} = P_{cu} + P_c + P_{mech} \tag{2.12}$$

where P_{mech} is the mechanical loss of the PMSM.

Ignoring the eddy current loss of permanent magnets and other stray losses, the output power, input power, and efficiency of the PMSM are calculated as

$$P_{output} = P_{em} - P_{mech} \tag{2.13}$$

$$P_{input} = P_{em} + P_{cu} + P_c \tag{2.14}$$

$$\eta = \frac{P_{output}}{P_{input}} \times 100\% \tag{2.15}$$

where P_{output} is the output power, P_{in} is the input power, and η is the efficiency of the PMSM.

To apply the ECM in motor characteristic analysis, the parameters including the equivalent core loss resistance should be identified properly. Generally, there are two methods to determine the value of the equivalent core loss resistance, i.e., numerical calculation based on the finite element analysis (FEA) and prototype tests at no-load conditions. In [12], the core loss of the PMSM is calculated based on the FEA, and the harmonic components of the magnetic flux density are concerned, while the core loss at each element is calculated from the summation of the core loss generated from different frequencies of the magnetic flux density. Finally, the total core loss of the PMSM is obtained by the summation of the core loss in all elements. After calculating the total core loss W_c, the equivalent core loss resistance R_c can be determined as

$$R_c = V_{od}^2 / W_c = V_{oq}^2 / W_c \tag{2.16}$$

Fig. 2-10 presented another kind of *d*-and *q*-axis ECM of PMSMs [23, 24]. In this ECM, L_{ls} is the leakage inductance of per phase, and L_{md} and L_{mq} are the *d*-axis and *q*-axis components of the magnetizing inductance, respectively. Fig. 2-10 separated the *d*- and *q*-axis inductances into magnetizing inductances and leakage inductances, and both of them contribute to the core loss.

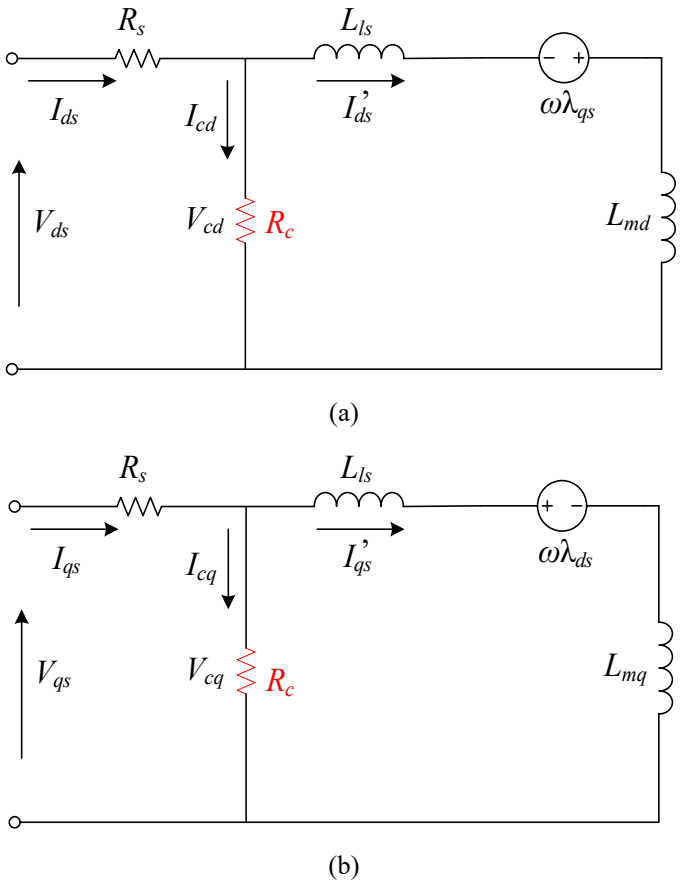

Fig. 2-10 ECM of PMSMs with predictable core loss: (a) *d*-axis; (b) *q*-axis [23].

Nevertheless, in the opinion of the author of this thesis, the ECM of PMSMs considering the leakage inductances under the *d*-and *q*-axis reference frame should be modified as shown in Fig. 2-11, and L_l is the leakage inductance of per phase. The flux linkage generated by phase windings can be expressed in terms of the leakage linkage and the magnetizing linkage. However, the leakage flux only links the stator winding itself and does not contribute much to the core loss of the stator. Therefore, the magnetizing flux

linkages, in which the equivalent core loss resistances are paralleled, should exclude the leakage inductances.

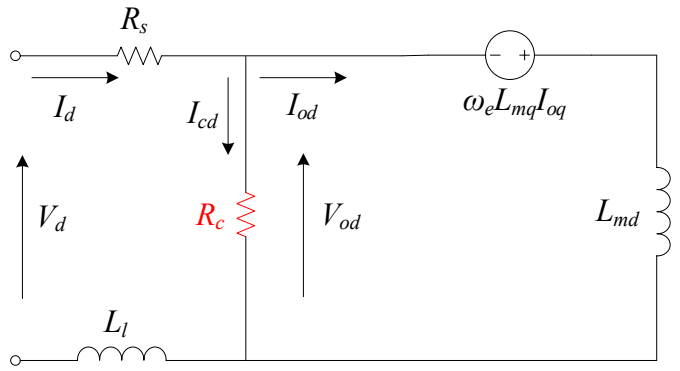

(a)

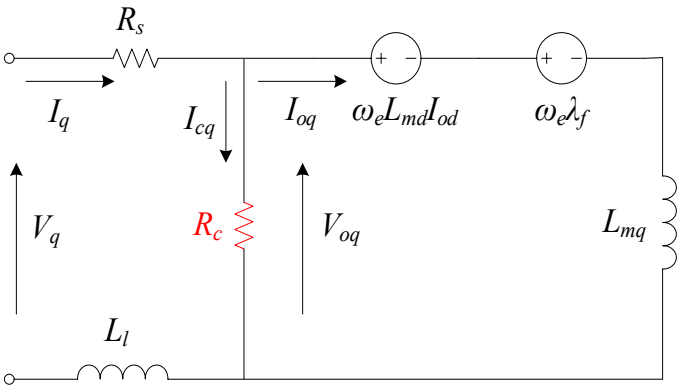

(b)

Fig. 2-11 ECM of PMSMs considering the core loss and leakage inductance: (a) *d*-axis; (b) *q*-axis.

After the reference frame transformation, the three-phase sinusoidal currents under the *abc* reference frame can be recognized as direct currents under the *d*-and *q*-axis reference frame. Therefore, based on the concept of the direct currents, the voltages across the *d*- and *q*-axis inductances would be zero in the steady state, resulting in the elimination of the *d*-and *q*-axis inductances in the equivalent circuit model of PMSMs [36-42], as shown in Fig. 2-12 [40]. For the determination of the equivalent core loss resistance R_c, although the value of R_c changes with the operating conditions, a considerable number of research works calculated it from the results of tests performed at nominal voltage and synchronous speed, i.e., R_c is assumed to be a constant in that condition [37, 40].

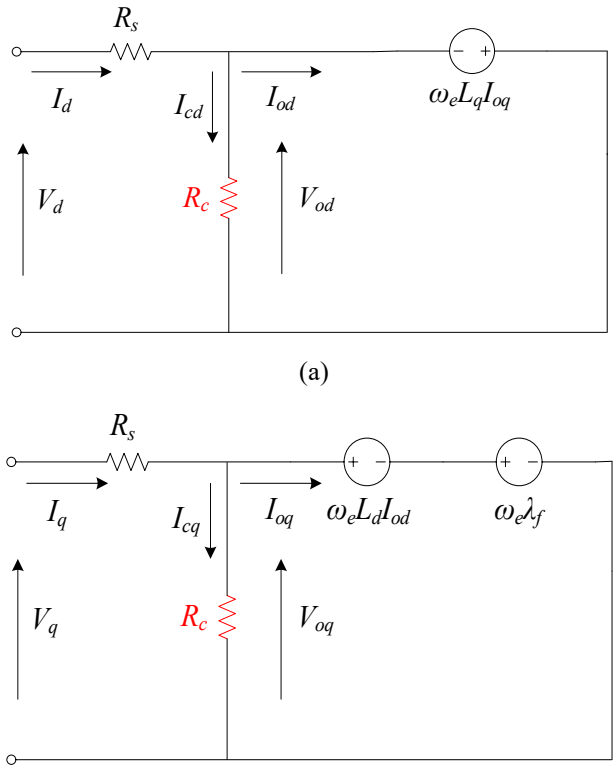

Fig. 2-12 ECM of PMSMs with predictable core loss: (a) *d*-axis; (b) *q*-axis [40].

When the PMSM is operated in the high-speed region, the field weakening control strategy is generally applied. During this condition, the harmonic components of the flux become more significant, especially in load conditions, and this might lead to underestimation of the core loss. Therefore, in [21], the harmonic components are considered by increasing the voltage drop across the equivalent core loss resistance, while the circuit model is illustrated in Fig. 2-13. Since the harmonic inductances L_h are added, the additional voltage drops $\omega_e L_h I_{oq}$ and $\omega_e L_h I_{od}$ would increase the power consumed by the equivalent core loss resistance R_c.

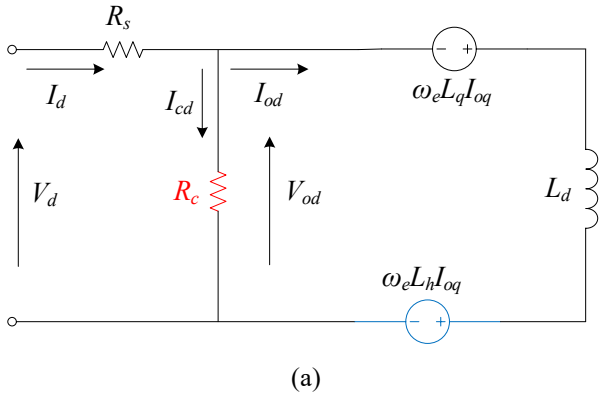

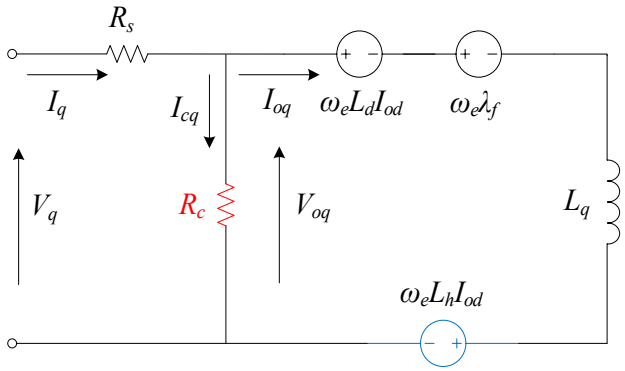

(b)

Fig. 2-13 ECM of PMSMs with predictable core loss: (a) d-axis; (b) q-axis [21].

By using the Fourier analysis, harmonic components of the flux the at load condition can be identified, and then each component is divided by the fundamental component of the current and added together. Thus, the harmonic inductance L_h can be calculated, as shown in (2.17). Besides, the corresponding voltage equations of this ECM are expressed as in (2.18) and (2.19).

$$L_h = \sum_{i=3,5,7\ldots}^{\infty} \frac{\lambda_{oi}}{I_a} \tag{2.17}$$

$$V_{od} = \omega_e L_q I_{oq} + \omega_e L_h I_{oq} \tag{2.18}$$

$$V_{oq} = \omega_e \lambda_f + \omega_e L_d I_{od} \mp \omega_e L_h I_{od} \tag{2.19}$$

where I_a, I_{od}, and I_{oq} are the phase current, d- and q-axis currents, λ_f and λ_{oi} the linkage flux generated by permanent magnets and the i-th harmonic component of the flux linkage, respectively.

Furthermore, the no-load core loss is obtained by using FEA and the corresponding resistance R_{c1} is expressed by a function of speed as

$$R_{c1} = \frac{(\omega_{e1} \times \lambda_{o1})^2}{W_{i1}} \approx a\omega_{e1}^b \tag{2.20}$$

where R_{c1} is the equivalent core loss resistance calculated at the no-load condition, W_{i1} the no-load core loss, λ_{o1} the no-load flux linkage, ω_{e1} the reference angular speed, and a and b are coefficients.

The core loss resistance corresponding to the load condition R_{c2} can be expressed as

$$R_{c2} = R_{c1} \times \frac{\lambda_{o2}^2}{(\frac{\lambda_{o2}}{\lambda_{o1}})^{1.4} \cdot \lambda_{o1}^2} \tag{2.21}$$

where R_{c2} is the equivalent core loss resistance calculated at the load condition, and λ_{o2} is the load flux linkage.

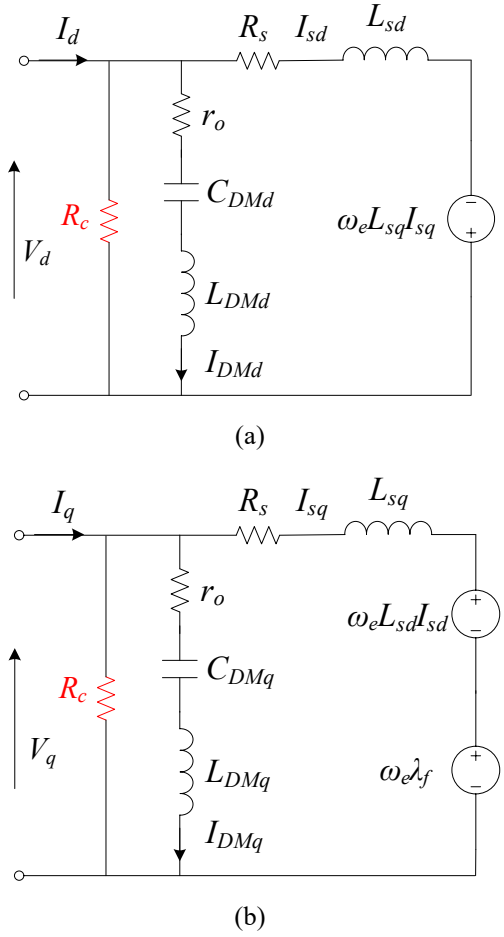

Fig. 2-14 Differential mode ECM of PMSMs with predictable core loss: (a) *d*-axis; (b) *q*-axis [43].

As shown in Fig. 2-14, an ECM of the PMSM which is suitable for high-frequency differential mode calculation was proposed in [43]. The differential mode branch contains series $r_0 L_{DMd} C_{DMd}$ ($r_0 L_{DMq} C_{DMq}$) combination to stand for the second resonance, while the differential mode capacitance C_{DM} together with the motor inductance L_s almost determines the value of the first resonance. Moreover, L_{DMd} and L_{DMq} are the *d*- and *q*-axis differential mode leakage inductances. The equivalent core loss resistance R_c is

normally of high values, and determined from the maximum value of the measured input impedance at the resonance frequency.

Taking into account not only the copper loss and core loss but also the PM loss, an ECM with a series-parallel structure was introduced [22], as shown in Fig. 2-15. R_{Fe} and R_{PM} are the equivalent core loss and PM loss resistances, respectively, and they are indirectly achieved based on finite element method (FEM) results.

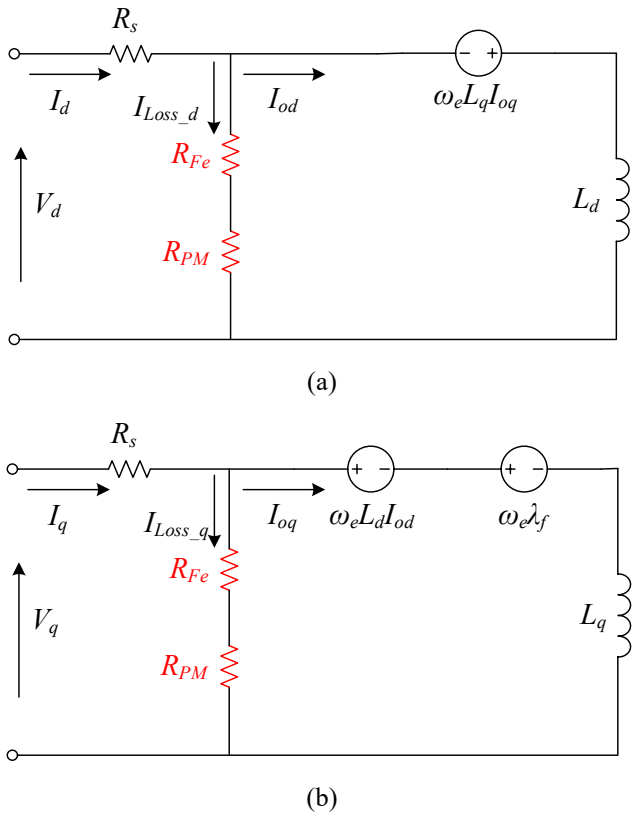

Fig. 2-15 ECM of PMSMs with predictable core loss: (a) d-axis; (b) q-axis [22].

Based on the ECM of Fig. 2-15, the copper loss as well the summation of the core loss and PM loss can be described as [22]

$$P_{cu} = \frac{3}{2} R_s \left[\left(\frac{\lambda_d - \lambda_f}{L_d} \right)^2 + \left(\frac{T_e}{1.5P \left[\frac{\lambda_f}{L_q} + (L_d - L_q) \frac{\lambda_d - \lambda_f}{L_d L_q} \right]} \right)^2 \right] \tag{2.22}$$

$$P_{Fe} + P_{PM} = \frac{3}{2} \frac{\omega_e^2}{R_{Fe} + R_{PM}} (\lambda_q^2 + \lambda_d^2) \tag{2.23}$$

To have an overview of all the ECMs with predictable core loss mentioned above, a comparison is made with five indicators, as shown in Table 2-1.

Table 2-1. Comparison of the ECMs

ECM	**Value of equivalent core loss resistance**	**Equivalent core loss resistance identification**	**Difficulty of application**	**Accuracy**	**Additional items**
Fig. 2-4	A single-valued resistance	Not mentioned	Easy	Low	None
Fig. 2-5	A single-valued resistance	Experimental test	Easy	Low	None
Fig. 2-6	A variable resistance (function of motor speed)	FEM	Medium	Relatively high	Incorporating the rotating core loss
Fig. 2-7	Two single-valued resistances	Experimental test	Most difficult due to the coupling structure and complex experimental conditions	Medium	Incorporating the saliency of the motor
Fig. 2-8	Two single-valued resistances	Experimental test	Medium	Medium	Incorporating the saliency of the motor
Fig. 2-9	A single-valued resistance for *d*- and *q*-axis respectively	Experimental test/FEM	Easy	Low	None
Fig. 2-10	A single-valued resistance for *d*- and *q*-axis respectively	Experimental test	Relatively difficult due to the separation	Low	Leakage inductances

			of the leakage inductance		
Fig. 2-11	Flexible	Flexible	Relatively difficult due to the separation of the leakage inductance	Medium	Leakage inductances
Fig. 2-12	A single-valued resistance for *d*- and *q*-axis respectively	Experimental test	Easy	Lowest due to eliminating of inductance	None
Fig. 2-13	A variable resistance (function of motor speed) for *d*- and *q*-axis respectively	FEM	Relatively difficult due to the identification of the harmonic inductance	Relatively high	Harmonic inductance
Fig. 2-14	A single-valued resistance for *d*- and *q*-axis respectively	Experimental test	Difficult and suitable for high-frequency differential mode	Relatively high	Differential mode capacitance and leakage inductance
Fig. 2-15	A single-valued resistance for *d*- and *q*-axis respectively	FEM	Easy	Medium	PM loss

2.5 Core Loss Measurement

The core loss measurement methods can be roughly divided into two categories. The first category reviewed in this section is the core loss separation methods based on the no-load and load tests. Then, the core loss direct measurement methods are presented based on the stator core test apparatus.

2.5.1 Core Loss Separation Method

1) Based on the No-load Tests (Open-circuit Tests)

When the PMSM operates as a generator, no-load tests, also called open-circuit tests, are conducted with the machine armature terminals open-circuited and hence no current flows in the armature windings, i.e., no copper loss. Therefore, the schematic view of the no-load (open-circuit) test and the power flow of the electrical machine are shown in Figs. 2-16 and 2-17, respectively. In Fig. 2-16, the target PMSM is driven by a DC motor or AC motor with variable speed drive system, and they are connected via a torque transducer or a mechanical coupling. From Fig. 2-17, it is noted that the power input the PMSM would be the summation of the core loss and the mechanical loss (friction and windage loss). The equation of power flow can be represented as

$$P_{\text{input}} = P_{\text{mech.loss}} + P_{\text{core loss}} \tag{2.24}$$

Then, the core loss of the PM machine would be the total input loss minus the mechanical loss under the no-load condition.

$$P_{\text{core loss}} = P_{\text{input}} - P_{\text{mech.loss}} \tag{2.25}$$

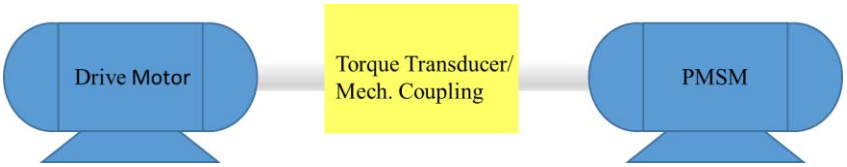

Fig. 2-16 Schematic view of the no-load test.

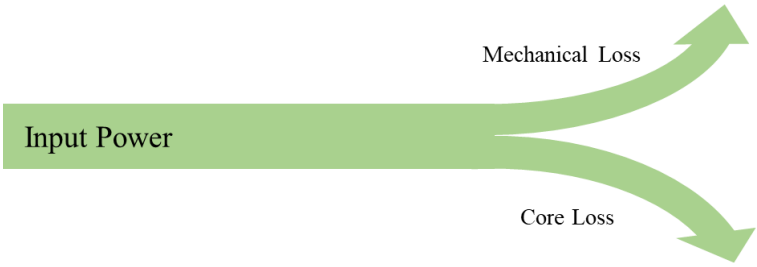

Fig. 2-17 Power flow of electrical machines under no-load condition.

However, it is unpractical to define tests for PMSMs which can provide a direct measurement of the core loss independent of the rotational friction and windage loss under no-load (open-circuit) conditions. Unlike wound-field machines in which the magnetic flux in the machine is controlled by the field current and can be varied from zero to the rated operation flux level or even higher, the flux excitation of permanent

magnet machines is fixed at a level determined by the PMs. It is not possible to “turn off” the magnetic flux of PMs to provide a direct measurement of the friction and windage loss under no-load (open-circuit) conditions. Thus, the key issue of the core loss measurement of PM machines is how to separate the core loss and the friction and windage loss. In order to measure the friction and windage loss, two alternative test methods can be implemented, i.e., using a dummy rotor or using a dummy stator.

According to the IEEE standards, replacing the PM rotor with a non-magnetized equivalent rotor can measure the friction and windage loss, and the equivalent rotor should be one of the following:

a) An identical rotor, including magnets, in which the magnets have not be magnetized yet.

b) An identical rotor in which the magnets have not be inserted yet and the magnet space is filled with a non-magnetized material.

c) A rotor which is physically similar to the PM rotor in all aspects which affect friction and windage loss.

With the equivalent rotor installed in the PMSM, the drive motor is then used to acquire the speed of interest. In this situation, the power input the PMSM equals the friction and windage loss, and it can be measured directly or indirectly. In [44-60], the measurements of the friction and windage loss are conducted by using the dummy rotor method. To be more specific, in [45, 47-51, 54, 55, 58], the rotor with magnets was replaced by a rotor without magnets but with the same bearings and identical shape, while in [46, 52, 53, 57], a rotor having non-magnetized permanent magnets was adopted. Besides, in [44] a plastic rotor and in [56] an induction motor rotor was substituted to remove the core loss component and to ensure that the friction and windage loss is not altered. Repeating the no-load test procedure, the relationship between the rotation speeds and the mechanical loss can be drawn.

For the dummy stator method, in [31, 61, 62] the stator was eliminated from the motor, while the rotor and bearings of the test motor were installed in the experiment set to measure only the mechanical loss. In [63, 64] the PM machine stator was replaced by a

non-magnetic replica made of hard plastic with exactly the same geometrical dimensions as the original stator. Then, the dummy stator was assembled with the original rotor, bearings and couplings to ensure that the friction and windage loss is not altered. Particularly, for the core loss measurement in [64], not only the plastic tube is utilized to imitate the mechanical loss but also the motor end effects are removed by using two motors with active lengths of 38 mm and 76 mm, respectively. Assume two motors of different active lengths have the same end effects because of the same end structures. The net core loss after the removal of the end effects in the 76 mm motor should be twice as much as that in the 38 mm one. Thus, the core loss due to the end effects can be deduced by [64]:

$$P_{end} = 2P_{38} - P_{76} \tag{2.26}$$

where P_{38} and P_{76} are the core loss in the 38 mm and 76 mm motors, respectively, before the removal of the end effects.

As mentioned above, the power input of the PMSM can be measured directly and indirectly. When the drive motor and the PMSM are connected via a torque transducer and the dummy stator or dummy rotor method is employed, the mechanical loss torque T_{mech} can be measured directly and the corresponding power loss $P_{\text{mech.loss}}$ can be obtained by multiplying this torque and test speed ω_m

$$P_{mech.loss} = \omega_m T_{mech} \tag{2.27}$$

If T_{mech} is expressed in Nm and ω_m in rad/sec, $P_{\text{mech.loss}}$ will be in Watts. Using a torque transducer to collect the torque data is the most common method when conducting the no-load tests and the mechanical loss tests, since it can provide accurate and convenient results efficiently.

On the other hand, when the torque transducer is absent and the test system includes a mechanical coupling between the drive motor and the PM machine, the mechanical loss torque also can be measured indirectly, and this kind of test method is also called the retardation test. In this method, the drive motor is used to bring the motor to a desired initial test speed. If the power to the drive is then disconnected, the subsequent decay in machine speed will be determined by the combined inertia and the friction and windage

loss torque of the machine under test and the drive motor. The rotational speed is recorded as the system decelerates, while the total decelerating torque of the test machine and the drive motor $T_{dec}(\omega_m)$ is calculated as

$$T_{dec}(\omega_m) = J_c \frac{d\omega_m}{dt} \tag{2.28}$$

where ω_m is the machine speed, J_c the total moment of inertia of the test machine and drive motor, and T_{dec} (ω_m) the total decelerating torque of the test machine and the drive motor. Note that this torque is a function of the machine speed.

Then, the machine loss for both test PM machine and the drive motor as a function of speed can be obtained as

$$P_{loss}(\omega_m) = \omega_m T_{dec}(\omega_m) \tag{2.29}$$

The loss of the drive motor should be well-defined so that the loss of the test PM motor can readily be obtained by subtracting of the drive motor loss from the total loss. In [26, 65], this kind of retardation test method was presented to measure the mechanical loss.

2) Based on the Load Tests

PM machines can be operated as both motors and generators, and a typical core loss test set-up under the load conditions can be illustrated in Figs. 2-18 and 2-19, respectively. In Fig. 2-18, the testing PM machine works as a generator, and it is driven by a rotating machine capable of bringing the generator to the desired test speeds and supplying the required test power. The generator load may be a variable-impedance load such as a resistor bank. In Fig. 2-19, the testing PMSM works as a motor and a mechanical load is used. Additionally, the power flow of the PM machine under a load condition is shown in Fig. 2-20, while the input power of the PMSM equals the summation of the output power, mechanical loss, copper loss, and core loss. The equation of the power flow can be represented as

$$P_{\text{input}} = P_{\text{output}} + P_{\text{mech.loss}} + P_{\text{core loss}} + P_{\text{copp.loss}} \tag{2.30}$$

Therefore, the absence or presence of the copper loss, output power and core loss due to the stator armature reaction are the main differences between the no-load core loss and the load core loss tests. The total loss can be obtained from the difference between the input power and output power. The core loss can then be obtained by subtracting the copper loss and mechanical loss from the total loss

$$P_{\text{core loss}} = P_{\text{input}} - P_{\text{output}} - P_{\text{mech.loss}} - P_{\text{copp.loss}} \tag{2.31}$$

The mechanical loss can be measured by the same methods reported in the last section. In [50, 53, 66], the load core loss is reported.

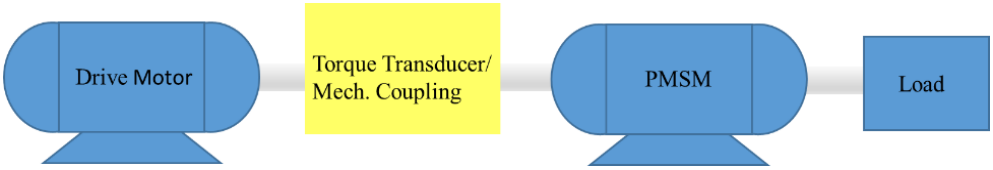

Fig. 2-18 Schematic view of the load test with the testing PMSM working as a generator.

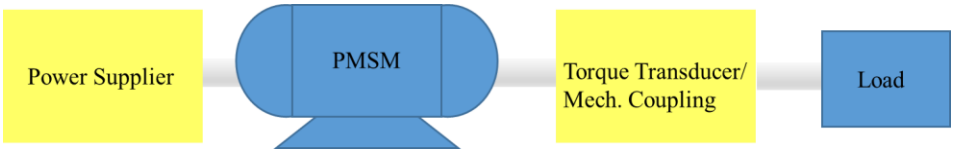

Fig. 2-19 Schematic view of the load test with the testing PMSM working as a motor.

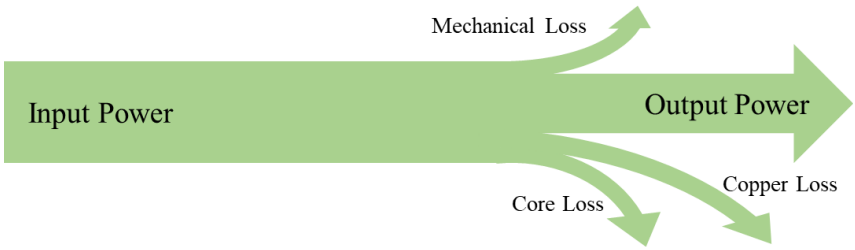

Fig. 2-20 Power flow of electrical machines under load condition.

In order to remove the mechanical loss, Xue *et al*. presented a core loss measurement method based on the locked rotor test when the PMSM is powered by a pulse width modulation (PWM) inverter and by a sinusoidal current supplier, respectively, as shown in Fig. 2-21 [67]. In this locked rotor test, the permanent magnets are removed from the rotor to eliminate the influence of the permanent magnet eddy current loss. Then the measured core loss can be calculated by subtracting the copper loss from the total input

power. The locked rotor test is also reported in [68-70] to remove the uncertainty associated with the mechanical loss. Since the loss in the locked rotor test is usually different from those under normal rotating operation, the aim of the locked rotor test is more to validate the core loss models.

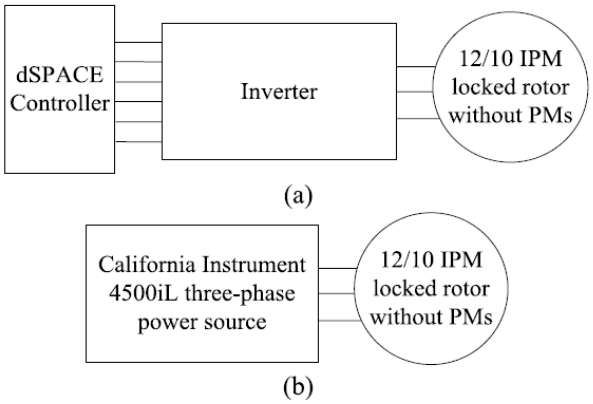

Fig. 2-21 Diagrams and photos of core loss test rig. (a) When powered by PWM inverter; (b) When powered by sinusoidal current supplier [67].

2.5.2 Core Loss Direct Measurement Methods

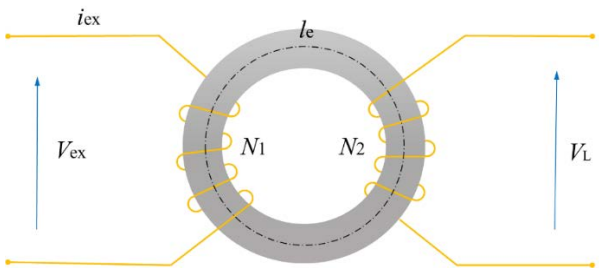

Fig. 2-22 A stator core in the measurement system.

Fig. 2-22 illustrates the basic principle of the core loss measurement of a stator core, in which V_{ex} is the excitation voltage, and i_{ex} the excitation current. Since the coils are uniformly wound around the ring core, the magnetic field intensity H and magnetic flux density B within the core can be assumed uniform. According to Ampere's law, one can obtain

$$Hl_e = N_1 i_{ex} \tag{2.32}$$

where l_e is the mean length of the stator core.

Thus, the magnetic field intensity H can be calculated by

$$H = N_1 i_{ex} / l_e \tag{2.33}$$

By the Faraday's law, the *emf* induced in the pick-up coil N_2 can be expressed as

$$V_L = N_2 A_e \frac{dB}{dt} \tag{2.34}$$

where A_e is the cross sectional area of the stator core, N_1 the number of turns of the exciting winding, and N_2 the number of turns of secondary winding. Therefore, the magnetic flux density in the stator core can be captured by the *emf* signal V_L and calculated as

$$B = \frac{1}{N_2 A_e} \int V_L dt \tag{2.35}$$

Finally, the core loss in the stator core is directly calculated according to the equation below and then divided by the stator yoke weight.

$$P(t) = \frac{N_1}{N_2} \frac{1}{T} \int_0^T i_{ex}(t) \cdot V_L(t) dt \tag{2.36}$$

where T is the waveform period.

This method of the stator core loss measurement described above is widely employed [30, 71-75]. For example, in [30, 71] the layout of the measurement setup (a) and the used instruments and one of the core sample (b) are shown in Fig. 2-23.

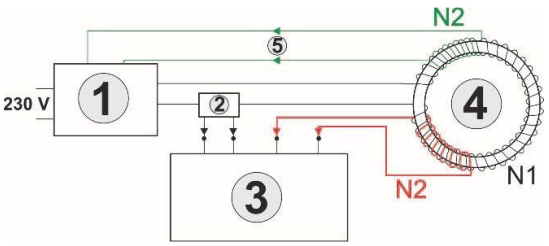

(a)

(b)

Fig. 2-23 (a) Layout of the measurement setup, (b) The used instruments and one of the core sample [30, 71].

In Fig. 2-23, *1* is the programmable power source which can operate with a signal derived from the feedback signal of the system, thereby providing a sinusoidal voltage induced in the secondary winding of the test core. *2* is the measuring transducer, *3* the digital oscilloscope, *4* the tested stator core, *5* the feedback, and *6* the analogue control meter.

Tekgun *et al*. developed a stator core loss measurement technique including the finite element analysis (FEA), which can be considered as a further step of the method described above [76]. First, flux density waveforms in various parts, where the core loss is approximately uniform, of the electric machine are determined using FEA. Second, the same waveforms are generated in a wound toroidal core made of the same material as used in the machine, with a novel flux-controlled core loss tester unit as shown in Fig. 2-24, and this apparatus is capable of controlling both dc and ac flux densities. This tester allows that the actual core loss is measured per unit mass under known and controllable flux density waveforms, and then the total motor core loss is calculated by integrating the measured W/kg loss values for predefined sections of the motor. However, only unidirectional flux densities are considered, i.e., the rotating flux densities and the rotating core loss are excluded in this research.

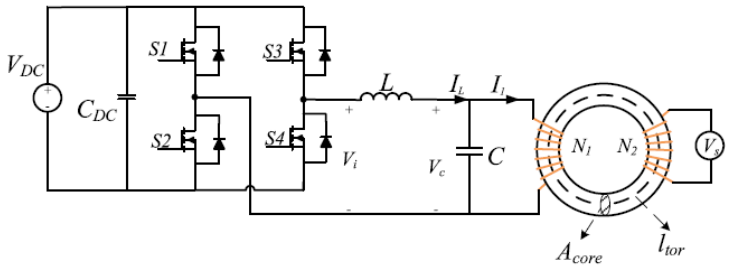

Fig. 2-24 Flux-controlled core loss tester [76].

A core loss test that nearly duplicates the magnetic field conditions in a spindle motor was designed and shown in Fig. 2-25 [77]. A base plate supports this experimental apparatus, and the sample core is mounted on a mandrel and connected to a variable speed motor whose speed is checked with a strobe lamp. The sampled core is axially centered and spun concentrically within a 12-pole electromagnet that is connected to a fixed shaft optical torque gauge. The electromagnet poles are alternately polarized to simulate the alternating permanent magnet poles of a motor, and the number of poles can be adjusted. When the sample core is spun, the drag torque of the electromagnet due to friction and windage alone is measured by the torque gauge. After that, the electromagnet is energized, and the total reaction torque is recorded. The core loss is recorded as the product of the angular velocity of the core and the total reaction minus the friction and windage torque, as shown in the equation below

$$P_{\text{core loss}} = \left(T_{\text{total}} - T_{\text{wind}}\right) \times 2\pi \times \frac{rpm}{60} \tag{2.37}$$

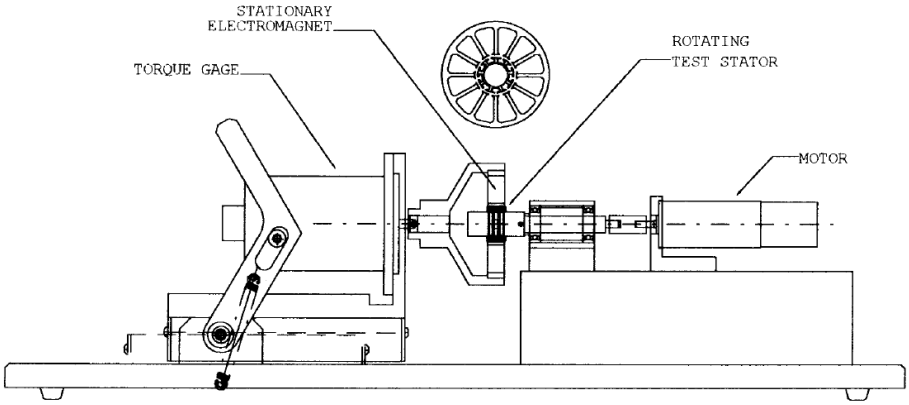

Fig. 2-25 Core loss test apparatus [77].

A core loss measurement system for semi-processed geometries like single tooth was presented by Veigel *et al.*, which consists of a digital controller, a power amplifier, a measurement adapter for individual test specimen and a power measurement system [78]. The magnetic circuit of this single tooth tester is shown in Fig. 2-26.

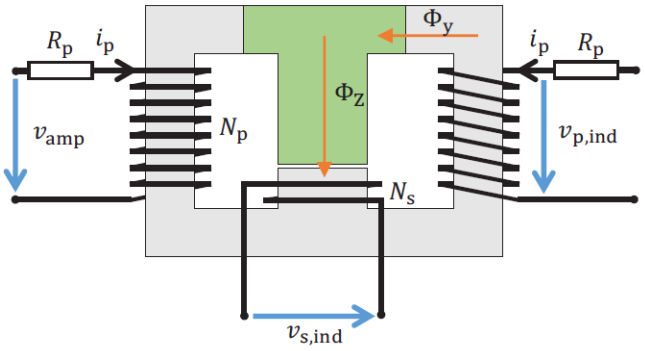

Fig. 2-26 Magnetic circuit of the single tooth tester and declaration of tooth flux Φz and yoke flux Φy [78].

The voltage equation of this system is shown below:

$$v_{\text{amp}}(t) = R_p i_p(t) + v_{\text{p,ind}}(t) \tag{2.38}$$

where v_{amp} (t) is the amplifier voltage, R_p the winding resistance, i_p (t) the winding current, and $v_{p,ind}$ (t) the primary induced voltage.

The induced voltage $v_{p,ind}$ (t) is caused by the alteration of the magnetic flux of the winding

$$v_{\text{p,ind}}(t) = N_p \frac{d\phi_y(t)}{dt} \tag{2.39}$$

where N_p is the number of turns of the primary winding, and Φ_y (t) the magnetic flux in the corresponding part of the yoke.

Therefore, a relationship between primary and secondary induced voltages can be established as

$$v_{\text{s,ind}}(t) = N_s \frac{d\phi_z(t)}{dt} = N_s \frac{2 \times d\phi_y(t)}{dt} \tag{2.40}$$

$$v_{\text{s,ind}}(t) = 2\frac{N_s}{N_p} v_{\text{p,ind}}(t) \tag{2.41}$$

where N_s is the number of turns of the secondary winding, and Φ_z (t) the magnetic flux in the tooth.

The power that is absorbed by this electromagnetic system is a composition of the ohmic loss in the primary windings, the core loss in the yoke and the core loss in the test specimen which is to be determined. The system power equation can be written as

$$v_{\text{amp}}(t) i_p(t) = R_p i_p^2(t) + \frac{N_s}{2N_p} v_{\text{s,ind}}(t) i_p(t) \tag{2.42}$$

The left side of the above equation is the system power, and the first term of the right side of the equation is the ohmic loss in the winding, while the last term is the core loss. This relationship shows the possibility to determine the system's core magnetization and loss by observing the secondary voltage and the primary current over time. This oscillating waveform can be split up into a part of reactive power and a part of active power. The part of reactive power is equal to the magnetization of the core, and the part of active power is equal to the core loss that has to be determined. However, the magnetizing conditions inside the yoke's arrangement are not changed in another tooth specimen, and the core loss of the yoke only depends on the flux waveform Φ_y (t). Thus, the yoke's flux and core loss are clearly defined by the operation point, and the core loss of the test specimen can be separated. Moreover, Veigel *et al*. employed this single tooth tester to determine the core loss of motor stator [79].

2.6 Conclusion

This chapter aims to present an extensive review on the ECMs considering the core loss and core loss measurement methods of PMSMs. ECMs for both per-phase and *d*-and *q*-axis are analyzed, and the equivalent core loss resistance is connected in parallel with the magnetizing branch, generally. Although various ECMs of PMSMs under *d*- and *q*-axis reference frame were developed in previous studies, there are some mismatches between the ECM and voltage equations in some papers. Therefore, corresponding modifications are reported in this paper.

For core loss measurement of PMSMs, the most common method is to separate it and the mechanical loss from no-load tests, or separate it and the mechanical loss as well as the

copper loss from loading tests. A dummy rotor or a dummy stator is employed to imitate the mechanical loss and exclude the core loss generated by permanent magnets. Moreover, this chapter also surveys other measurement techniques based on the testing apparatus to measure the stator core loss of electrical machines.

CHAPTER 3. CORE LOSS WITH ROTATING MAGNETIC FIELDS AND EQUIVALENT RESISTANCES IN CIRCUIT MODELS

3.1 Introduction

Recently, as more and more PMSMs are operating in the high speed (frequency) range, the core loss has increasing significant influences on the efficiency, temperature rise, and volume/weight of motors. For a PMSM with a specified capacity, compared with the traditional ignoring or roughly estimating the core loss in the motor design and control, a lighter cooling design is required if the core loss can be precisely predicted, and higher efficiency is obtained if the motor control strategy appropriately manages the core loss. Thus, the torque/power density of the PMSM can be effectively increased. Therefore, high-precision core loss calculation models and effective ways to model the core loss into the ECM are required urgently.

According to Bertotti's core loss separation model, the core loss can be divided into three parts: hysteresis loss, (classical) eddy loss, and anomalous loss or excess loss. The hysteresis loss is caused by Barkhausen jumps and irreversible rotation processes in the magnetic material of electrical machines. The induced voltage by the alternating magnetic field causes circular currents in the iron sheets that cause the classical eddy current loss. The anomalous loss originates from the microscopic eddy current produced by the displacement of the Bloch walls. Material characteristics, excitation frequencies and the magnetic flux density in electrical devices are the main factors affecting the values of the core loss. Therefore, in this chapter, the core loss of the PMSM with 3-D rotating magnetic field will be introduced first. Then, how to model the core loss into the ECM is established systematically.

Soft magnetic composite (SMC) material is formed by surface-insulated iron powder particles, and possesses a number of advantages, including isotropic magnetic and thermal properties, low eddy current loss and relatively low total core loss at medium and higher frequencies, net-shape fabrication process with smooth surface and good finish, and prospect of very low-cost mass production [80]. Due to its powder nature and

isotropic magnetic property, SMC material is suitable for construction of electrical machines of three-dimensional (3D) magnetic fluxes and complex structures, for which it is almost impossible or very difficult to use laminated steels. In the past decades, many investigations have been made to explore SMC material in different types of motor, such as claw pole motor [80, 81], transverse motor [60, 82], axial flux motor [83, 84], universal motor [85, 86] and so on. Therefore, this chapter takes a claw pole permanent magnet motor prototype with SMC core as the example to establish the ECM with the predictable core loss, and experimental verifications of this prototype are set up in both no-load and load conditions.

In the last section of this chapter, an improved deadbeat predictive current control (DPCC) with novel current predictive model of PMSMs is proposed. First, the new predictive model is built, which takes the motor core loss into account and can effectively reduce the errors between the predictive and the actual values of the control variables. Therefore, an improved DPCC containing a higher-precision predictive model is developed. Finally, in order to validate the superior control performance and disturbance robustness of the improved DPCC, comparisons have been made between the traditional and improved approaches.

3.2 3-D Rotating Magnetic Fields of a Claw Pole PMSM

This section will explore the performance of the claw-pole PMSM with SMC core.

Table 3-1 lists the dimensions and major parameters of the claw pole PMSM.

Table 3-1. Dimensions and major parameters of the claw pole PMSM.

Dimensions and parameters	Values	Dimensions and parameters	Values
Rated frequency	300 Hz	Rotor inner radius	41 mm
Number of phases	3	Stator outer radius	40 mm
Rated phase voltage	64 V	Effective stator axial length	93 mm
Rated power	500 W	Shaft outer radius	9 mm

Rated phase current	4.1 A	Airgap	1 mm
Rated speed	1800 r/min	Number of turns	75
Rated torque	2.65 Nm	Number of coils	3
Rated efficiency	81%	Number of strands	2
Number of poles	20	Coil window dimension	17×11 mm^2
Permanent magnets	NdFeB	Diameter of copper wire	0.71
Number of magnets	60	Phase resistance	0.302 Ω
Stator core material	Somaloy^{TM} 500	Rotor outer radius	47 mm

This claw pole PMSM is of the outer rotor structure, and the stator and rotor of the prototype are illustrated in Fig. 3-1. The outer rotor consists of a mild steel case, three arrays of NdFeB magnets for three phases, and two aluminum end plates. Since the flux density in the yoke is almost constant, mild steel is used for the construction of the rotor. The stator has three stacks with an angular shift of 120 electrical degrees from each other. Each stator phase has two pieces of SMC claw pole discs and a single concentrated coil, which is housed between two claw pole discs.

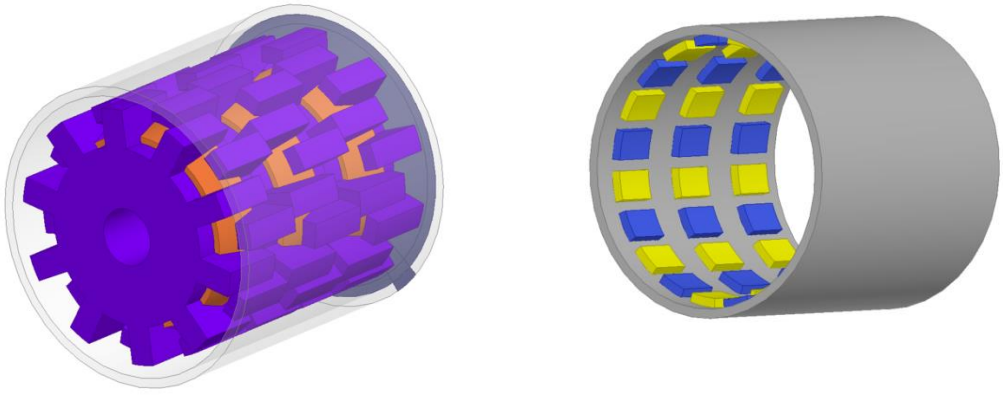

(a) (b)

Fig. 3-1 The structure of the claw pole SMC motor: (a) stator; (b) rotor.

Fig. 3-2 shows the ANSYS simulation model of one pole of the claw pole PMSM, and five points are selected in it, of which point 1 is in the yoke of the stator, points 2 and 3 are in the middle of the stator, and points 4 and 5 are at the top of the stator claw pole.

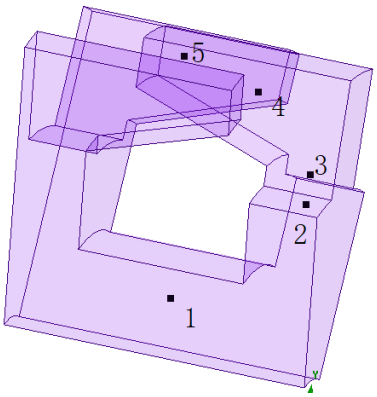

Fig. 3-2 ANSYS simulation model of one pole of the claw pole PMSM.

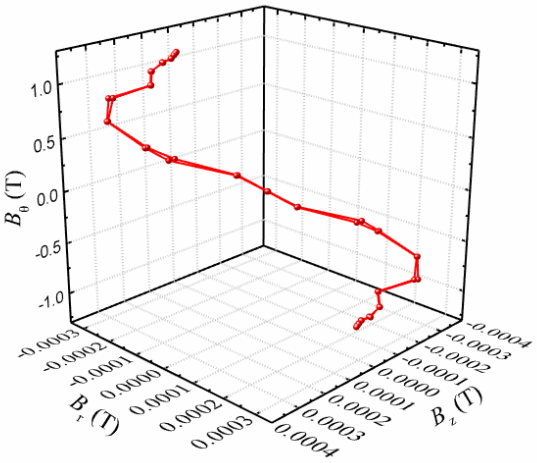

(a) 3-D trajectory of the flux density vector.

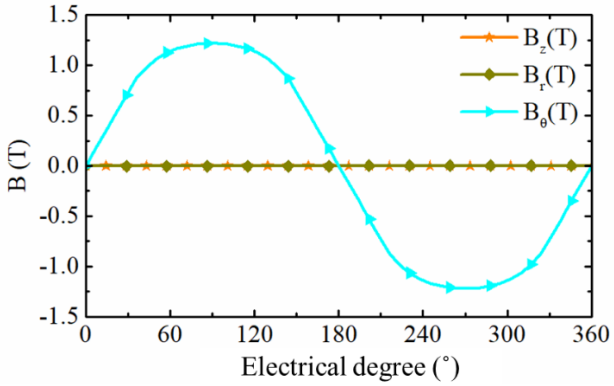

(b) The magnitudes of the axial, radial, circumferential components of the flux density vector.

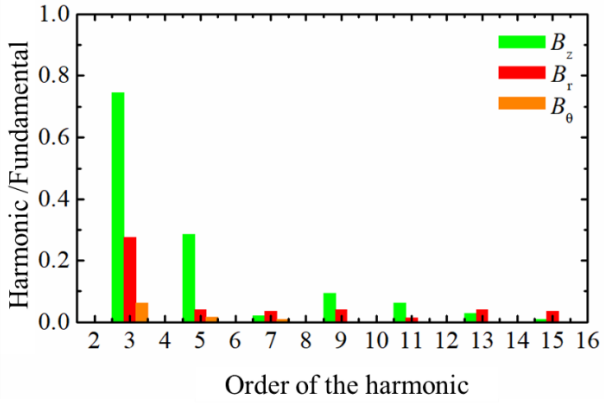

(c) Amplitude relationships between harmonics and fundamentals.

Fig. 3-3 Magnetic flux density characteristics at point 1.

At point 1, the magnetic flux density characteristics at no-load condition are analysed, as shown in Fig. 3-3. Fig. 3-3 (a) depicts the 3-D magnetic flux density trajectory in an electrical cycle, and Fig. 3-3 (b) represents the magnitudes of the axial magnetic flux density B_z, radial magnetic flux density B_r and circumferential magnetic flux density B_θ at different rotor positions, while the amplitude relationships between harmonics and fundamentals of these three components are shown in Fig. 3-3 (c). It can be seen that the most notable vibration of the 3-D magnetic flux density trajectory occurs in the circumferential direction of the motor, and the amplitude of it is about 1.2 T, while the changes of the radial and axial magnetic flux density components are small and fluctuate around zero, respectively. In addition, each magnetic flux density component contains a large number of odd-order harmonics, and the amplitude of the third harmonic of the axial magnetic flux density component B_z even reaches 75% of the fundamental, and the harmonic amplitude decreases as the harmonic order increases.

The magnetic flux density characteristics at the no-load condition of point 2 are analysed in Fig. 3-4, and Fig. 3-4 (a) depicts the 3-D magnetic flux density trajectory in an electrical cycle, Fig. 3-4 (b) the magnitudes of the axial magnetic flux density B_z, radial magnetic flux density B_r and circumferential magnetic flux density B_θ at different rotor positions, and Fig. 3-4 (c) shows the amplitude relationships between harmonics and fundamentals of these three components. The major change of the 3-D magnetic flux density trajectory occurs in the radial direction of the motor with the amplitude of 1.5 T. The amplitudes of

the third harmonic of B_z, B_r, and B_θ account for 48%, 9%, and 29% of the fundamental, respectively.

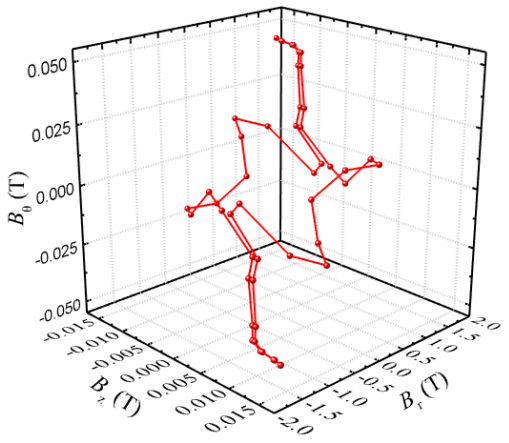

(a) 3-D trajectory of the flux density vector.

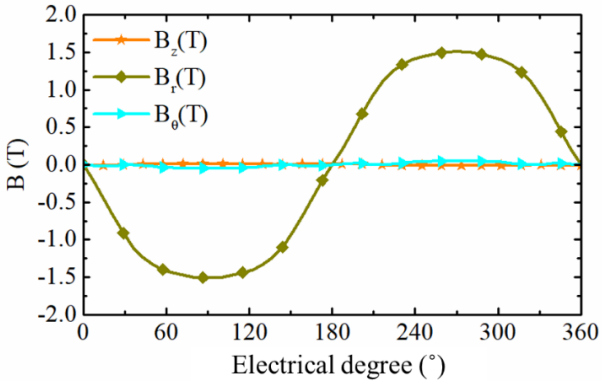

(b) The magnitudes of the axial, radial, circumferential components of the flux density vector.

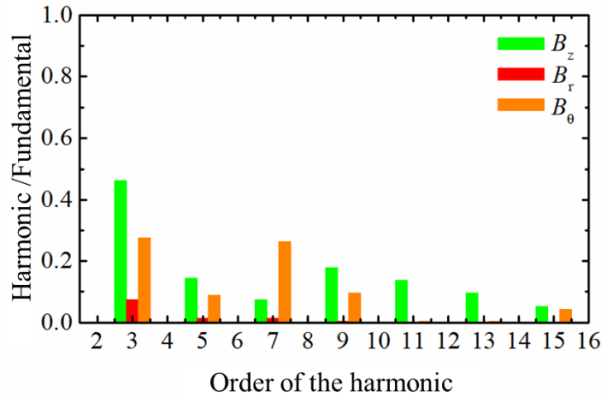

(c) Amplitude relationships between harmonics and fundamentals.

Fig. 3-4 Magnetic flux density characteristics at point 2.

The magnetic flux density characteristics of point 3 are illustrated in Fig. 3-5. Fig. 3-5 (a) is the 3-D magnetic flux density trajectory in an electrical cycle, the shape of which is an approximately irregular quadrilateral. The magnitudes of the axial magnetic flux density B_z, radial magnetic flux density B_r and circumferential magnetic flux density B_θ at different rotor positions are described in Fig. 3-5 (b), which is similar to that of point 2 and the amplitude of the radial magnetic flux density component is about 1.9 T. The amplitudes of the third harmonic of B_z, B_r, and B_θ respectively account for 52%, 5%, and 44% of the fundamental, as shown in Fig. 3-5 (c).

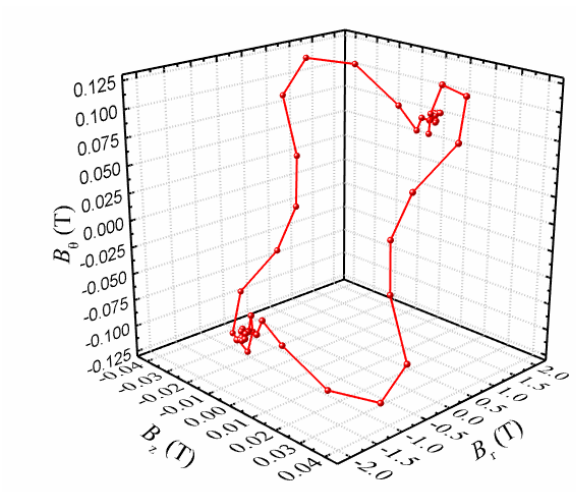

(a) 3-D trajectory of the flux density vector.

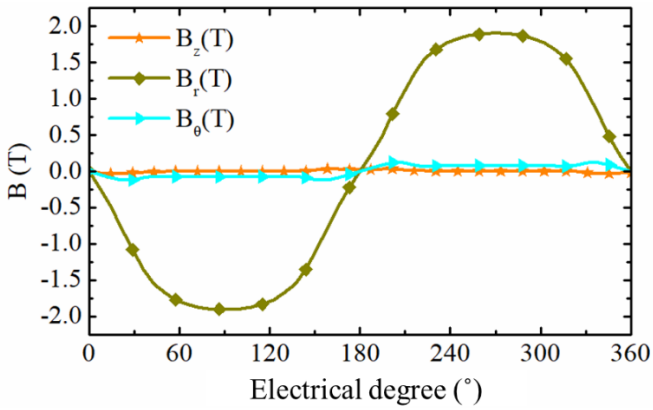

(b) The magnitudes of the axial, radial, circumferential components of the flux density vector.

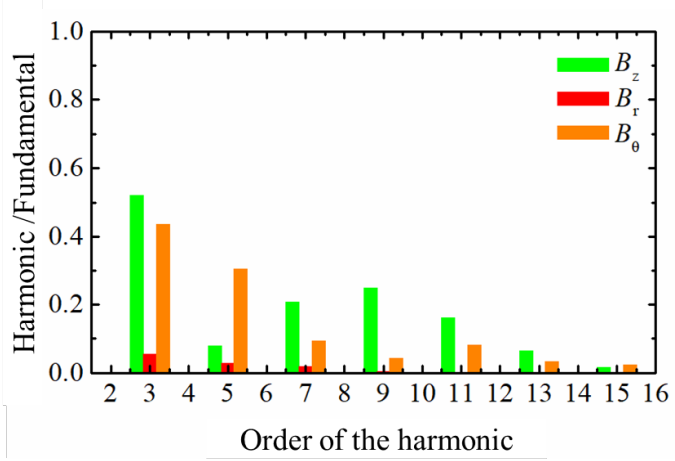

(c) Amplitude relationships between harmonics and fundamentals.

Fig. 3-5 Magnetic flux density characteristics at point 3.

Fig. 3-6 shows the magnetic flux density characteristics at the no-load condition of point 4, and Fig. 3-6 (a) illustrates the approximately elliptical 3-D magnetic flux density trajectory in an electrical cycle, while the axial magnetic flux density B_z, radial magnetic flux density B_r and circumferential magnetic flux density B_θ change according to an approximate sinusoidal law, and the magnitude of them are respectively 0.34 T, 0.68 T, and 1.03 T, as shown in Fig. 3-6 (b). At point 4 of the stator claw pole, the high-order harmonics of each magnetic flux density component are comparatively small, and their 3rd harmonics account for 2.4%, 7.5%, and 6.5% of the fundamental, as analysed in Fig. 3-6 (c).

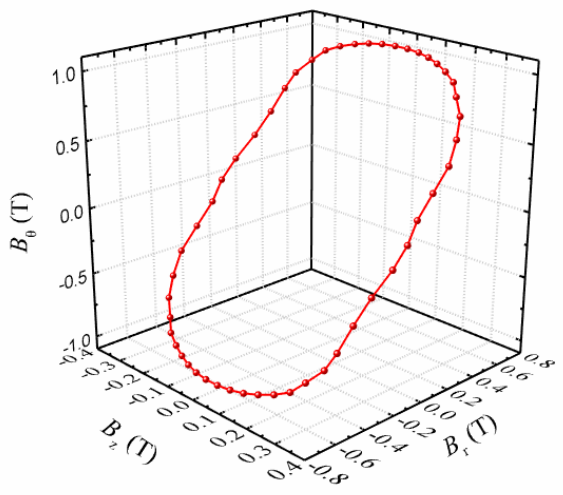

(a) 3-D trajectory of the flux density vector.

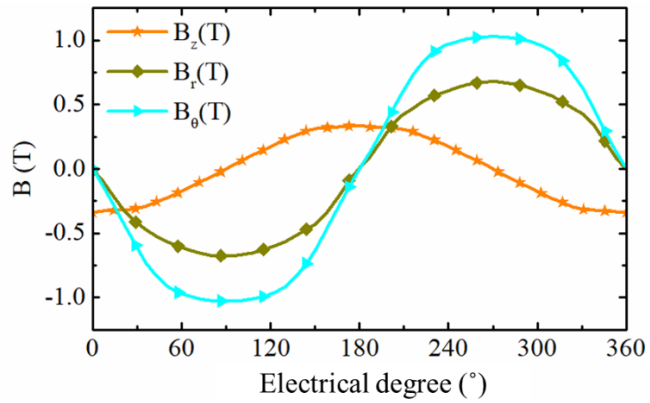

(b) The magnitudes of the axial, radial, circumferential components of the flux density vector.

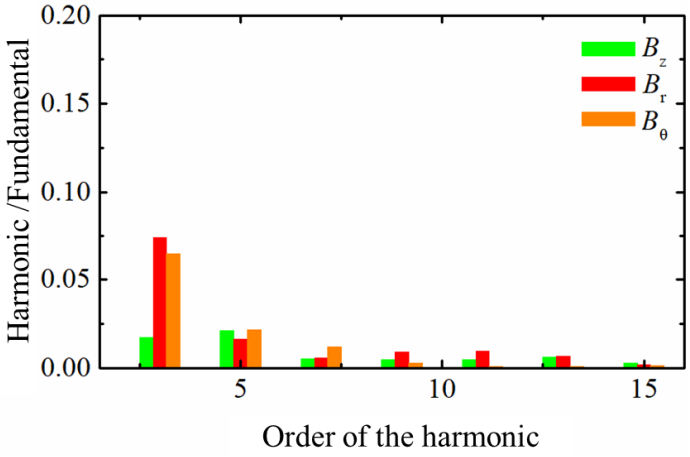

(c) Amplitude relationships between harmonics and fundamentals.

Fig. 3-6 Magnetic flux density characteristics at point 4.

Similar to the magnetic flux density trajectory at point 4, the magnetic flux density trajectory at point 5 is also a relatively smooth approximate ellipse, as shown in Fig. 3-7 (a). The axial magnetic flux density B_z, radial magnetic flux density B_r and circumferential magnetic flux density B_θ at different positions of the rotor are all varying approximately sinusoidally, respectively with the magnitude of 0.84 T, 0.78 T, and 0.62 T, as illustrated in Fig. 3-7 (b). Fig. 3-7 (c) gives the amplitude relationships between harmonics and fundamentals of these three components. The 3rd harmonics of each magnetic flux density component account for 1.3%, 3% and 8.7% of the fundamental, respectively.

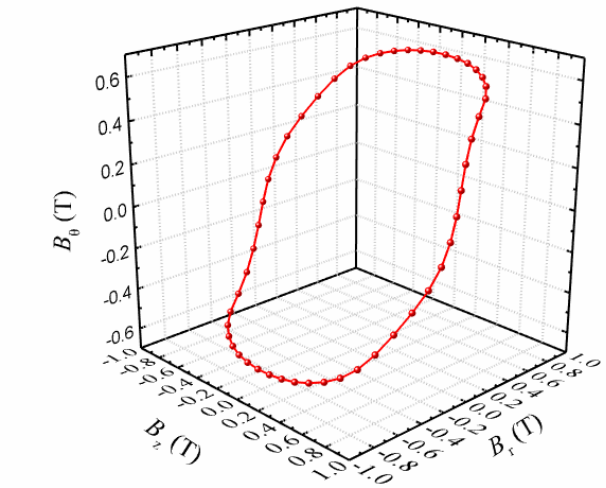

(a) 3-D trajectory of the flux density vector.

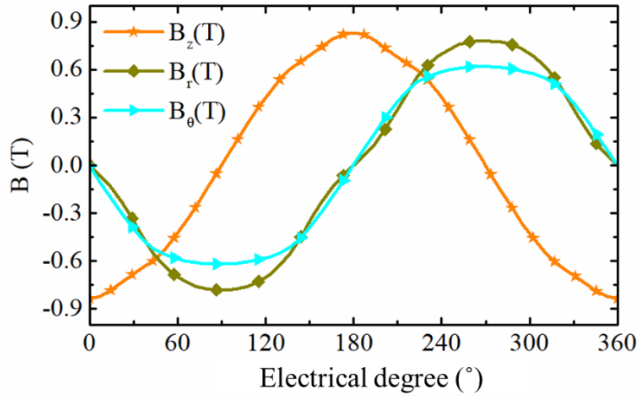

(b) The magnitudes of the axial, radial, circumferential components of the flux density vector.

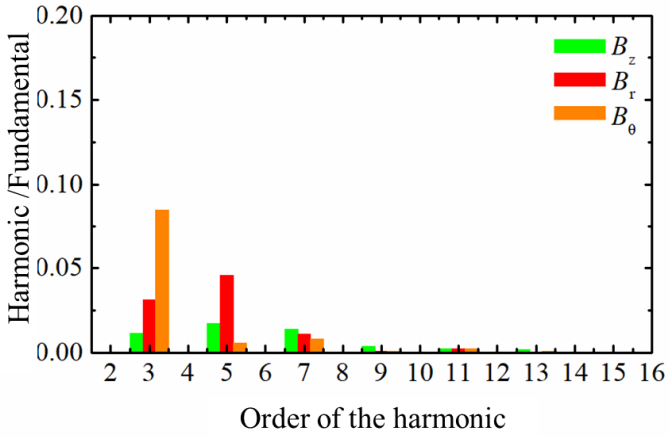

(c) Amplitude relationships between harmonics and fundamentals.

Fig. 3-7 Magnetic flux density characteristics at point 5.

From Figs. 3-3 to 3-7, conclusions can be drawn as follows:

(1) In an electrical cycle, the magnetic flux density trajectory at any point in the stator of the claw pole PMSM is of 3-D pattern, in which the magnetic flux density trajectories at the yoke of the stator are close to the alternating pattern and that at the bottom of the stator are near the elliptical rotating pattern.
(2) These 3-D magnetic flux density trajectories contain a large number of high-order harmonics, and with the proportion of the high-order harmonics to the fundamental increases, the distortion of the trajectory becomes significant.

To analyse the magnetic flux density of the claw pole PMSM furtherly, the axial magnetic flux density B_z, radial magnetic flux density B_r and circumferential magnetic flux density B_θ at 5 points in Fig. 3-2 are expanded according to the Fourier series, and the trajectories of magnetic flux density are reorganised by using the fundamental, the third harmonic, and the fifth harmonic of B_z, B_r, and B_θ, respectively.

Fig. 3-8 (a) illustrates the trajectory of the magnetic flux density at point 1 of the claw pole PMSM, while Figs. 3-8 (b)-(d) are the reformed trajectories of the fundamental, 3rd harmonic, and 5th harmonic of the axial magnetic flux density B_z, radial magnetic flux density B_r and circumferential magnetic flux density B_θ, respectively. It is obvious that the magnetic flux density trajectories of the fundamental, 3rd harmonic, and 5th harmonic are all one-dimensional alternating patterns. The trajectory shown in Fig. 3-8 (a) can be considered as vectors superposition of Figs. 3-8 (b)-(d) as well as remaining higher harmonic of the magnetic flux density.

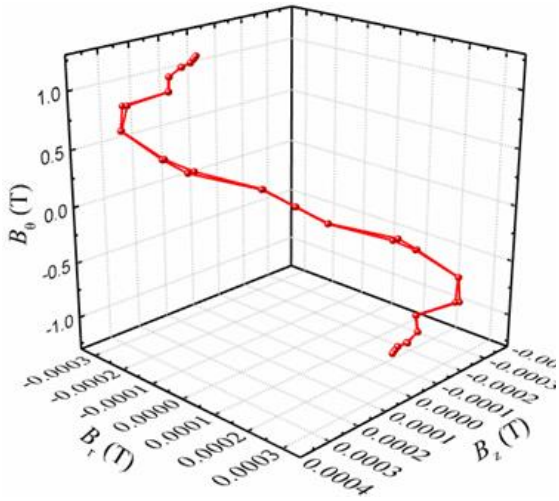

(a) Trajectory of the flux density.

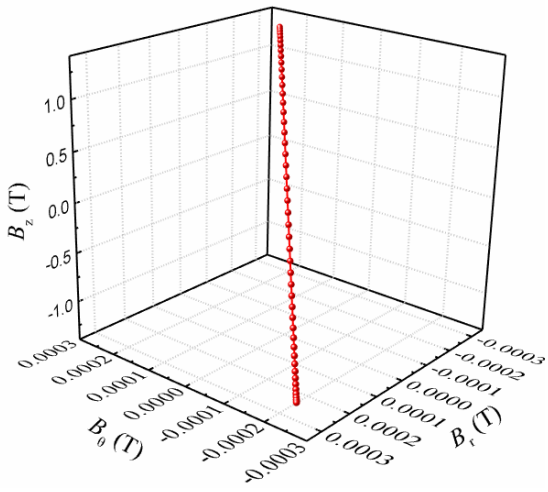

(b) Trajectory of the fundamental of the flux density.

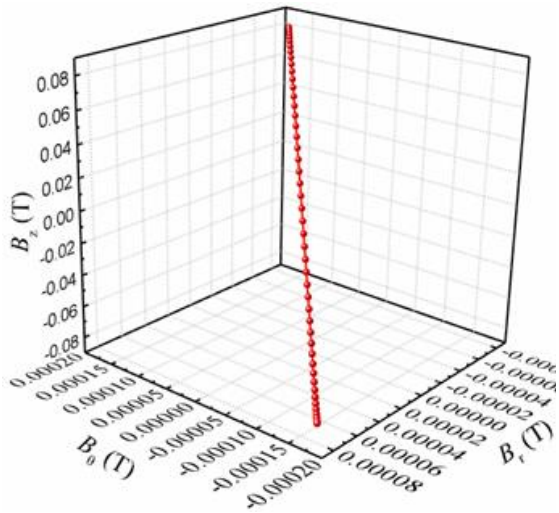

(c) Trajectory of the 3rd harmonic of the flux density.

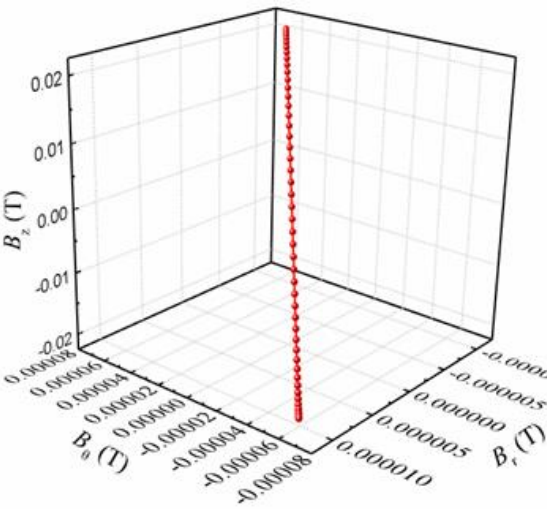

(d) Trajectory of the 5th harmonic of the flux density.

Fig. 3-8 Trajectories of the flux density at point 1.

Figs. 3-9 (a)-(d) illustrate the trajectories of the magnetic flux density, the fundamental, 3rd harmonic, and 5th harmonic of the magnetic flux density at point 2 of the claw pole PMSM, respectively. Although the magnetic flux density trajectories of the fundamental, 3rd harmonic, and 5th harmonic are all one-dimensional alternating patterns in the 3-D space, the amplitude and direction of each alternating trajectory are different.

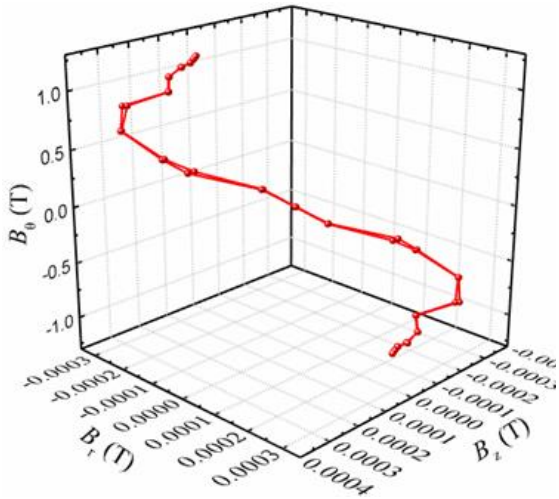

(a) Trajectory of the flux density.

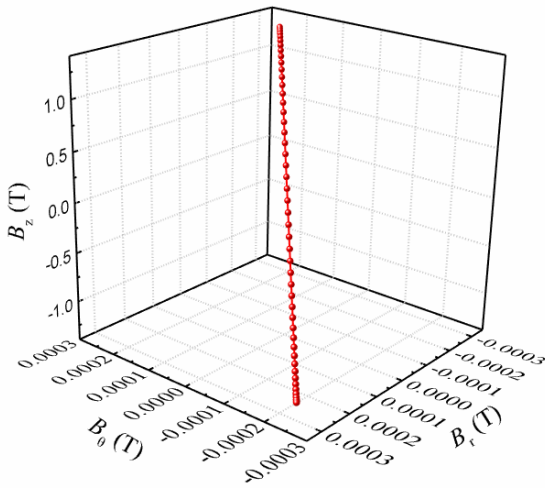

(b) Trajectory of the fundamental of the flux density.

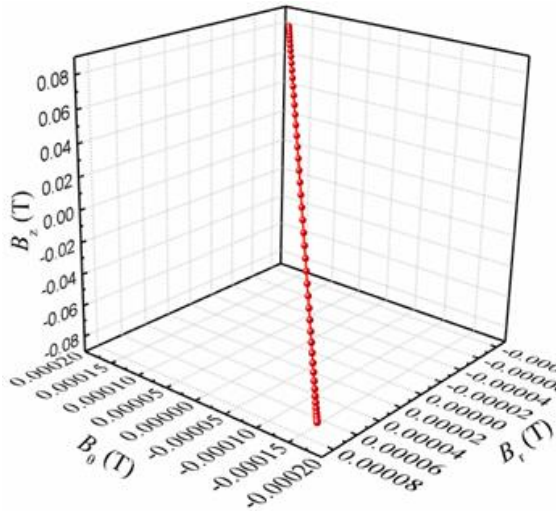

(c) Trajectory of the 3rd harmonic of the flux density.

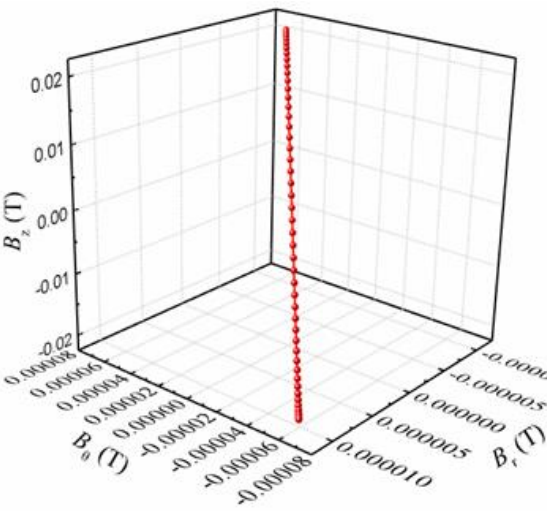

(d) Trajectory of the 5th harmonic of the flux density.

Fig. 3-9 Trajectories of the flux density at point 2.

The trajectory of the magnetic flux density at point 3 of the claw pole PMSM is shown in Fig. 3-10 (a), which is approximately an irregular quadrilateral. However, the trajectories of the fundamental, 3rd harmonic, and 5th harmonic of the magnetic flux density at point 3 are standard ellipses, as shown in Figs. 3-10 (b)-(d), respectively. A deep observation of these elliptical trajectories suggests that the amplitudes, axial rates, and spatial positions of them are all inconsistent.

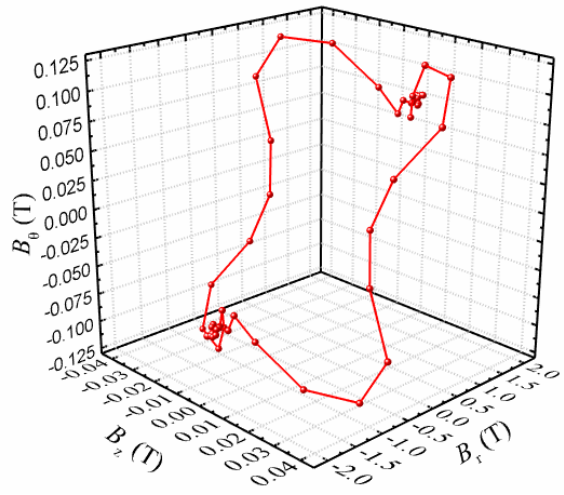

(a) Trajectory of the flux density.

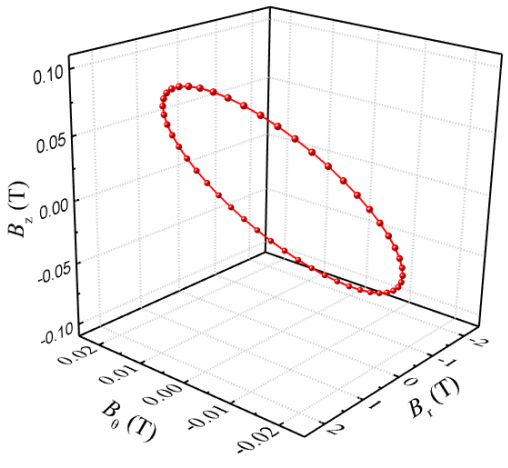

(b) Trajectory of the fundamental of the flux density.

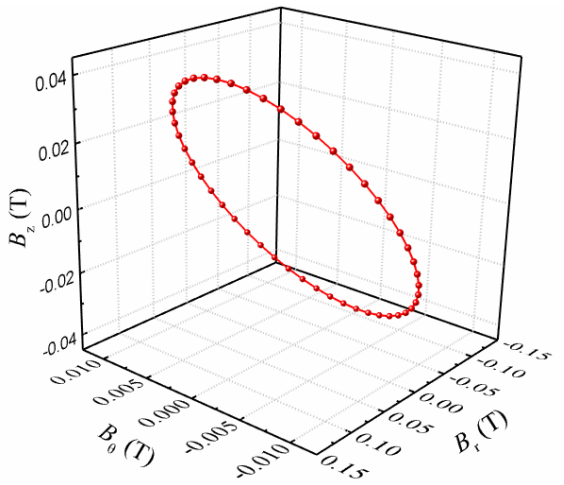

(c) Trajectory of the 3rd harmonic of the flux density.

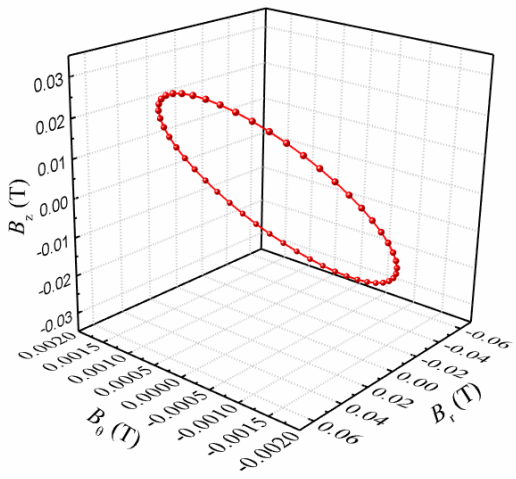

(d) Trajectory of the 5th harmonic of the flux density.

Fig. 3-10 Trajectories of the flux density at point 3.

Similar to Fig. 3-10, Fig. 3-11 demonstrates the trajectories of the magnetic flux density at point 4. The approximately irregular ellipse, as shown in Fig. 3-11 (a), is the vector summation of standard ellipses with different main axis lengths, axial ratios and spatial positions. The standard elliptical trajectories of the fundamental, 3rd harmonic, and 5th harmonic of the magnetic flux density are depicted in Figs. 3-9 (b)-(d).

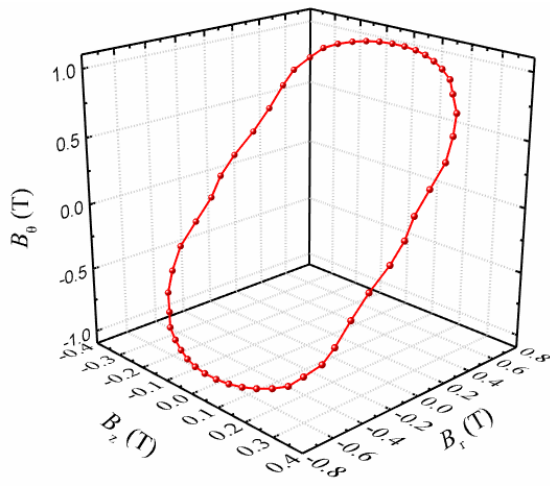

(a) Trajectory of the flux density.

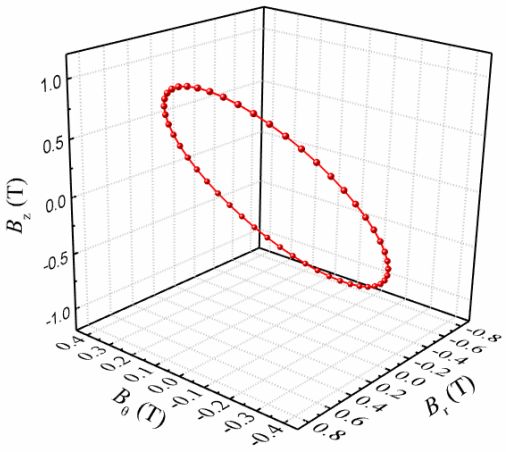

(b) Trajectory of the fundamental of the flux density.

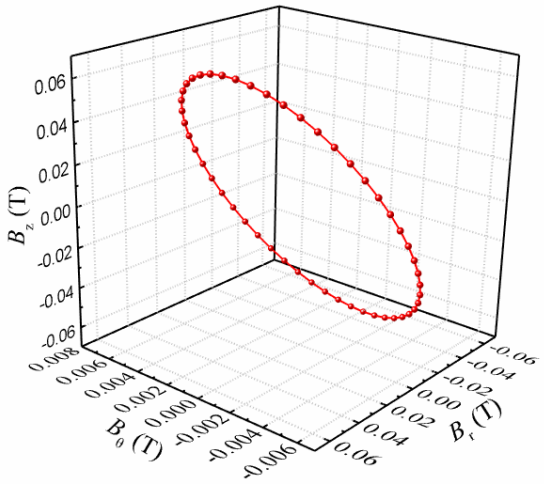

(c) Trajectory of the 3rd harmonic of the flux density.

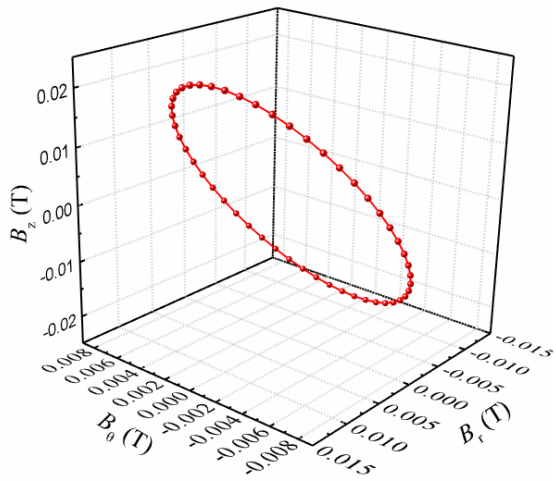

(d) Trajectory of the 5th harmonic of the flux density.

Fig. 3-11 Trajectories of the flux density at point 4.

Figs. 3-12 (a)-(d) display the trajectories of the magnetic flux density, the fundamental, 3rd harmonic, and 5th harmonic of the magnetic flux density at point 5 of the claw pole PMSM, respectively. Although the magnetic flux density trajectories of the fundamental, 3rd harmonic, and 5th harmonic are all two-dimensional rotating patterns in the 3-D space, the directions of the main axes of the elliptical trajectories are not parallel to any reference axis in the 3-D coordinate system.

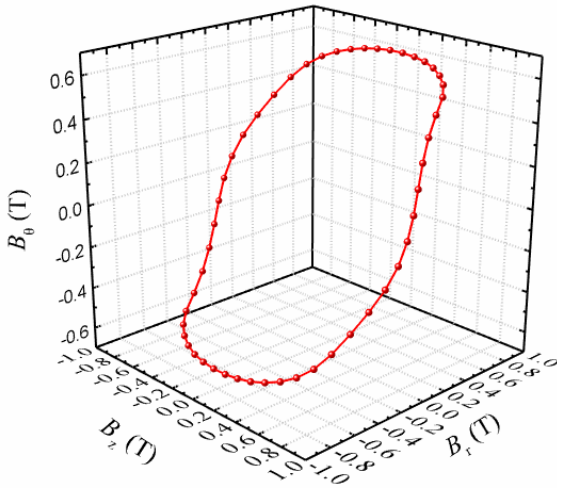

(a) Trajectory of the flux density.

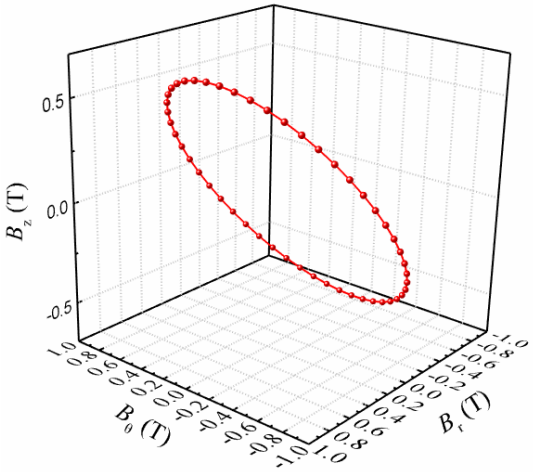

(b) Trajectory of the fundamental of the flux density.

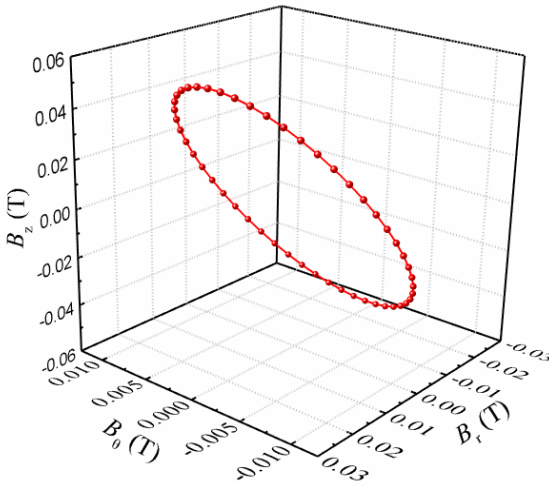

(c) Trajectory of the 3rd harmonic of the flux density.

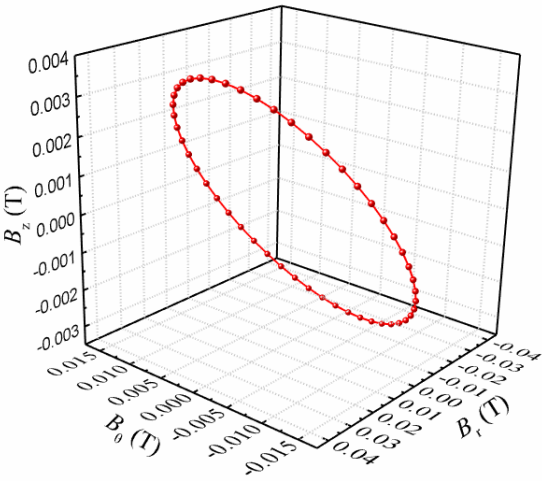

(d) Trajectory of the 5th harmonic of the flux density.

Fig. 3-12 Trajectories of the flux density at point 5.

In conclusion, Figs. 3-8 to 3-12 show that:

(1) The 3-D trajectory of the magnetic flux density at any point in the stator of the claw pole PMSM is the vector summation of the trajectories of magnetic flux density's fundamental and high-order harmonics.

(2) Either fundamental or high-order harmonics of the magnetic flux density, the trajectories of them just fall into two categories: 1-D alternating pattern like a straight line and 2-D rotating pattern like an ellipse.

Therefore, it is necessary to develop the core loss calculation models when the applied magnetic field varies in the 1-D alternating pattern or 2-D rotating pattern, namely the alternating core loss and rotating core loss calculation models.

3.3 Core Loss with the 3-D Rotating Magnetic Fields

3.3.1 1-D Alternating Core Loss

The most general practice for computing the core loss is to divide it into two or three terms, i.e., the hysteresis loss, eddy current loss, and anomalous loss, while two terms model does not have the anomalous loss. Assuming the excitation magnetic field is 1-D alternating, the alternating core loss can be calculated as [87-91]

$$P_a = P_{ha} + P_{ea} + P_{aa} = C_{ha} f B_m^h + C_{ea} \left(f B_m \right)^2 + C_{aa} \left(f B_m \right)^{3/2} \tag{3.1}$$

where P_{ha}, P_{ea}, and P_{aa} represent respectively the alternating hysteresis, eddy current, and anomalous loss, and f and B_m are the flux density frequency and peak value, while C_{ha}, C_{ea}, C_{aa}, and h are coefficients depending on material properties.

3.3.2 2-D Rotating Core Loss

Similar to the 1-D alternating core loss, the 2-D rotating core loss can also be separated into rotating hysteresis, eddy current, anomalous loss

$$P_r = P_{hr} + P_{er} + P_{ar} \tag{3.2}$$

where P_{hr}, P_{er}, and P_{ar} represent respectively the rotating hysteresis, eddy current, and anomalous loss.

If the trajectory of the 2-D exciting magnetic field is a standard circle, the rotating eddy current loss can be calculated by

$$P_{er} = C_{er} \left(fB \right)^2 = 2 C_e \left(fB \right)^2 \tag{3.3}$$

$$C_e = \frac{\pi^2 b^2 \sigma}{6 \rho_m} \tag{3.4}$$

where C_e is the coefficient of the eddy current loss, which is the same for both alternating and rotating core loss, and f and B are the frequency and magnitude of the circular rotating magnetic flux density. Moreover, b is the thickness of the electrical steel sheet, σ the conductivity, and ρ_m the mass density.

The rotating anomalous loss is obtained by

$$P_{ar} = C_{ar}\left(fB\right)^{3/2} \tag{3.5}$$

where C_{ar} is the coefficient of the rotating anomalous loss and it is a function of the magnetic flux density. C_{ar} eventually reduces to zero when the core material is magnetic saturated and all magnetic domain walls disappear.

The rotating hysteresis loss is quite different from that with the alternating counterpart. Some models have been developed and applied, and one example with high-accuracy is shown below [92-95].

$$\frac{P_{\mathrm{hr}}}{f} = a_1\left[\frac{1/s}{(a_2+1/s)^2+a_3^2} - \frac{1/(2-s)}{[a_2+1/(2-s)]^2+a_3^2}\right] \tag{3.6}$$

$$s = 1 - \frac{B}{B_s}\sqrt{1-1/a_2^2+a_3^2} \tag{3.7}$$

where B_s is the saturation value of the rotating magnetic flux density, and a_1, a_2, a_3, and s are all coefficients.

However, from the research of the magnetic flux distribution of the PMSM we know that the most common trajectory of the magnetic flux density is an ellipse rather than a circle. Therefore, the elliptically rotating core loss calculation model will be established in this section.

If the trajectory of the magnetic flux density $\boldsymbol{B}$ in the stator core of the PMSM is an ellipse, the applied rotating magnetic field strength $\boldsymbol{H}$ may not be an elliptically rotating vector due to the magnetic anisotropy of the core material and the nonlinear relationship between $\boldsymbol{B}$-$\boldsymbol{H}$. Expanding the magnetic field strength $\boldsymbol{H}$ into a Fourier series, the higher harmonics

of it do not contribute the total core loss as long as $\boldsymbol{B}$ contains only the fundamental component.

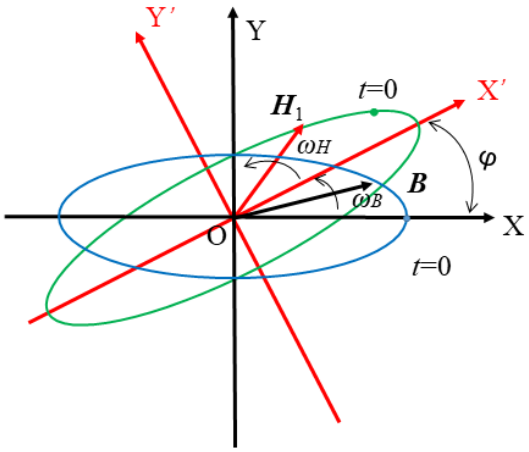

Fig. 3-13 Trajectories of elliptical $\boldsymbol{B}$ and $\boldsymbol{H_1}$ vectors.

Fig. 3-13 depicts the trajectories of the magnetic flux density $\boldsymbol{B}$ and the fundamental component of magnetic field strength $\boldsymbol{H_1}$, and they can be expressed as

$$\begin{cases} B_x = B_{\text{maj}} \cos(\omega t) \\ B_y = B_{\text{min}} \sin(\omega t) \end{cases} \tag{3.8}$$

$$\begin{cases} H_{1x'} = H_{1\text{maj}} \cos(\omega t + \varphi) \\ H_{1y'} = H_{1\text{min}} \sin(\omega t + \varphi) \end{cases} \tag{3.9}$$

where B_x and B_y are respectively the X and Y components of $\boldsymbol{B}$ in the XOY coordinate system, B_{maj} and B_{min} the major and minor axes of elliptical $\boldsymbol{B}$, and ω is the angular frequency of magnetisation. $H_{1x'}$ and $H_{1y'}$ are respectively the X' and Y' component of $\boldsymbol{H_1}$ in the X'OY' coordinate system, H_{1maj} and H_{1min} the major and minor axes of elliptical $\boldsymbol{H_1}$, and φ is the phase angle by which $\boldsymbol{H_1}$ leads $\boldsymbol{B}$ in time.

Equation (3.9) can be transferred into the XOY coordinate system by multiplying a transformation matrix

$$\begin{pmatrix} H_{1x} \\ H_{1y} \end{pmatrix} = \begin{pmatrix} \cos\alpha & -\sin\alpha \\ \sin\alpha & \cos\alpha \end{pmatrix} \begin{pmatrix} H_{1x'} \\ H_{1y'} \end{pmatrix} \tag{3.10}$$

Therefore, the total elliptically rotating core loss can be computed as

$$\begin{aligned} P_t &= \frac{1}{T\rho_m}\int_0^T \left(H \cdot \frac{dB}{dt} \right) dt = \frac{1}{T\rho_m}\int_0^T \left(H_x \cdot \frac{dB_x}{dt} + H_y \cdot \frac{dB_y}{dt} \right) dt \\ &= \frac{1}{T\rho_m}\int_0^{2\pi} \begin{pmatrix} \left(-B_{maj}\sin(\omega t)\right) \times \left[H_{1maj}\cos(\omega t+\varphi)\cos\alpha - H_{1\min}\sin(\omega t+\varphi)\sin\alpha \right] \\ +\left(B_{\min}\cos(\omega t)\right) \times \left[H_{1maj}\cos(\omega t+\varphi)\sin\alpha + H_{1\min}\sin(\omega t+\varphi)\cos\alpha \right] \end{pmatrix} d(\omega t) \\ &= \frac{\pi}{T\rho_m}\left[\left(B_{maj}H_{1\min} + B_{\min}H_{1maj}\right)\sin(\alpha+\varphi) + \left(B_{maj} - B_{\min}\right)\left(H_{1maj} - H_{1\min}\right)\cos\alpha\sin\varphi \right] \\ &= \frac{\pi}{T\rho_m} B_{maj}H_{1maj}\left[\left(R_H + R_B\right)\sin(\alpha+\varphi) + \left(1-R_B\right)\left(1-R_H\right)\cos\alpha\sin\varphi \right] \end{aligned} \tag{3.11}$$

where $T=1/f$ is the time period of magnetisation, ρ_m the mass density of the core material, and $R_B=B_{min}/B_{maj}$ and $R_H=H_{1min}/H_{1maj}$ are the axis ratio of elliptical $\boldsymbol{B}$ and $\boldsymbol{H_1}$, respectively.

If the core material has isotropic magnetic property, R_H equals R_B, and hence the above equation can be rewritten as

$$P_t = \frac{\pi}{T\rho_m} B_{maj}H_{1maj}\left[2R_B\sin(\alpha+\varphi) + \left(1-R_B\right)^2\cos\alpha\sin\varphi \right] \tag{3.12}$$

When R_B =1, the total rotating core loss in an isotropic material with a purely circular flux density is

$$P_{cr} = \frac{2\pi}{T\rho_m} B_{maj}H_{1maj}\sin(\alpha+\varphi) \tag{3.13}$$

When R_B = 0, the total rotating core loss in an isotropic material with a purely alternating flux density is

$$P_{alt} = \frac{\pi}{T\rho_m} B_{maj}H_{1maj}\cos\alpha\sin\varphi \tag{3.14}$$

Therefore, (3.12) can be rewritten as

$$P_t = R_B P_{cr} + \left(1 - R_B\right)^2 P_{alt} \tag{3.15}$$

Equation (3.15) is independent of the magnetisation frequency, since it is derived directly from the formula of the total rotating core loss, which is valid for any magnetisation frequency, and should be applicable to both hysteresis and total core loss.

3.3.3 3-D Rotating Core Loss

In an element of the finite element method (FEM), the three items core loss calculation model still can be applied even the magnetic flux density contains higher harmonics

$$P_t = P_{th} + P_{te} + P_{ta} \tag{3.16}$$

where P_t is the total core loss considering higher harmonics in an element of the FEM, while P_{th}, P_{te}, and P_{ta} represent respectively the total hysteresis, eddy current, and anomalous losses considering higher harmonics in an element of the FEM.

For arbitrary 3-D magnetic flux density trajectory in an FEM element of the PMSM, the radial magnetic flux density B_r, circumferential magnetic flux density B_θ and axial magnetic flux density B_z can be expanded as follows according to the Fourier series

$$\begin{aligned} B_r(t) &= \sum_{k=0}^{\infty}\left[B_{rsk}\sin\left(2\pi kft\right) + B_{rck}\cos\left(2\pi kft\right)\right] \\ &= \sum_{k=0}^{\infty} B_{rmk}\sin\left(2\pi kft + \phi_{rk}\right) \end{aligned} \tag{3.17}$$

$$\begin{aligned} B_\theta(t) &= \sum_{k=0}^{\infty}\left[B_{\theta sk}\sin\left(2\pi kft\right) + B_{\theta ck}\cos\left(2\pi kft\right)\right] \\ &= \sum_{k=0}^{\infty} B_{\theta mk}\sin\left(2\pi kft + \phi_{\theta k}\right) \end{aligned} \tag{3.18}$$

$$\begin{aligned} B_z(t) &= \sum_{k=0}^{\infty}\left[B_{zsk}\sin\left(2\pi kft\right) + B_{zck}\cos\left(2\pi kft\right)\right] \\ &= \sum_{k=0}^{\infty} B_{zmk}\sin\left(2\pi kft + \phi_{zk}\right) \end{aligned} \tag{3.19}$$

where B_{rmk}, $B_{\theta mk}$, B_{zmk} are the magnitudes of the k-th harmonics of B_r, B_θ, B_z, and ϕ_{rk}, $\phi_{\theta k}$, ϕ_{zk} are the phase angles of these harmonics.

Any order harmonic of these three components will reform an elliptical trajectory in a plane, which may not be parallel to any coordinate axis. The two axes can be calculated by

$$B_{msk} = \sqrt{B_{rsk}^2 + B_{\theta sk}^2 + B_{zsk}^2} \tag{3.20}$$

$$B_{mck} = \sqrt{B_{rck}^2 + B_{\theta ck}^2 + B_{zck}^2} \tag{3.21}$$

The larger of B_{msk} and B_{mck} is taken as the major axis B_{kmaj}, and the other as the minor axis B_{kmin} of the k-th harmonic of the elliptical flux density vector.

The total hysteresis loss in an FEM element can be obtained by summing up the contributions from these flux density harmonics. For each elliptically rotating flux density harmonic, the loss can be predicted from the corresponding alternating and rotating losses according to the axis ratio of the elliptical flux density. Therefore, the total hysteresis loss P_{th} in an FEM element is

$$P_{th} = \sum_{k=0}^{\infty} \left[P_{rhk} R_{Bk} + \left(1 - R_{Bk}\right)^2 P_{ahk} \right] \tag{3.22}$$

where R_{BK}=B_{kmin}/B_{kmaj} is the axis ratio of the k-th harmonic flux density, P_{rk} is the purely rotating hysteresis loss with flux density B_{kmaj}, and P_{ak} is the alternating hysteresis loss with flux density magnitude of B_{kmaj}.

Moreover, the total eddy current loss P_{te} and total anomalous loss P_{ta} in an FEM element are as follows

$$P_{te} = C_e \sum_{k=0}^{\infty} \left(kf\right)^2 \left(B_{kmaj}^2 + B_{k\min}^2\right) \tag{3.23}$$

$$P_{ta} = \frac{C_{ar}}{\left(2\pi\right)^{3/2}} \frac{1}{T} \int_0^T \left[\left(\frac{dB_{rmk}\left(t\right)}{dt} \right)^2 + \left(\frac{dB_{\theta mk}\left(t\right)}{dt} \right)^2 + \left(\frac{dB_{zmk}\left(t\right)}{dt} \right)^2 \right]^{3/4} dt \tag{3.24}$$

The core loss for the entire PMSM can be computed as

$$P_{\text{motor}} = \sum_{e=1}^{Ne} \left(P_{th} + P_{te} + P_{ta} \right) \tag{3.25}$$

where N_e is the number of FEM elements for the entire PMSM.

3.4 Modelling the Core Loss in the Equivalent Circuit Models

Using the equivalent electric circuit is a common way to predict the motor performance in the field of electrical machine design, analysis and control. The machine is represented by lumped parameters such as rotating electromotive force (EMF), resistances and inductances.

Fig. 3-14 illustrates schematically the cross section of a three phase, two pole cylindrical rotor PMSM. Coils *aa'*, *bb'*, and *cc'* represent the distributed stator windings producing sinusoidal magnetomotive force (*mmf*) and flux density waves rotating in the air gap. The reference directions for the currents are shown by dots and crosses. The magnetic axis of the permanent magnets is rotating with the rotor.

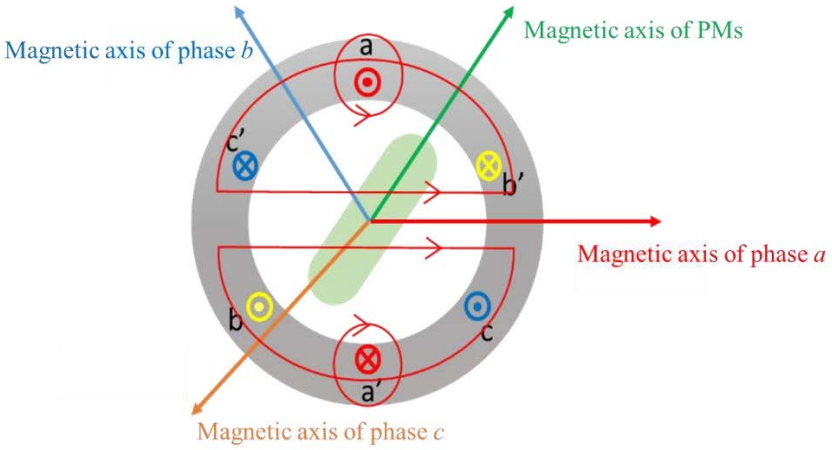

Fig. 3-14 Cross section of a three phase PMSM.

Taking phase *a* as an example, the electrical circuit equation for per-phase of the PMSM can be written by the Kirchhoff's voltage law as

$$v_a = R_a i_a + d\lambda_a / dt \tag{3.26}$$

where v_a and i_a are the terminal voltage and phase current of the PMSM, R_a is the stator winding resistance, and λ_a the flux linkage of phase winding, which can be expressed in terms of the leakage linkage and the magnetizing linkage as the following

$$\lambda_a = \lambda_{al} + \lambda_{am} \tag{3.27}$$

where λ_{al} is the leakage linkage of phase a, which links only the stator wingding a, and λ_{am} is the magnetizing linkage which links all three phase of stator windings. To be more specific, the magnetizing linkage λ_{am} also can be expressed as

$$\lambda_{am} = \lambda_{aa} + \lambda_{ab} + \lambda_{ac} + \lambda_{af} \tag{3.28}$$

where λ_{aa} is the flux linkage of phase a generated by phase a current, λ_{ab} the flux linkage of phase a generated by phase b current, λ_{ac} the flux linkage of phase a generated by phase c current, and λ_{af} the component of the PM flux linkage on the magnetic axis of phase a.

Thus, the flux linkage of phase winding a can be rewritten as

$$\lambda_a = \lambda_{al} + \lambda_{aa} + \lambda_{ab} + \lambda_{ac} + \lambda_{af} \tag{3.29}$$

Taking the time derivative of both sides of the above equation, one can obtain

$$\begin{aligned} \frac{d\lambda_a}{dt} &= \frac{d\lambda_{al}}{di_a}\frac{di_a}{dt} + \frac{\partial\lambda_{am}}{\partial i_a}\frac{di_a}{dt} + \frac{\partial\lambda_{am}}{\partial i_b}\frac{di_b}{dt} + \frac{\partial\lambda_{am}}{\partial i_c}\frac{di_c}{dt} + \frac{d\lambda_{af}}{dt} \\ &= L_{al}^{diff}\frac{di_a}{dt} + L_{aa}^{diff}\frac{di_a}{dt} + L_{ab}^{diff}\frac{di_b}{dt} + L_{ac}^{diff}\frac{di_c}{dt} + \frac{d\lambda_{af}}{dt} \end{aligned} \tag{3.30}$$

where L_{al} is the differential leakage inductance of phase a; L_{aa} the differential self-inductance; while L_{ab} and L_{ac} are differential mutual inductances.

For a symmetric three-phase stator winding of the PMSM, the relationships of inductances are as follows

$$L_{ab}=L_{ac}=-\frac{1}{2}L_{aa} \tag{3.31}$$

When the stator windings are excited by balanced three-phase currents, we have

$$\frac{di_b}{dt}+\frac{di_c}{dt}=-\frac{di_a}{dt} \tag{3.32}$$

Thus, equitation (3.30) can be rewritten as

$$\frac{d\lambda_a}{dt}=L_{al}^{diff}\frac{di_a}{dt}+\frac{3L_{aa}^{diff}}{2}\frac{di_a}{dt}+\frac{d\lambda_{af}}{dt} \tag{3.33}$$

Therefore, the electrical circuit equation for single phase *a* can be rewritten as

$$v_a=R_a i_a+L_s^{diff}\frac{di_a}{dt}+\frac{d\lambda_{af}}{dt} \tag{3.34}$$

$$L_s^{diff}=\frac{3L_{aa}^{diff}}{2}+L_{al}^{diff} \tag{3.35}$$

where L_s^{diff} is known as the differential synchronous inductance, and $d\lambda_{af}/dt$ is the induced electromotive force (*emf*).

According to the above equation, the equivalent circuit model (ECM) of the per phase of the PMSM can be illustrated as shown in Fig. 3-15.

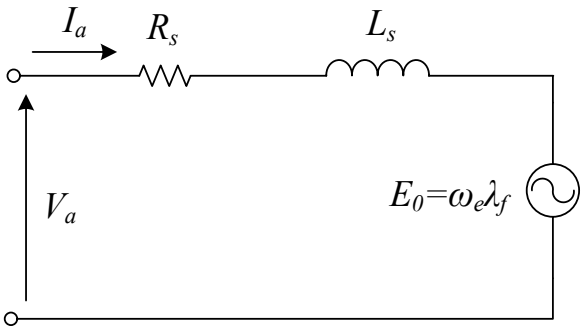

Fig. 3-15 Per phase ECM of the PMSM.

However, in electrical machines, there are mainly two kinds of electromagnetic loss, i.e., the copper loss and the core loss. In Fig. 3-15, the copper loss is incorporated by using a

winding resistance R_a, while the core loss is neglected in this equivalent circuit model. In order to establish an equivalent circuit model which can predict the performance of the PMSM comprehensively, the core loss should be taken into account.

If a resistance is used to represent the core loss due to the magnetizing linkage, the power consumed by this resistance should be calculated as

$$P_{core} = \frac{V_c^2}{R_c} \tag{3.36}$$

where P_{core} is the power consumed by the equivalent core loss resistance caused by the flux linkage; R_c the equivalent core loss resistance; V_c the voltage across the equivalent core loss resistance.

According to Faraday's law, we can obtain:

$$V_c = -\frac{d\lambda_a}{dt} \tag{3.37}$$

Therefore, the equivalent core loss resistance which represents the core loss caused by the magnetic flux should be connected in parallel with the magnetizing branch. Moreover, the equivalent circuit model of the PMSM with predictable core loss should be established as described in Fig. 3-16.

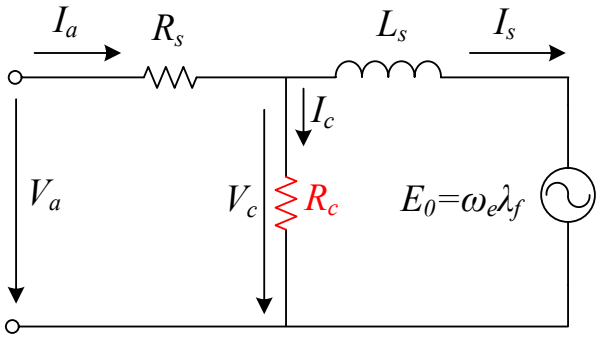

Fig. 3-16 Per phase ECM of the PMSM with predictable core loss.

3.5 Parameters Identification in the ECM of the Claw Pole PMSM

3.5.1 Back *EMF*

Considering the almost magnetic independence and structural symmetry, only one pole pitch of one stack of the motor needs to be calculated. Fig. 3-17 illustrates the no-load magnetic flux density vector distribution. The major path of the PM flux is along one of the PMs – the main air gap − half of the SMC claw pole stator core disk − the stator yoke − another half of SMC claw pole stator core disk − main air gap − another PM and then − the mild steel rotor yoke to form a closed loop.

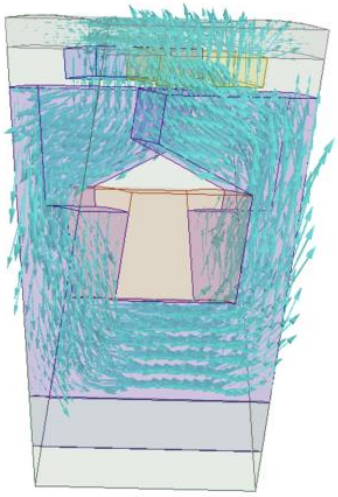

Fig. 3-17 Plots of magnetic flux density vectors.

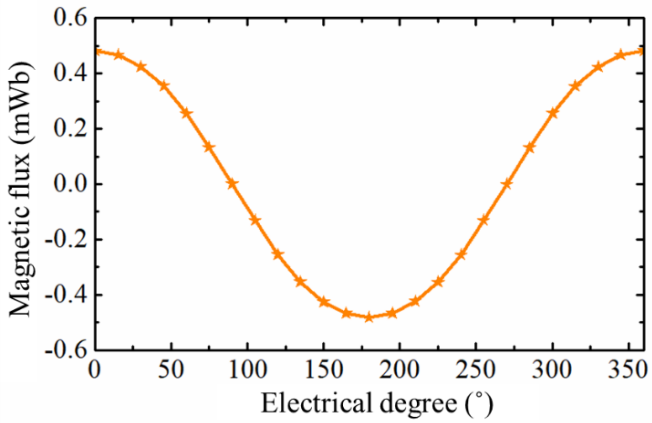

Fig. 3-18 Per turn no-load flux of a phase winding.

The flux waveform linking a stator phase winding produced by the rotor PMs can be calculated by rotating the rotor magnets for one pole pitch in steps. When the rotor rotates, the flux linking the stator winding varies and an EMF is induced. In this claw pole PM motor, the flux waveform is almost perfectly sinusoidal versus the rotor position, as plotted in Fig. 3-18.

Therefore, the back EMF can be determined as

$$E_0 = \sqrt{2}\pi f N k_{wa} \phi_m \tag{3.38}$$

where f is the frequency, N the number of turns of the stator winding, k_{wa} the winding factor of the phase winding, and ϕ_m is the magnitude of the magnetic flux linking the stator winding. In the claw pole PMSM, the concentrated winding is adopted, and hence k_{wa} =1. At 1800 rpm (300 Hz), E_0=48.9V, and the values of the back EFM are proportional to the rotor speeds.

3.5.2 Incremental Inductance

The behaviour of an electrical circuit is governed by the incremental inductance, also called differential inductance, rather than the secant inductance [96]. When considering the nonlinear characteristic of the core material, which is the case for changing loading conditions, using the secant inductance to analyse the performance of electrical machines is not very reasonable. Since the principle of the FEM is based on the minimization of magnetic field energy, choosing energy method, i.e., calculating the energy or co-energy stored in all the elements to evaluate inductances is considered as quite accurate. Thus, a modified incremental energy method for the calculation of the phase winding incremental inductance of the claw-pole motor is used [97]. However, in the case of PM machines, the magnetic field is generated not only by winding currents but also by PMs, and the former one just accounts for a small account. According to the modified incremental energy method, the self-incremental inductance can be computed as

$$L(\theta) = 2W_c(\Delta i, \theta)/(\Delta i)^2 \tag{3.39}$$

where W_c is the magnetic co-energy, and Δi is the stator perturbation.

Fig. 3-19 shows the computed self-incremental inductance as well as the computed secant inductance and measured inductance of one phase winding at different rotor positions. Since the fluctuation of the values of inductances is not significant, for simplification, the phase winding inductance can be considered as a constant, e.g., the average value over a variation cycle. Therefore, the average value of a phase winding's self-incremental inductance can be computed as L = 4.91 mH, while that of the self-secant inductance and measured inductance are 5.22 mH and 4.72 mH. In the claw pole PMSM, the three phase are magnetic independent, and hence the mutual inductances between phases can be regarded as zero, and then the synchronous inductance equals the self-inductance. At the rated operational frequency of 300 Hz, the synchronous reactance of the stator winding can be calculated as $X_s = 2\pi f L_s$ = 9.26 Ω.

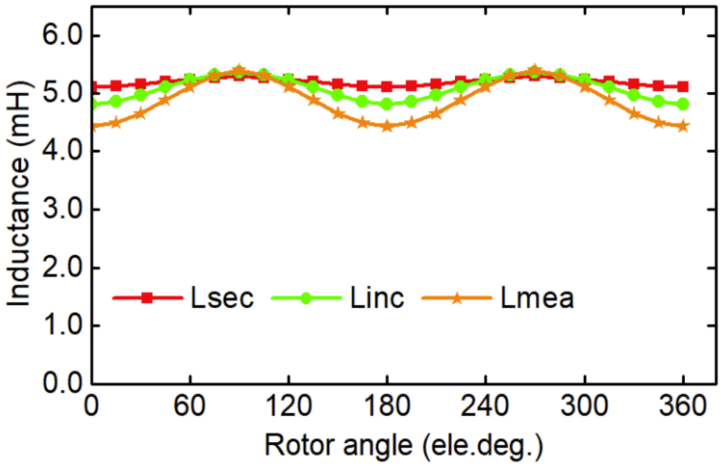

Fig. 3-19 Self-incremental, secant, and measured inductances.

3.5.3 Stator Winding Resistance

The stator winding resistance can be calculated as

$$R_s = \rho l / A \tag{3.40}$$

where l is the total wire length, A the wire cross sectional area, and ρ the electrical resistivity of the stator winding.

At the rated winding temperature of 115 ℃, representing a temperature rises of 75 ℃ above an ambient temperature 40 ℃, the resistance is calculated as 0.302 Ω.

3.5.4 Equivalent Core loss Resistance

Fig. 3-20 draws the measured alternating core loss of the SMC material at different frequencies [98]. Fitting the alternating core loss in Fig. 3-19 with the alternating core loss mathematical model (3.1), the coefficients in that are C_{ha}=0.1402, h=1.548, C_{ea}=1.233e^{-5}, and C_{aa}=3.645e^{-5}. Therefore, the proportion of each component of the core loss in the SMC core can be analyzed quantitatively. In the low frequency range, compared with the alternating hysteresis loss, the alternating eddy current loss and anomalous loss can be ignored. For example, the alternating eddy current loss and anomalous loss respectively account for 0.1% and 2.6% of the alternating hysteresis loss when the frequency is 100Hz.

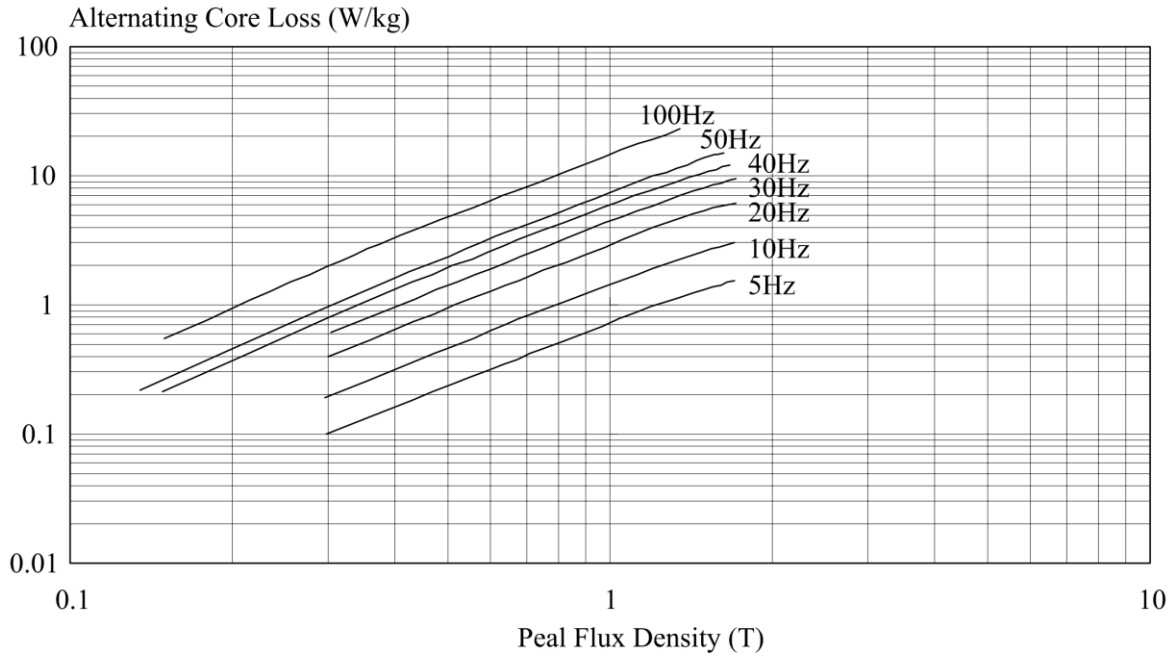

Fig. 3-20 Measured alternating core loss of the SMC material at different frequencies.

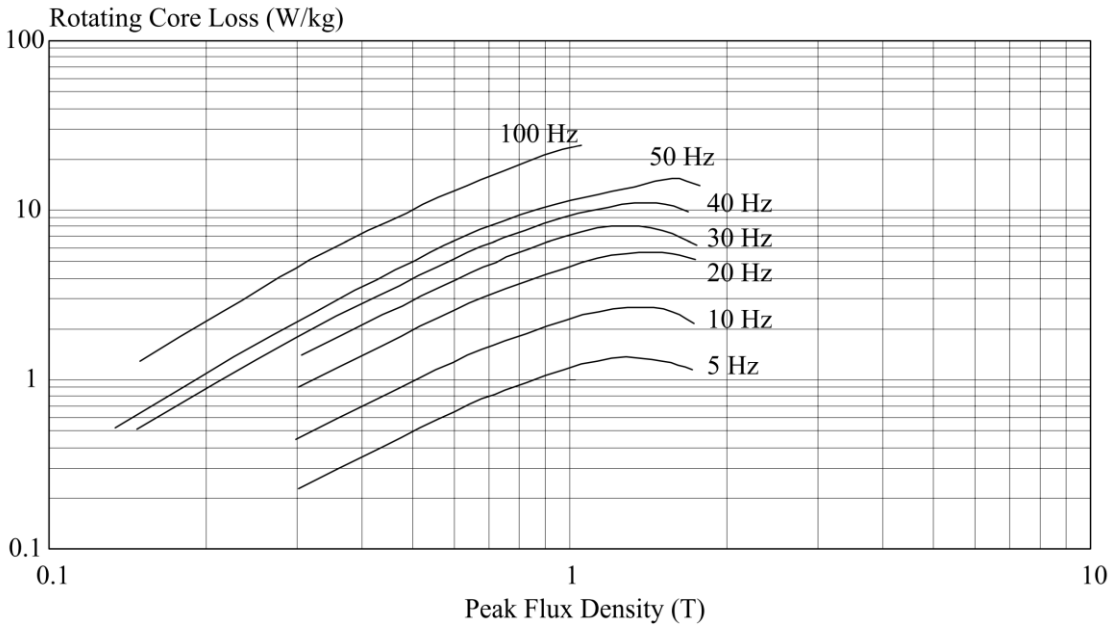

Fig. 3-21 Measured rotating core loss of the SMC material at different frequencies.

The measured rotating core loss of the SMC core at different frequencies are illustrated in Fig. 3-21. The coefficients in the rotating core loss calculation models (3.3) – (3.7) are calculated as C_{er}=2.303e^{-4}, C_{ar}=0, a_1=6.814, a_2=1.054, a_3=1.445, and B_s=2.134T by curve fitting the core loss data in Fig. 3-21.

In the no-load condition, the core loss of the claw pole PMSM based on the proposed 3-D core loss calculation models at different speeds is demonstrated in Table 3-2.

Table 3-2. Calculated core loss of the claw pole PMSM.

Speed (r/min)	Core Loss (W)
300	9.7
600	18.5
900	27.8
1200	38.5
1500	47.6
1800	57.5

According to the proposed ECM with predictable core loss as shown in Fig. 3-15, when the motor operates in the no-load conditions, $\boldsymbol{I_a}$ is considered as zero, then V_c and equivalent core loss resistance R_c can be calculated as

$$V_c = E_a \tag{3.41}$$

$$R_c = 3V_c^2 / P_{core} \tag{3.42}$$

where V_c is the magnitude of the voltage across the equivalent core loss resistance, and P_{core} the calculated core loss.

The variation of the equivalent core loss resistance R_c with respect to the motor speed is shown in Fig. 3-22. It is seen that the values of R_c vary almost in proportional to the rotor speeds (frequencies). This agrees with the dominant hysteresis loss of SMC, which is proportional to the excitation frequency.

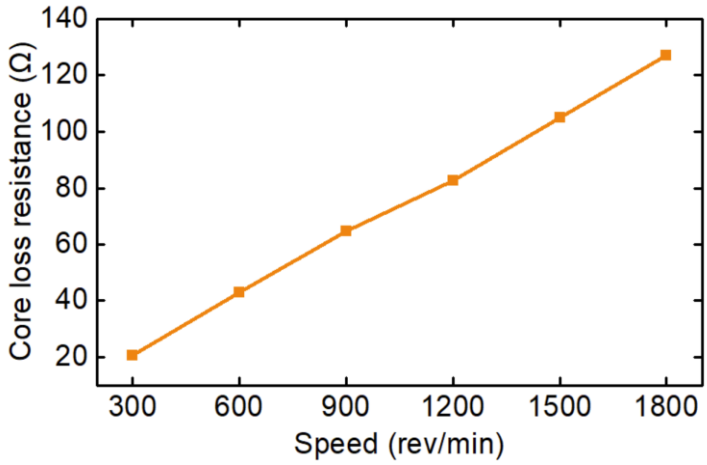

Fig. 3-22 Equivalent core loss resistance *Rc* with respect to the motor speed.

Therefore, we can conclude an equation for calculating the equivalent core loss resistance by curve-fitting as

$$R_c = 0.0702n \tag{3.43}$$

where n is the rotor speed of the claw pole PMSM.

3.6 Experimental Verifications of the Equivalent Core Loss Resistance in the Circuit Model

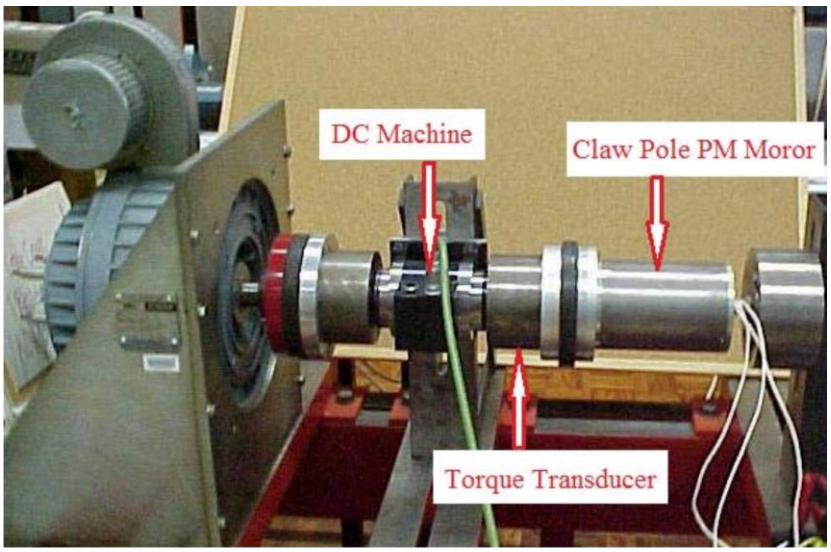

Fig. 3-23 Experimental platform of the claw pole PMSM.

Fig. 3-23 shows the experimental platform of the claw pole PMSM. The motor on the right side is the target claw pole PMSM, while the DC machine with variable speed drive system on the left side is the drive motor, and they are connected via a torque transducer (in the middle). The DC machine works as the drive motor when the prototype is operated as a generator or the load when the prototype is operated as a motor.

3.6.1 No-load Experimental Verifications

In the no-load experiments of the claw pole PMSM, it is operated as a generator, and its armature terminals are open-circuited. Thus, no current flows in the armature windings, resulting in no copper loss. The power feeds into the DC motor would be the summation of the core loss and mechanical loss (friction and windage) of both the DC motor and the claw pole PMSM. Subtracting the loss of the DC motor yields the core loss and mechanical loss of the claw pole PMSM alone. Table 5-3 shows the power fed into the DC machine when it drives the claw pole PMSM at different speeds, where V_{dc} is the applied DC voltage to the armature of the DC machine, I_{dc} the input current, E_a the back *emf*, and P_{em} the electromagnetic power.

Table 3-3. Power fed into the DC machine when it drives the claw pole PMSM at different speeds.

n (r/min)	V_{dc} (V)	I_{dc} (A)	E_a (V)	P_{em} (W)
104	6.4	1.29	4.1	5.3
196	10.2	1.32	7.8	10.4
299	14.3	1.40	11.8	16.6
401	18.5	1.44	16.0	22.9
508	23.0	1.50	20.4	30.7
608	27.2	1.55	24.4	38.0
705	31.2	1.60	28.4	45.3
816	35.6	1.65	32.7	54.1
898	39.0	1.70	36.0	61.2
1003	43.1	1.75	40.0	69.9
1115	47.8	1.81	44.6	80.6
1207	51.4	1.85	48.1	89.0
1292	55.0	1.89	51.7	97.8
1403	59.3	1.93	55.9	107.8
1507	63.5	1.99	60.0	119.6
1604	67.5	2.02	64.0	129.2
1710	71.9	2.09	68.2	142.6
1808	75.9	2.13	72.2	153.5

The mechanical loss of the claw pole PMSM is measured by replacing its stator with a wooden tube, and then repeating the previous test procedure. Therefore, the core loss of the claw pole PMSM is obtained by subtracting the mechanical loss from the summation of the core loss and mechanical loss. Table 3-4 exhibits the power fed into the DC motor when it drives the claw pole PMSM with a wooden stator.

It is assumed that the core loss and mechanical loss of the DC motor are constants at a certain speed. Therefore, the electromagnetic power in Table 3-3 subtracting that in Table 3-4 yields the core loss of the claw pole PMSM.

Table 3-4. Power fed into the DC machine when it drives the claw pole PMSM with a wooden stator.

n (r/min)	V_{dc} (V)	I_{dc} (A)	E_a (V)	P_{em} (W)
113	5.7	0.425	4.4	1.9
212	9.8	0.489	8.3	4.1
288	13.1	0.528	11.5	6.1
404	17.9	0.601	16.1	9.7
539	23.6	0.645	21.6	14.0
593	25.8	0.690	23.7	16.4
730	31.5	0.773	29.2	22.5
776	33.2	0.785	30.8	24.2
913	39.0	0.845	36.4	30.8
997	42.5	0.880	39.8	35.0
1106	46.8	0.928	44.0	40.8
1238	52.3	0.980	49.3	48.3
1279	54.0	1.01	50.9	51.4
1383	58.5	1.05	55.3	58.1
1519	64.0	1.11	60.6	67.3
1588	66.5	1.14	63.0	71.9
1671	70.2	1.18	66.6	78.6
1777	74.5	1.23	70.8	87.0

The comparisons between the measured core loss and calculated core loss based on the proposed ECM at different speeds under the no-load steady-state conditions are shown in Fig. 3-24. The calculated core loss is about 7% lower than the measured, which may be caused by the measurement error and some additional loss ignored in the calculation, e.g., the stray loss, eddy current loss of PMs, etc. To sum up, the proposed ECM and equivalent core loss resistance identification methods can effectively and accurately predict the core loss of the PMSM under no-load conditions with a wide speed range.

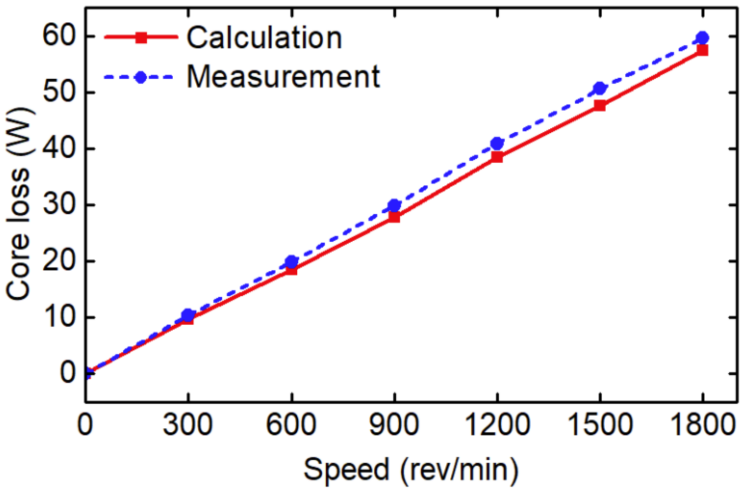

Fig. 3-24 Core loss measurement and calculation.

3.6.2 Load Experimental Verifications

The motor is assumed to operate in the optimum brushless DC mode, i.e. $\boldsymbol{I_s}$ in phase with $\boldsymbol{E_a}$, so that the electromagnetic power and torque can be obtained by

$$P_{em} = 3E_a I_s \cos\varphi = 3E_a I_s \tag{3.44}$$

$$T_{em} = P_{em}/\omega \tag{3.45}$$

where φ is the angle between phasors $\boldsymbol{E_a}$ and $\boldsymbol{I_s}$, and in the optimum brushless DC mode, φ=0.

In this claw pole PMSM, electromagnetic torque is a constant as: T_{em}=0.273 Nm.

Notice that the armature reaction in the SMC motor is quite small and it will not demagnetize the permanent magnets. That is to say, whether the motor works with no-load or load conditions, the distribution and strength of the magnetic field in the SMC core will hardly change, and then the core loss will not change significantly. Therefore, the calculated equivalent core loss resistance R_c by (3.43) can be used to predict the core loss in loading conditions, where phase current $|\boldsymbol{I_a}|$ >0, and then the core loss and copper loss can be predicted by

$$\boldsymbol{V}_c = \boldsymbol{E}_a - \mathrm{j}X_s\boldsymbol{I}_s \tag{3.46}$$

$$P_{\text{core}} = 3V_c^2 / R_c \tag{3.47}$$

$$\boldsymbol{I}_a = \frac{1}{R_c}\boldsymbol{E}_a + (1 - \mathrm{j}\frac{X_s}{R_c})\boldsymbol{I}_s \tag{3.48}$$

$$P_{\text{copper}} = 3I_a^2 R_s \tag{3.49}$$

where $\boldsymbol{V_c}$ is the voltage across the equivalent core loss resistance, $\boldsymbol{I_s}$ the current through the synchronous inductance, and $\boldsymbol{I_a}$ the phase current of the claw pole PMSM.

In the load conditions, the output power, input power, and efficiency of the claw pole PMSM are calculated by

$$P_{\text{out}} = P_{\text{em}} - P_{\text{mech}} \tag{3.50}$$

$$P_{\text{in}} = P_{\text{em}} + P_{\text{copper}} + P_{\text{core}} \tag{3.51}$$

$$\eta = P_{\text{out}} / P_{\text{in}} \times 100\% \tag{3.52}$$

where P_{mech} is the mechanical loss including windage and friction. In this claw pole PMSM, the mechanical loss accounts 3% of the output power approximately.

Based on the test platform as shown in Fig. 3-23, load experiments of the claw-pole PMSM with SMC core were established. The prototype was used as the prime mover, and the DC machine was used as the generator. The magnitude of the electrical load is adjusted by changing the value of variable resistances connected to the DC machine, thereby changing the phase current and output electromagnetic torque of the claw-pole PMSM. In load experiments, the input voltage of each phase of the PMSM is fixed at 68V.

Table 3-5 shows the measured output characteristics of the claw-pole PMSM under different load conditions. It can be seen that with the increase of motor load (or the phase current of the motor), the output torque constant k_T (the ratio of electromagnetic torque to armature current) is also increasing until reaching the rated operating point (n=1802 r/min, T_{out}=2.65Nm).

Table 3-5. Measured output characteristics of the claw-pole PMSM under different load conditions.

n (r/min)	I_a (A)	T_{out} (N·m)	P_{in} (W)	P_{out} (W)	η(%)	k_T (N·m /A)
2021	1.96	1.185	359.7	250.8	69.7	0.605
1959	2.34	1.500	417.5	307.7	73.7	0.640
1898	2.81	1.910	498.0	379.6	76.2	0.679
1828	3.49	2.463	595.5	471.5	79.2	0.706
1802	3.72	2.651	624.8	500.3	80.1	0.709
1776	4.27	3.000	700.9	557.9	79.6	0.702

Fig. 3-25 presents the output torque versus the speed of the claw pole PMSM. The orange curve in the figure shows the measured output torque of the motor, while the green curve demonstrates the calculated output torque via the proposed ECM with the predictable core loss. It is clear that the calculated torque is slightly smaller than the measured ones, and the maximum error between them does not exceed 6.5%. The error may come from the neglection of the stray loss and eddy current loss of PMs. In conclusion, the proposed ECM with the predictable core loss can accurately predict the core loss and the output torque of the PMSM in a wide speed range.

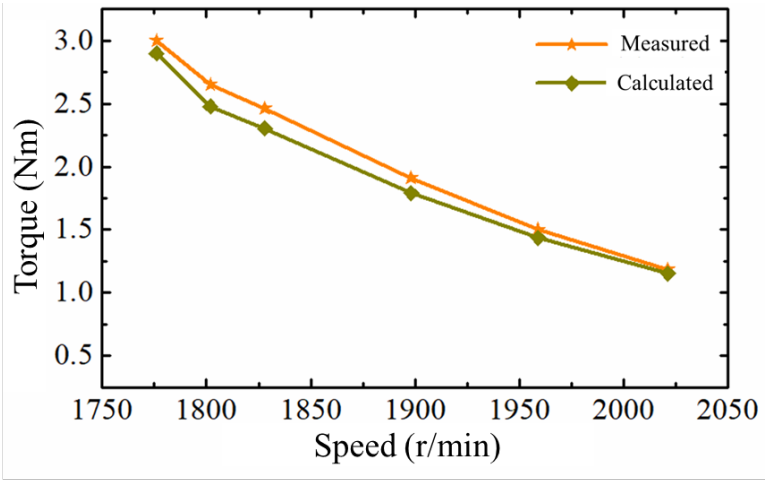

Fig. 3-25 Output torque versus the speed of the claw pole PMSM.

3.7 Core Loss Predictable Model in the Model Predictive Control of the PMSM

In the last decades, model predictive controls (MPCs) have become a hotspot of academic research and industrial application since they can provide superior dynamic and steady-state characteristics. Among various MPC methods, the deadbeat predictive current control (DPCC) has superior dynamic response capabilities, making it suitable for the high-speed drive [99-101]. However, the DPCC is a parameter-sensitive control method of the PMSM model, and hence parameter mismatch will cause the predicted control variables to deviate significantly from the expected values. Some parameter compensation methods have been developed to address this problem, but often they cannot provide satisfactory results.

In the DPCC, the ECM of PMSMs, also known as the predictive model, is the essence for the further behavior prediction of the control variables, such as the *q*-axis current. The predictive values of the control variables are derived though the ECM of the PMSM, and at the end of each control period, the difference between the predictive and actual values of control variables is forced towards zero. Thus, the DPCC is a model-dependent algorithm, and the inaccurate ECM will directly affect the values of the control variables and furtherly increase the errors. Therefore, improving the accuracy of the ECM of the PMSM can be very effective for the performance enhancement of the DPCC drive system.

3.7.1 Establishment of the *d*- and *q*-axis ECM with Predictable Core Loss

Although the per-phase ECM (as shown in Fig. 3-16) benefits in clear physical meaning and easy to understanding, the *d*-*q* axis ECM of PMSMs attracts more attention in the motor vector control area. Thus, a change of variables that formulates a transformation of the three-phase stationary circuit elements to the rotary reference frame can be written as

$$\boldsymbol{u}_{qd0} = \boldsymbol{K}_s \boldsymbol{u}_{abc} \tag{3.53}$$

where $\boldsymbol{u}_{qdo}$ is the voltage vector with the rotary reference frame, $\boldsymbol{u}_{abc}$ the voltage vector with the three-phase stationary reference frame, and the matrix $\boldsymbol{K}_s$ and its inverse matrix $(\boldsymbol{K}_s)^{-1}$ are defined as

$$\boldsymbol{K}_s = \frac{2}{3}\begin{pmatrix} \cos\theta & \cos(\theta - 2\pi/3) & \cos(\theta + 2\pi/3) \\ \sin\theta & \sin(\theta - 2\pi/3) & \sin(\theta + 2\pi/3) \\ 1/2 & 1/2 & 1/2 \end{pmatrix} \tag{3.54}$$

$$(\boldsymbol{K}_s)^{-1} = \begin{pmatrix} \cos\theta & \sin\theta & 1 \\ \cos(\theta - 2\pi/3) & \sin(\theta - 2\pi/3) & 1 \\ \cos(\theta + 2\pi/3) & \sin(\theta + 2\pi/3) & 1 \end{pmatrix} \tag{3.55}$$

Thus, (3.53) can be rewritten as

$$\begin{aligned} \boldsymbol{u}_{qd0} &= \boldsymbol{K}_s \boldsymbol{R}_s (\boldsymbol{K}_s)^{-1} \boldsymbol{i}_{qd0} + \boldsymbol{K}_s p\left[(\boldsymbol{K}_s)^{-1} \boldsymbol{\lambda}_{qd0}\right] \\ &= \boldsymbol{K}_s \boldsymbol{R}_s (\boldsymbol{K}_s)^{-1} \boldsymbol{i}_{qd0} + \boldsymbol{K}_s p(\boldsymbol{K}_s)^{-1} \boldsymbol{\lambda}_{qd0} + \boldsymbol{K}_s (\boldsymbol{K}_s)^{-1} p\boldsymbol{\lambda}_{qd0} \end{aligned} \tag{3.56}$$

where $\boldsymbol{\lambda}_{qdo}$ and $\boldsymbol{i}_{qdo}$ are the flux linkage and current vectors under the rotary reference frame, $\boldsymbol{R_s}$ is the stator winding resistance matrix, and p is the differential operator (=d/dt).

After mathematical manipulations, the voltage equations under d-q axis reference frame can be written as

$$\begin{cases} u_d = R_s i_d - \omega_e \lambda_q + p\lambda_d \\ u_q = R_s i_q + \omega_e \lambda_d + p\lambda_q \end{cases} \tag{3.57}$$

where ω_e is the PMSM speed in electrical radian per second.

Similarly, for the R_c branch in the per-phase ECM, the voltage equation can be described as

$$\boldsymbol{u}_{abc} = \boldsymbol{R_s} \boldsymbol{i}_{abc} + \boldsymbol{R_c} \boldsymbol{i}_{cabc} \tag{3.58}$$

Applying the reference frame transformation, one has

$$\begin{aligned} \boldsymbol{u}_{qd0} &= \boldsymbol{K}_s \boldsymbol{u}_{abc} = \boldsymbol{K}_s \boldsymbol{R}_s (\boldsymbol{K}_s)^{-1} \boldsymbol{i}_{qd0} + \boldsymbol{K}_s \boldsymbol{R}_c (\boldsymbol{K}_s)^{-1} \boldsymbol{i}_{cqd0} \\ &= \boldsymbol{R_s} \boldsymbol{i}_{qd0} + \boldsymbol{R_c} \boldsymbol{i}_{cqd0} \end{aligned} \tag{3.59}$$

where $\boldsymbol{i}_{abc}$ and $\boldsymbol{i}_{cabc}$ are the phase current and the core loss current matrixes under the three-phase stationary reference frame, whereas $\boldsymbol{i}_{cqdo}$ is the core loss current matrix under the rotary reference frame, and $\boldsymbol{R_c}$ is the equivalent core loss resistance matrix of the PMSM.

Then, the mathematical models of the PMSM considering the core loss resistance under the *d-q* axis reference frame have been established. Additionally, the *d-q* axis ECMs with predictable core loss are demonstrated as shown in Fig. 3-26.

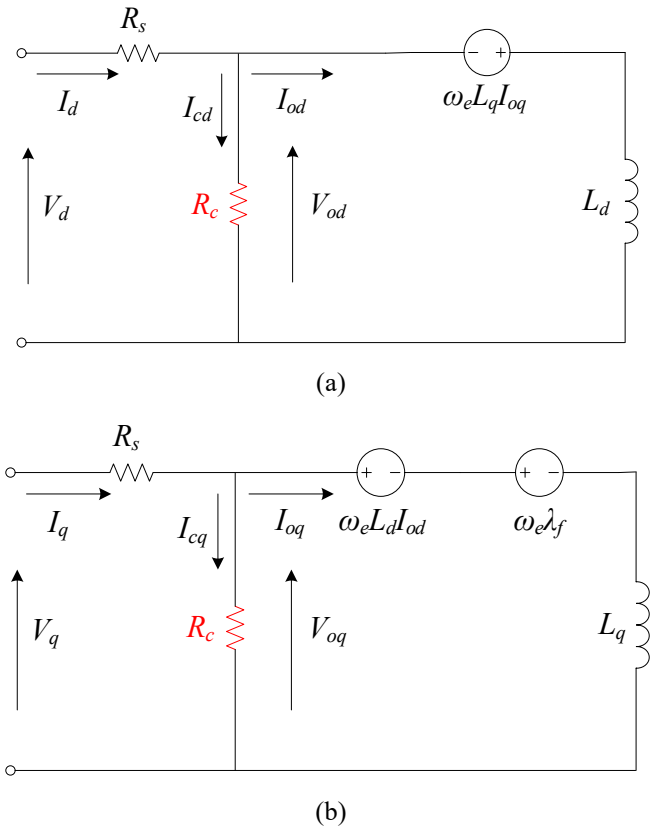

Fig. 3-26 ECM of PMSMs with predictable core loss: (a) *d*-axis; (b) *q*-axis.

3.7.2 Establishment of the Drive System with Improved DPCC

The DPCC is based on the predictive model of the PMSM to predict voltage references to generate proper switch signals via space vector pulse-width-modulation module for the inverter, and then drive the PMSM. Correspondingly, the model parameter mismatch of the DPCC is an obvious problem that has attracted widespread attention from scholars all over the world. Establishing an accurate predictive model of PMSMs can address the aforementioned problem fundamentally. The block diagram of the drive system with the improved DPCC is illustrated in Fig. 3-27. A PI controller which regulates the mechanical speed loop of the PMSM, and a DPCC which adjusts the *d-q* axis current loop are included in the proposed drive system. The reference *d-q* axis currents are derived from the speed error in the PI controller. In this application, the i_d=0 control strategy is adopted to realize the maximum torque per ampere drive.

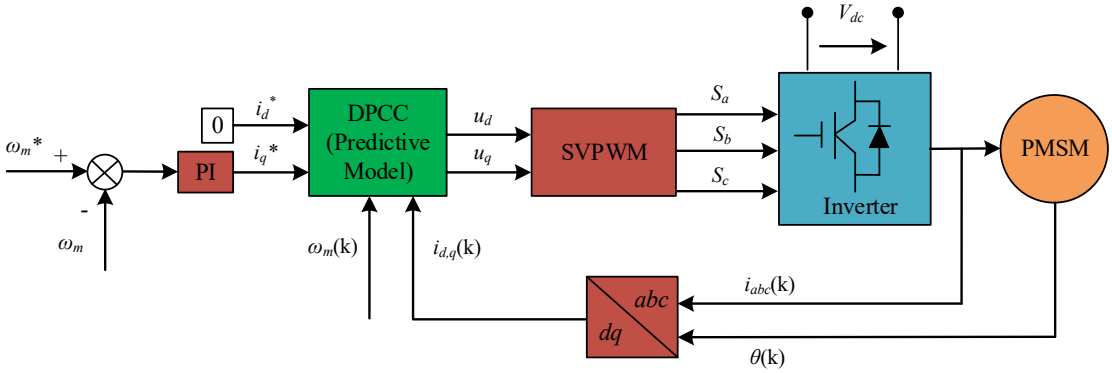

Fig. 3-27 Schematic diagram of the DPCC drive system.

The current equations considering the core loss of the PMSM in the DPCC can be written as

$$\begin{bmatrix} \frac{di_{od}}{dt} \\ \frac{di_{oq}}{dt} \end{bmatrix} = \begin{bmatrix} -\frac{R_c R_s}{L_s\left(R_c+R_s\right)} & \omega_e \\ -\omega_e & -\frac{R_c R_s}{L_s\left(R_c+R_s\right)} \end{bmatrix} \begin{bmatrix} i_{od} \\ i_{oq} \end{bmatrix} + \begin{bmatrix} \frac{R_c}{L_s\left(R_c+R_s\right)} & 0 \\ 0 & \frac{R_c}{L_s\left(R_c+R_s\right)} \end{bmatrix} \begin{bmatrix} u_d \\ u_q \end{bmatrix} + \begin{bmatrix} 0 \\ -\frac{\omega_e \lambda_f}{L_s} \end{bmatrix} \tag{3.60}$$

$$\begin{cases} i_d = i_{od} - \dfrac{L_s \omega_e}{R_c} i_{oq} \\ i_q = i_{oq} + \dfrac{L_s \omega_e}{R_c} i_{od} + \dfrac{\omega_e \lambda_f}{R_c} \end{cases} \tag{3.61}$$

where i_d and i_{od} are the d-axis current and magnetizing current, and i_q and i_{oq} are the q-axis current and magnetizing current, respectively. λ_f is flux linkage generated by the PMs.

Assuming that the control system has very small sampling period T_s, the PMSM's discrete current predictive model can be obtained according to the first-order Taylor series as

$$\boldsymbol{i}(k+1) = \boldsymbol{A}\boldsymbol{i}(k) + \boldsymbol{C}\boldsymbol{u}(k) + \boldsymbol{D}(k) \tag{3.62}$$

where

$$\boldsymbol{i}(k)=\begin{bmatrix} i_d(k) \\ i_q(k) \end{bmatrix}, \boldsymbol{u}(k)=\begin{bmatrix} u_d(k) \\ u_q(k) \end{bmatrix} \tag{3.63}$$

$$\boldsymbol{A}=\begin{bmatrix} 1-\dfrac{T_s R_c R_s}{L_s(R_c+R_s)} & T_s\omega_e(k) \\ -T_s\omega_e(k) & 1-\dfrac{T_s R_c R_s}{L_s(R_c+R_s)} \end{bmatrix} \tag{3.64}$$

$$\boldsymbol{C}=\begin{bmatrix} \dfrac{T_s R_c}{L_s(R_c+R_s)} & 0 \\ 0 & \dfrac{T_s R_c}{L_s(R_c+R_s)} \end{bmatrix} \tag{3.65}$$

$$\boldsymbol{D}(k)=\begin{bmatrix} 0 \\ -\dfrac{T_s\omega_e(k)\lambda_f}{L_s} \end{bmatrix} \tag{3.66}$$

The PMSM voltage in the following modulation period is predicted as

$$\boldsymbol{u}(k+1)=\boldsymbol{C}^{-1}\left[\boldsymbol{i}^*(k)-\boldsymbol{A}\left(\boldsymbol{A}\boldsymbol{i}(k)+\boldsymbol{C}\boldsymbol{u}(k)+\boldsymbol{D}(k)\right)-\boldsymbol{D}(k+1)\right] \tag{3.67}$$

where $\boldsymbol{i}^*(k)$ is the reference currents.

3.7.3 Comparison of the Proposed and Traditional DPCC

Initially, the motor is at standstill and with no-load. A step command of rated speed (1800 r/min) from standstill is provided. In the drive system, the parameters of the PI controller are fixed as K_p=10 and K_i=0.24 both for the traditional DPCC and the improved DPCC. Fig. 3-28 depicts the rotor speed response of the two cases. It is found that the rise time with the traditional DPCC is 0.091 s, and after a short period of oscillation, the motor speed can follow the preset speed without steady-state error, as shown by the blue line. The red line describes the rotor speed response with the improved DPCC, and the rise time is 0.085 s and also can follow the preset speed without steady-state error. The dynamic speed response of the drive system with the improved DPCC is faster than that of the traditional one.

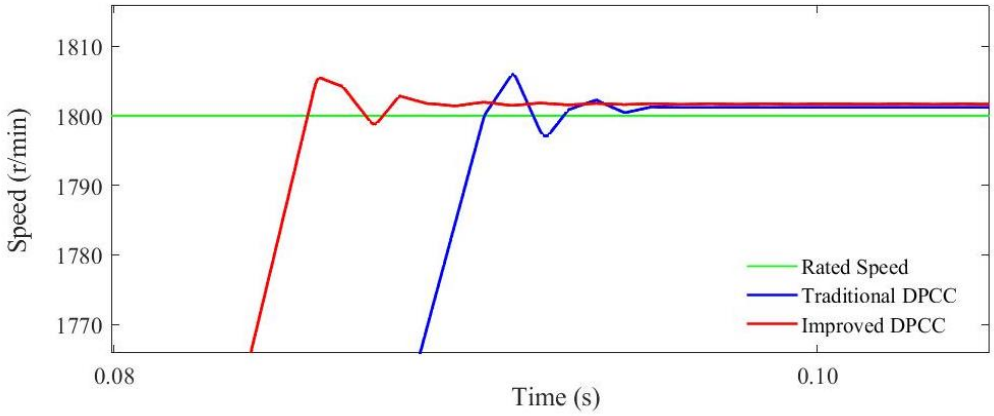

Fig. 3-28 Comparison of rotor speed response between the drive systems with the traditional and improved DPCCs.

After the rotor speed reaches the steady-state, a torque step command of 1 Nm from no-load at 0.12 s is applied. The corresponding torque characteristics for both the traditional and improved DPCCs are presented in Fig.3-29. With the traditional DPCC, after a short period of oscillation, the speed offset of the drive system changes from zero to a negative value, i.e., the steady-state speed is less than the preset speed (1800 r/min), depicted by the blue line. With the improved DPCC, the rotor speed enters the steady-state after 0.005 s of oscillation, and can still follow the preset speed accurately. It can also be seen that the torque robustness of the drive system with the improved DPCC is better than the traditional DPCC when the motor load torque changes suddenly.

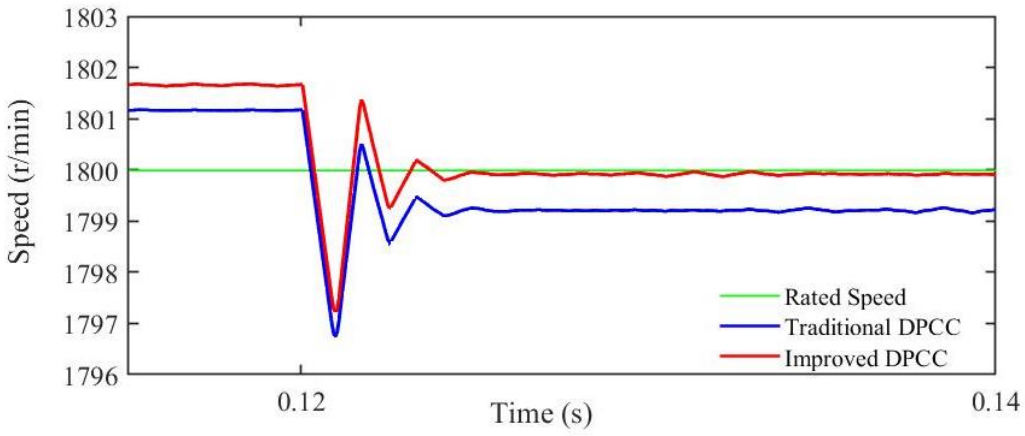

Fig. 3-29 Comparison of torque response between the drive systems with the traditional and improved DPCCs.

Fig. 3-30 illustrates the phase current response of the drive system with the improved DPCC during the control process mentioned above. After the phase currents are stabilized, their amplitude is 2.379 A, and the phase currents are quite sinusoidal.

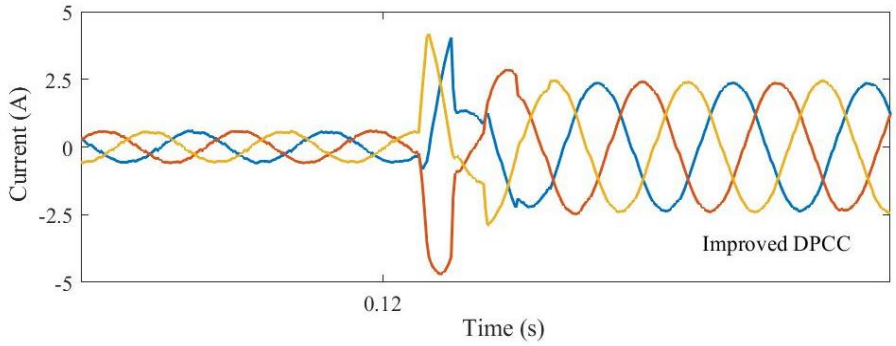

Fig. 3-30 Phase current response of the drive system with the improved DPCC.

3.8 Conclusion

Firstly, this chapter analyzes the 3-D rotating magnetic fields in a claw pole PMSM which has a stereoscopic magnetic structure, and the magnetic flux density trajectory at any point in the stator of the motor is of 3-D pattern and gets into two categories: the alternating pattern and near the elliptical rotating pattern. Moreover, these 3-D magnetic flux density trajectories contain a large number of high-order harmonics, and the higher the proportion of the high-order harmonics, the more distortion of the trajectory. However, the 3-D trajectory of the magnetic flux density at any point in the stator is the vector summation of the trajectories of magnetic flux density's fundamental and high-order harmonics, and the trajectories of the fundamental and high-order harmonics of the magnetic flux density just fall into two categories: 1-D alternating pattern like a straight line and 2-D rotating pattern like an ellipse.

Secondly, the core loss mathematical models with the 3-D rotating magnetic fields are derived, and then the method of modelling the core loss in the ECM is developed systematically. In the next sections, the motor parameters including the equivalent core loss resistance are determined based on finite element method and considering the 3-D rotating magnetic field, which is efficient and accurate, particularly at the design stage. More importantly, the equivalent core loss resistance in the proposed ECM is modelled as a function of the motor speed, and hence the prediction accuracy of entire speed range

has been boosted. Both no-load and load tests verify that the proposed ECM and parameters identification methods are practical, effective and accurate.

Finally, this chapter establishes an improved DPCC with a novel predictive model to enhance the performance of the PMSM drive system. In the improved DPCC, the predictive model of PMSMs with predictable core loss is adopted to generate more accurate predictive control variables. Then, the dynamic speed response and the torque robustness of the drive system with this improved DPCC are enhanced effectively. At the same time, the phase currents of the drive system with the improved DPCC can maintain a good sinusoid. This predictive model can be further extended to analyze the robustness when other kinds of disturbance, such as parameter variation during operation, and this approach would also be effective to enhance the accuracy of the predictive control variables in other kinds of model predictive control.

CHAPTER 4. PER-PHASE EQUIVALENT CIRCUIT MODEL OF THE PMSM WITH PREDICTABLE CORE LOSS

4.1 Introduction

ECM with predictable core loss has not been limited to a standard topology, since the mechanism of the core loss has not been fully understood yet, hence its modelling in the ECM is also a pending issue. Some topologies have been developed over the last decades to achieve specific features, and the most widely used per-phase ECM of the PMSM is as shown in Fig. 4-1.

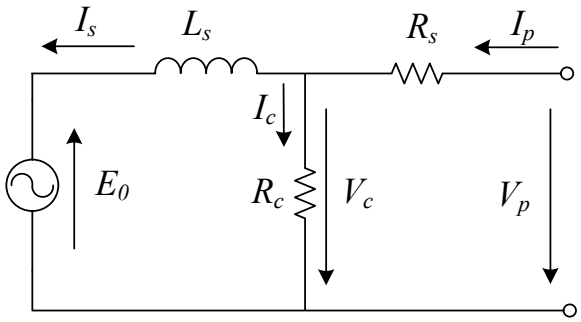

Fig. 4-1. Per-phase ECM of PMSM with predictable core loss.

In Fig. 4-1, the equivalent core loss resistance R_c is connected in parallel with the series branch of synchronous inductance L_s and back EMF E_0. If the PMSM is operated with the optimal brushless dc control, i.e., adjusting the armature current I_s and the back *emf* to have the same phase angle, and the terminal voltage of per-phase V_p is controlled to vary against the back *emf* (or speed) and load current by

$$V_p = E_0 + \mathrm{j}X_s I_s + R_s\left(I_s + \frac{E_0 + \mathrm{j}X_s I_s}{R_c}\right) \tag{4.1}$$

where R_s is the phase winding resistance, $X_s=\omega_e L_s$ the synchronous reactance, and ω_e is the rotor speed in electrical angular frequency.

The core loss is calculated by

$$P_c = 3\frac{V_c^2}{R_c} = 3\frac{E_0^2 + (X_s I_s)^2}{R_c} \tag{4.2}$$

To further understand the core loss and the magnetic flux in stator core which arises the core loss, Fig. 4-2 illustrates the magnetic flux density versus the phase current in the stator core of the PMSM. When the PMSM operates under the no-load conditions where no current flows in the armature windings, I_p=0, the magnetic flux density in the stator core generated by PMs is at the inflection point of the magnetization curve, B_{PM}, which is close to the saturation value B_S. When the PMSM operates under the load conditions where there are armature currents fed into the motor, the magnetic flux density in the stator core is the resultant flux density generated by both PMs and phases currents, and it increases slowly with the significant grow of the phase current. When the phase current reaches the rated value I_N, the stator core flux density B_N is very close to the saturation value B_S., and will not increase significantly, and that is the magnetic saturation effect. On the other hand, the core loss of the PMSM positively correlates the magnetic flux density. Similar to the relationship of magnetic flux density and the phase current, the core loss will not increase evidently with the growing phase current.

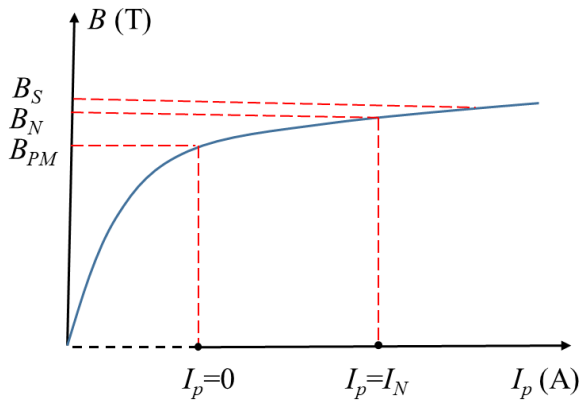

Fig. 4-2. Magnetic flux density versus the phase current in the stator core of the PMSM.

Therefore, (4.2) may much overestimate the extra core loss caused by the armature current. The core loss does go up when the load or armature current increases, but it will not increase that much due to magnetic saturation effect. For example, if the voltage generated by the armature current, X_sI_s, has the same value of E_0, the calculated core loss would be doubled compared with that at no-load conditions where X_sI_s equals zero.

In conclusion, the ECM as shown in Fig. 4-1 cannot provide accurate core loss predictions, especially when the motor is operating with large loads or armature currents.

4.2 Per-phase ECM of the PMSM with Predictable Core Loss

The proposed generalized per-phase ECM of the PMSM with predictable core loss is shown in Fig. 4-3. When the PMSM operates at no-load condition, i.e., the armature terminals are open-circuited and hence no current flows in the armature windings, the magnetic flux in the motor is generated by the PMs only. The PM magnetic flux not only contributes the back electromotive force but also causes the core loss; therefore, the equivalent resistance which stands for the no-load core loss should be connected in parallel with the back electromotive force E_0. Since there are three components of the core loss, three equivalent resistances R_h, R_e and R_{an} are adopted to respectively present the hysteresis loss, eddy current loss and anomalous loss at no-load conditions. Various stator core materials have different proportions and development trends of these three core loss components. The advantage of using three resistances rather than single resistance as in the traditional topology is that it makes the core loss evaluation, optimization and even control more flexible and targetable.

When the PMSM operates at loading conditions, i.e., the load current flows in the armature windings, the magnetic flux in the motor is the resultant flux of the PMs-generated flux and the load current-generated flux. Moreover, the magnetic flux in the motor cannot increase linearly with the load current due to the magnetic saturation effect of the stator core. To depict the extra core loss due to the load current and take the magnetic saturation effect into consideration, an equivalent resistance R_i connected in parallel with the synchronous inductance L_s is adopted. The summation of the power loss in R_i, R_h, R_e and R_{an} represents the core loss when the PMSM operates at loading conditions.

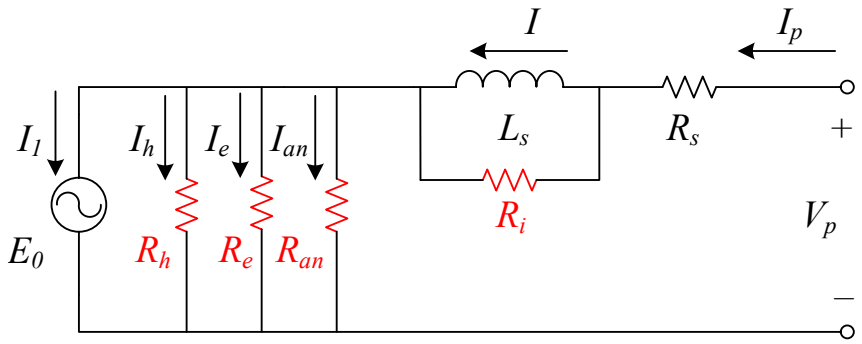

Fig. 4-3. Generalized per-phase ECM of PMSM considering the core loss and magnetic saturation effect (In motor convention).

According to the proposed ECM, the mathematical models of the PMSM should be rewritten as

$$V_p = E_0 + R_s I_p + \frac{\mathrm{j}X_s R_i}{\mathrm{j}X_s + R_i} I_p = E_0 + R_s I_p + \frac{X_s^2 R_i}{X_s^2 + R_i^2} I_p + \frac{\mathrm{j}X_s R_i^2}{X_s^2 + R_i^2} I_p \tag{4.3}$$

$$I_p = I_1 + I_h + I_e + I_{an} \tag{4.4}$$

where V_p and I_p are respectively the phase voltage and phase current. E_0 is the back electromotive force, R_s the phase winding resistance, $X_s=\omega_e L_s$ the synchronous reactance, and R_i, R_h, R_e and R_{an} are equivalent core loss resistances. I_h, I_e, I_{an}, and I_1 are currents flowing through R_h, R_e, R_{an}, and E_0, respectively.

The electromagnetic power and torque of the PMSM can be calculated as:

$$P_{em} = n_p E_0 I_1 \cos\psi \tag{4.5}$$

$$T_{em} = \frac{P_{em}}{\omega_m} \tag{4.6}$$

where ψ stands for the angle between phasors E_a and I_1, n_p the number of phases, and ω_m is the rotor speed in mechanical angular frequency.

Moreover, the copper loss P_{cu}, the no-load core loss P_{co}, the load core loss P_{ci}, the input power P_{in}, the output power P_{out}, and the efficiency η of the PMSM are obtained as follows:

$$P_{cu} = n_p I_p^2 R_s \tag{4.7}$$

$$P_{co} = P_h + P_e + P_{an} = n_p \frac{E_0^2}{R_h} + n_p \frac{E_0^2}{R_e} + n_p \frac{E_0^2}{R_{an}} \tag{4.8}$$

$$P_{ci} = P_{co} + P_i = P_h + P_e + P_{an} + P_i = n_p \frac{E_0^2}{R_h} + n_p \frac{E_0^2}{R_e} + n_p \frac{E_0^2}{R_{an}} + n_p I_p^2 \frac{X_s^2 R_i}{X_s^2 + R_i^2} \tag{4.9}$$

$$P_{in} = n_p V_p I_p \cos\varphi \tag{4.10}$$

$$P_{out} = P_{em} - P_{mech} \tag{4.11}$$

$$\eta = P_{out} / P_{in} \times 100\% \tag{4.12}$$

where φ is the angle between phasors V_p and I_p, n_p the number of phases, and P_{mech} is the mechanical loss of the PMSM.

4.3 Determination of the Equivalent Core Loss Resistances

Identification of the parameters in the proposed ECM properly is the key to achieving precise analysis results. Generally, there are two methods to work out these parameters including the equivalent core loss resistances, i.e., the finite element method (FEM) and the experimental test. Three-dimensional core loss calculation considering the rotating magnetic field is highly recommended due to its superior accurateness, and details can be found in [20]. Although experimental tests are able to provide intuitional and reliable solutions, additional auxiliary equipment is needed to separate the core loss and the mechanical loss. For instance, an identical rotor with non-magnetized PMs, or an equivalent stator made of non-ferromagnetic material.

In this chapter, a three-phase PM transverse flux synchronous motor (TFSM) with the SMC core is selected as the prototype motor to verify the proposed ECM, and other types of PM synchronous motor, e.g., surface-mounted PMSM, interior PMSM, claw-pole PMSM, axial flux PMSM, also can be described by this proposed ECM. Furthermore, both the single-phase and multi-phase PMSMs can be represented by this proposed ECM. The parameters of the PM TFSM are listed in Table 4-1, and the prototype motor is

illustrated in Fig. 4-4. The outer rotor configuration is introduced in this PM TFSM, and the permanent magnets are mounted on the inner surface of the rotor. The stator has three stacks of core which are arranged axially, and three concentrated coils are embedded in the stator for three phases.

Table 4-1. Parameters of the PM TFSM.

Parameter	Value
Number of phases	3
Number of poles	20
Rated power	640 W
Rated speed	1800 r/min
Rated torque	3.4 Nm
Rated phase current	5.5 A
Winding resistance	0.41 Ω
Synchronous inductance	6.08 mH
PM flux	0.28 mWb
Number of turns of a phase winding	125

(a) (b)

Fig. 4-4. Prototype of the PM TFSM: (a) Rotor, (b) Stator.

For determining the equivalent core loss resistance, R_h, R_e and R_{an}, the no-load core loss data should be figured out. In this study, all parameters in the ECM are from experimental tests, and Table 4-2 lists the measured no-load core loss with different speed or frequency [60, 102]. The core loss measurement of the PM motor is a complex process and requires additional auxiliary components, such as a dummy rotor or stator, to imitate and measure the mechanical loss of the motor. In this study, the rotor of the PM motor is replaced by a wood one to imitate the windage, and hence measure the mechanical loss of the PM motor without the coupled core loss. The PM motor is driven to act as a generator and a DC motor is selected as the prime mover, and the armature terminals of the PM motor are open-circuited and hence no current flows in the armature windings, i.e., no copper loss.

The electromagnetic properties of the selected DC motor have been well measured in advance. Therefore, the power fed into the DC motor when it drives the PM motor subtracting the power fed into the DC motor when it operates alone yields the total of the core loss and mechanical loss of the PM motor. Then, the total of the core loss and mechanical loss subtracting the mechanical loss of the PM motor, which is measured with the help of the dummy rotor, obtains the core loss of the PM motor.

Table 4-2. Measured no-load core loss of the PM TFSM.

Speed (rpm)	Core Loss (W)
200	4.2
400	9.3
600	15.3
800	22.1
1000	29.8
1200	38.4
1400	47.9
1600	58.2
1800	69.4

Notice that the flux density frequency in the stator of the PMSM is proportional to the speed of the PMSM, and then the no-load core loss of the PM TFSM is obtained as

$$P_c = n_p E_0^2 \left(\frac{1}{R_h} + \frac{1}{R_e} + \frac{1}{R_{an}}\right) = k_h n + k_e n^2 + k_{an} n^{1.5} \tag{4.13}$$

where n is the speed of the PMSM, n_p=3 for this PM TFSM.

By curve-fitting the data in Table 4-2, the core loss coefficients can be obtained as k_h=1.881×10^{-2} W/rpm, k_e=1.085×10^{-5} W/(rpm)^2, and k_{an}=5.178×10^{-6}. As E_0=4.44$fN\Phi_m$ and f=pn/120, where p=20 is the number of poles, E_0=0.0259n. It can be deduced that R_h is a linear function of motor speed n, R_{an} is proportional to the square root of n, and R_e is a constant. Then we can obtain R_h =0.107n Ω, R_e =185.5 Ω, and R_{an} =388.7$\sqrt{n}$ Ω.

For determining R_i, the motor core loss under various load currents should be figured out. It should be noted that the motor control method will affect the magnetic field distribution and hence the core loss. Here, the PM TFSM is driven by the so-called optimal brushless

dc control, i.e., the armature current is controlled to be in phase with the back *emf*, so I_p lags Φ_m by 90 degrees.

Actually, the synchronous reactance is a function of the motor speed as well

$$X_s = \frac{\pi p L_s}{60} n \tag{4.14}$$

where p is the number of poles, and n is the motor speed in rpm.

Substituting (4.14) into (4.9) and solving it, R_i can be obtained as

$$R_i = \frac{S_2^2 n^2 + S_2 n\sqrt{S_2^2 n^2 - 4S_1^2}}{2S_1} \tag{4.15}$$

$$S_1 = \frac{P_{ci} - P_{co}}{n_p I_p^2} \tag{4.16}$$

$$S_2 = \frac{\pi p L_s}{60} \tag{4.17}$$

The core loss of the PM TFSM at the rated speed 1800 rpm and rated load current 5.5 A is 120.3 W, and from the above-mentioned equations, S_1=0.56 and S_2=6.37 $\times$ 10^{-3}. Therefore, the equivalent resistance R_i for the PM TFSM is computed as

$$R_i = \frac{(6.37\times10^{-3})^2 n^2 + (6.37\times10^{-3}) n\sqrt{(6.37\times10^{-3})^2 n^2 - 1.2544}}{1.12} \tag{4.18}$$

4.4 Performance Comparisons of ECMs with Predictable Core Loss

There are two vital points that determine the accuracy of the ECMs with predictable core loss. The first is where the equivalent core loss resistance should be placed, and the second is how to identify the value of the equivalent core loss resistance. Through a comprehensive and in-depth analysis of the previous literature [103], two representative methods will be used to compare with the proposed method in this chapter.

Method 1: the topology of the ECM is as shown in Fig. 4-1, and the equivalent core loss resistance R_c is a single-valued resistance and determined based on the core loss at rated speed and no-load condition. For the PM TFSM, R_c=94 Ω.

Method 2: the topology of the ECM is as shown in Fig. 4-1, and the equivalent core loss resistance R_c is a function of the motor speed and determined based on the no-load core loss at various speeds. For the PM TFSM, R_c=0.0583n Ω, where n is the motor speed.

The experimental platform of the PM TFSM is illustrated in Fig. 4-5. It mainly contains a DC motor, a torque transducer, and the PM TFSM with SMC core. These two motors are connected via a torque transducer, and both of them can operate as the driver or load, depending on performance testing requirements. The torque transducer was made in Switzerland, and the type is Vibrometer TM109 S/N 0148, and the range is 20 Nm. The torque transducer has been calibrated before the test to guarantee the accuracy of the measurement. More conveniently, the neutral point of the three phase windings is led to outside for measurement.

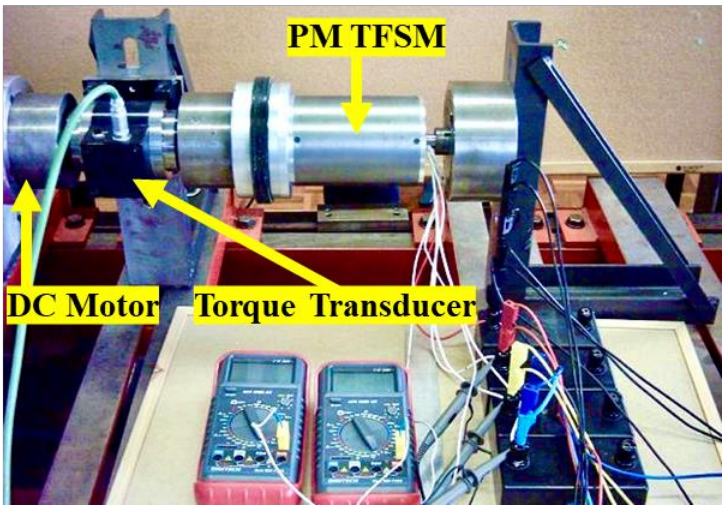

Fig. 4-5. Experimental platform of the PM TFSM with SMC core.

Fig. 4-6 demonstrates the predicted no-load core loss via method 1, method 2, the proposed method, and measured core loss. It can be seen that the proposed method can predict the no-load core loss with the highest precision, followed by method 2, while method 1 has the lowest precision.

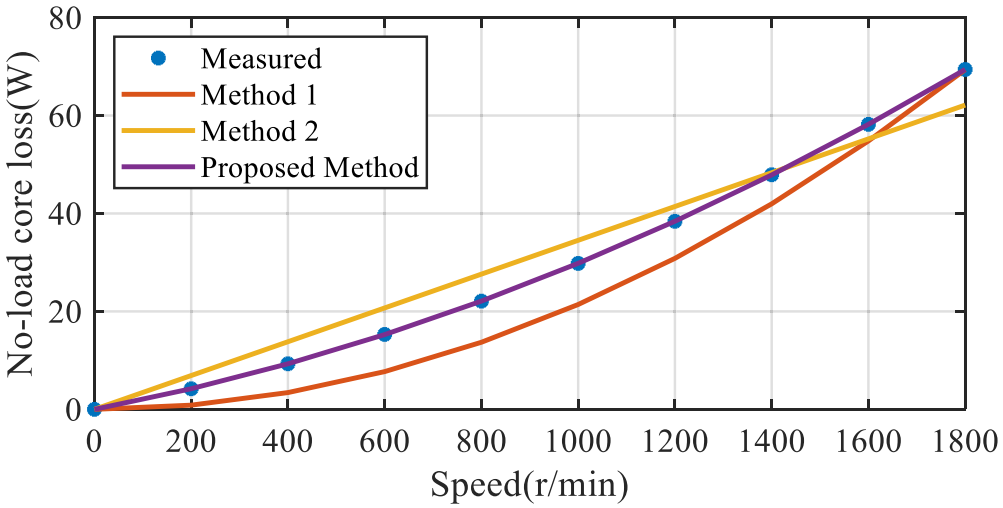

Fig. 4-6. No-load core loss versus motor speed predicted by different methods.

The errors between the measured no-load core loss and predicted values are evaluated via the standard deviation, and that is calculated as

$$\sigma = \sqrt{\frac{1}{N}\sum_{i=1}^{N}(x_i - \bar{x})^2} \tag{4.19}$$

The standard deviation of method 1 is about 6.22, and that of method 2 is 4.88, while that of the proposed method is close to zero. Quantitative analysis confirms that the proposed ECM and parameter identification method have superior performance in core loss prediction.

Another distinctive merit of the proposed ECM is that it makes the analysis of each component of core loss possible, and the hysteresis loss, eddy current loss, and anomalous loss versus motor speed are depicted in Fig. 4-7. In the motor speed range of 0 to 1750 r/min, the hysteresis loss dominates the core loss, while the eddy current loss will master the core loss in the higher speed range, and the anomalous loss, which is less than 1 W even at the rated speed of 1800 r/min, maintains the lowest value.

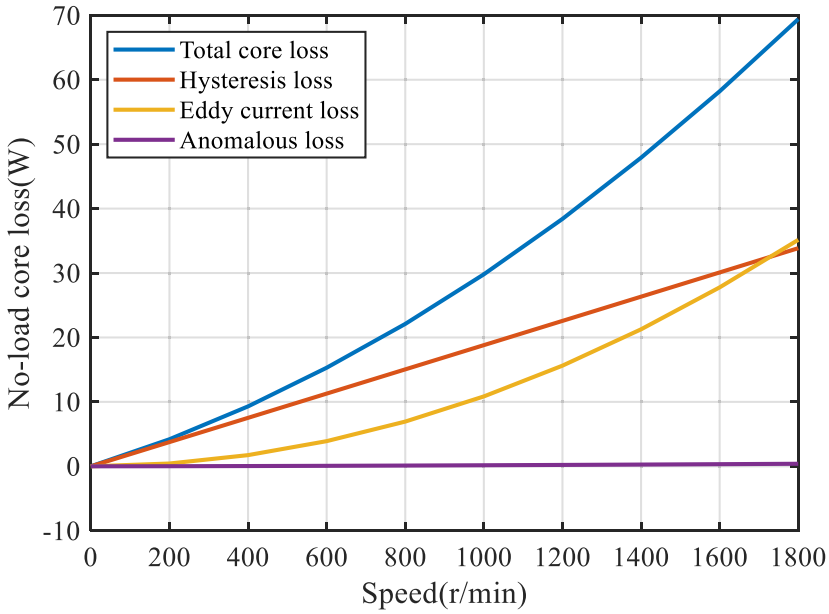

Fig. 4-7. No-load core loss and its components versus motor speed.

Furthermore, the proposed ECM has significant advantages in predicting the core loss and performance under loading conditions. Fig. 4-8 presents the core loss at the rated operating point predicted by different methods, at which the phase current is 5.5 A and the motor speed is 1800 r/min. Due to the ignoring of the magnetic saturation effect, methods 1 and 2 notably overestimate the core loss, but the proposed method can estimate it accurately.

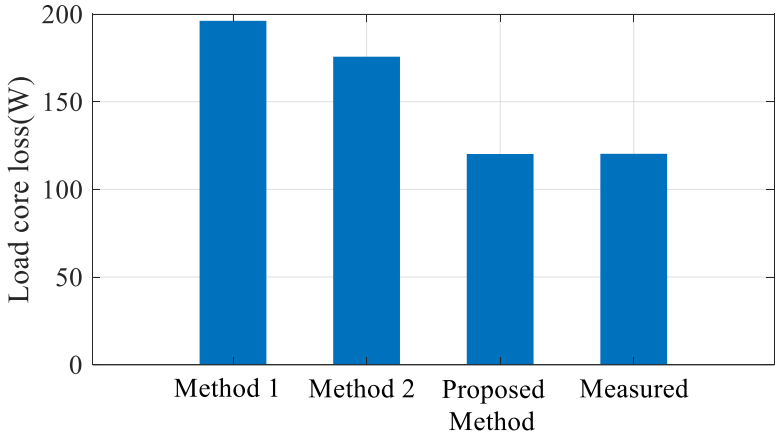

Fig. 4-8. Core loss at the rated operating point predicted by different methods.

An excellent ECM with predictable core loss of the PMSM is not only able to predict the core loss correctly, but also can predict the output performance of the motor reliably.

Since the measurement of the load core loss is very difficult and hard to ensure accuracy, and we need to separate the output power, copper loss and mechanical loss from the input power, we compare the mechanical characteristics and efficiency of the motor which includes the calculation and comparison of the load core loss in following paragraphs.

When the PM TFSM operates under the optimal brushless dc control with a dc link voltage, i.e., adjusting the current I_1 and back *emf* E_0 to have the same phase angle, the phase voltage of the motor can be obtained as

$$V_p = \sqrt{(E_0 + R_s I_p + \frac{I_p X_s^2 R_i}{X_s^2 + R_i^2})^2 + (\frac{I_p X_s R_i^2}{X_s^2 + R_i^2})^2} \tag{4.20}$$

Therefore, the mechanical characteristic of the PM TFSM, i.e., the relation of the motor speed and output torque can be worked out from the above-mentioned equation as

$$\begin{aligned} V_p^2 = & \left[\begin{array}{l} k_{emf} n + R_s (\frac{T_{em}}{k_T} + \frac{k_{emf}}{k_h} + \frac{k_{emf} n}{k_e} + \frac{k_{emf} \sqrt{n}}{k_{an}}) \\ + \frac{k_{Xs}^2 n^2 R_i}{k_{Xs}^2 n^2 + R_i^2} (\frac{T_{em}}{k_T} + \frac{k_{emf}}{k_h} + \frac{k_{emf} n}{k_e} + \frac{k_{emf} \sqrt{n}}{k_{an}}) \end{array} \right]^2 \\ & + \left[\frac{k_{Xs} n R_i^2}{k_{Xs}^2 n^2 + R_i^2} (\frac{T_{em}}{k_T} + \frac{k_{emf}}{k_h} + \frac{k_{emf} n}{k_e} + \frac{k_{emf} \sqrt{n}}{k_{an}}) \right]^2 \end{aligned} \tag{4.21}$$

where k_{emf}=0.0259 V/rpm is the back *emf* constant, k_{Xs}=2πpL_s/120=0.00637 Ω/rpm is the synchronous reactance constant, and k_T=90k_{emf}/π=0.742 Nm/A is the electromagnetic torque constant.

In methods 1 and 2, the phase voltage equation can be obtained by rewriting (4.1) as

$$V_p = \sqrt{(E_0 + R_s I_s + \frac{E_0 R_s}{R_c})^2 + (X_s I_s + \frac{X_s I_s R_s}{R_c})^2} \tag{4.22}$$

The mechanical characteristic of the PM TFSM can be calculated as

$$V_p^2 = \left[k_{emf} n + R_s \frac{T_{em}}{k_T} + \frac{k_{emf} R_s n}{R_c} \right]^2 + \left[k_{Xs} n \frac{T_{em}}{k_T} (1 + \frac{R_s}{R_c}) \right]^2 \tag{4.23}$$

To furtherly demonstrate the superiority of the ECM considering the core loss, the ECM ignoring the core loss is also be compared, and hence the voltage equation becomes

$$V_p = E_0 + R_s I_p + \mathrm{j} X_s I_p \tag{4.24}$$

where the currents passing through E_0, R_s and X_s are the same. As I_p is controlled to be in phase with E_0, one can obtain

$$V_p^2 = (k_{emf} n + R_s \frac{T_{em}}{k_T})^2 + (k_{Xs} n \frac{T_{em}}{k_T})^2 \tag{4.25}$$

For V_{dc}=192 V, the curves of the mechanical characteristic in terms of the motor speed against output torque are solved by different methods as shown in Fig. 4-9. It is noted from the prototype experiment that the ratio of V_p over V_{dc} is not fixed, but decreases by a slope of approximately 10% against the increase of torque. In order to have a fair comparison with the measured data, this variation is included in the prediction of the mechanical characteristics.

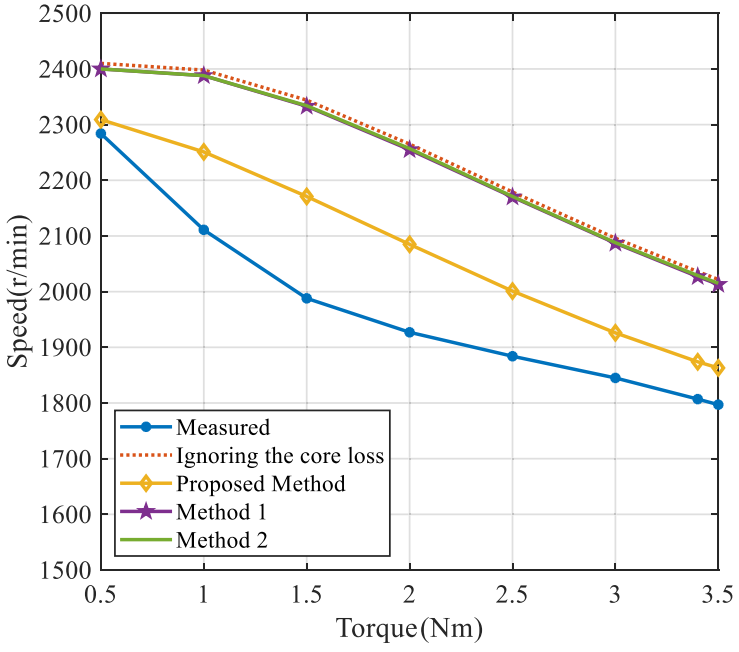

Fig. 4-9. Core loss at the rated operating point predicted by different methods.

It is seen from the figure that the prediction of ignoring the core loss is far from the measurement, while method 1 and method 2 can improve the predicted results slightly. Compared with these counterparts, the proposed method has the best performance in predicting the mechanical characteristic of the PMSM. This comparison results indirectly verify the superiority of the proposed method in predicting the load core loss of the motor.

To quantitatively compare the four cases, their errors are calculated. It is seen that the predicted speeds when ignoring the core loss have an average error of 13.6% compared to the measurements, while the average errors marginally decrease to 13.13% and 13.19% in method 1 and method 2 respectively, and it decreases considerably to 5.4% in the proposed method.

The most notable advantage of the ECM, compared to the finite element method, can provide various analysis results with much less calculation burden. An example of applying the proposed ECM to analyse the motor efficiency is constructed, as shown in Fig. 4-10. In the optimal brushless dc control mode, the maximum efficiency of the PM TFSM is 80%, which is consistent with the prototype measurement.

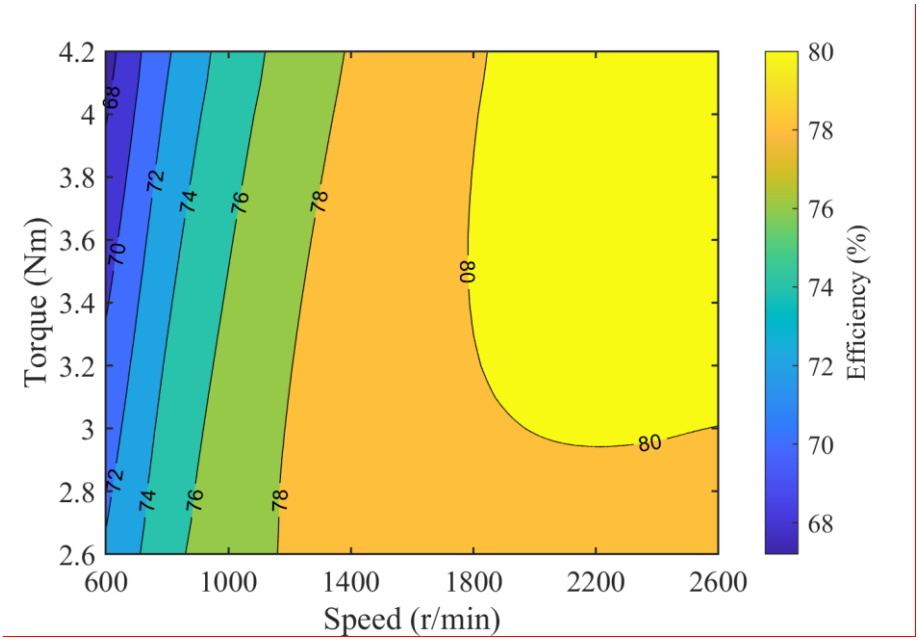

Fig. 4-10. Efficiency map of the PM TFSM.

4.5 Conclusion

This chapter presented a generalized per-phase equivalent circuit model considering the core loss and magnetic saturation effect, for predicting the core loss and analysing the performance of PMSMs under varying speed and load conditions. The proposed model has been applied to calculate the performance of a PM transverse flux synchronous motor under the optimal brushless dc control mode. Compared with previous studies of the ECMs with predictable core loss, the proposed method has better accuracy in both no-load and load core loss predictions, and can analyse the hysteresis loss, eddy current loss, and anomalous loss separately. Furthermore, in predicting the motor performance, such as mechanical characteristics, the proposed method can provide more reliable results compared to the traditional ECM ignoring the core loss as well as previous ECMs considering core loss. The superior performances of the proposed method have been verified by experiments.

The proposed model of the PMSM can be versatilely used in motor design, optimization, and control with fast calculation speed. For example, the developed model is also be useful for improving the performance of the PMSM under other motor control strategies such as model predictive control, in which the mathematical model will be more accurate by considering the core loss under varying speed and load conditions.

Finally, a brief discussion about whether or not the eddy current loss of PMs should be included in the ECM is launched. The ECM of the synchronous motor is different from that of the asynchronous motor. To be more specific, in the ECM of the asynchronous motor, the electromagnetic parameters of the rotor, such as the rotor winding resistance, are included. By contrast, in the ECM of the synchronous motor, the electromagnetic parameters of the rotor are eliminated since its stator and rotor magnetic fluxes are rotating at the same speed. Generally, eddy current loss in PMs is caused by the harmonic fluxes, and it might not be significant when the motor operates stably at the synchronous speed.

CHAPTER 5. DQ AXIS EQUIVALENT CIRCUIT MODELS OF THE PMSM WITH PREDICTABLE CORE LOSS

5.1 Introduction

Electric vehicles (EVs) have been considered as one of the major solutions for tackling greenhouse gas emission and environment pollution problem. Electric motor drives are among the key enabling technologies for EV success [5, 6]. Various types of electric motors have been investigated for driving the EVs, such as induction motors [104, 105], switched reluctance and synchronous reluctance motors [106-109] and permanent magnet (PM) synchronous motors (PMSMs) [110-124]. Particularly, the PMSMs have been very widely researched and applied thanks to their many advantages such as high efficiency, high power density, light weight and small size. While the surface-mounted PMSM (SPMSM) has merit of easy assembly of permanent magnets [110-112], the interior PMSM (IPMSM) [113-118] possesses the advantages of high resistance against demagnetization and possible usage of flux concentration, leading to higher torque density and higher speed range.

In [113], the interior PMSM with distributed winding design revealed the capability of simultaneously achieving flux concentration and reluctance torque, and avoiding PM demagnetization based on the rotor structure optimization. Jung *et al.* designed an IPMSM with asymmetric rotor for reducing vibration under certain load condition [115]. To reduce the usage of expensive rare-earth PM, a spoke-type motor was designed to have both NdFeB and ferrite magnets, and the results show that it cannot only gain low PM cost, but also achieve high flux-weakening and demagnetization withstand capabilities [114]. Liu *et al.* investigated the parameter and performance calculations of IPMSMs with different rotor structures such as U-shape, V-shape, spoke-type and circumferential-type PMs [116]. Dorrell *et al.* studied different rotor topologies based on the spoke design for hybrid EVs [117]. Sun *et al.* analysed the performance of IPMSM by using the model predictive control strategy [118].

In this chapter, an IPMSM prototype for EV propulsion is selected as the study case to develop the *d*- and *q*-axis ECMs with predictable core loss. The *d*- and *q*-axis ECMs of the PMSM greatly benefit the development of the modern motor control theory, and they

work the same as the analytical formulas which can provide a fast computation with good indication of how a parameter may affect the motor performance [119-121]. On the other hand, the numerical methods like finite-element analysis (FEA) can achieve more accurate results as they can take into account the geometry details and the nonlinear properties of magnetic materials [122-125]. Therefore, the major motor parameters in *d*- and *q*-axis ECMs, such as the winding flux and back electromotive force (EMF), winding inductance, and the core loss in various load conditions, are calculated with the assistance of the FEA.

In the last section of this chapter, an improved maximum torque per ampere current control of the PMSM considering both the core loss and copper loss, which is derived from the proposed *d*- and *q*-axis ECMs with the predictable core loss, is developed theoretically.

5.2 Analysis of the IPMSM

Fig. 5-1 shows the structure of the IPMSM prototype. The top figure illustrates the schematic diagram of the rotor assembly, and the bottom figure shows the photos of the fabricated rotor and stator. Table 5-1 lists the major dimensions and parameters.

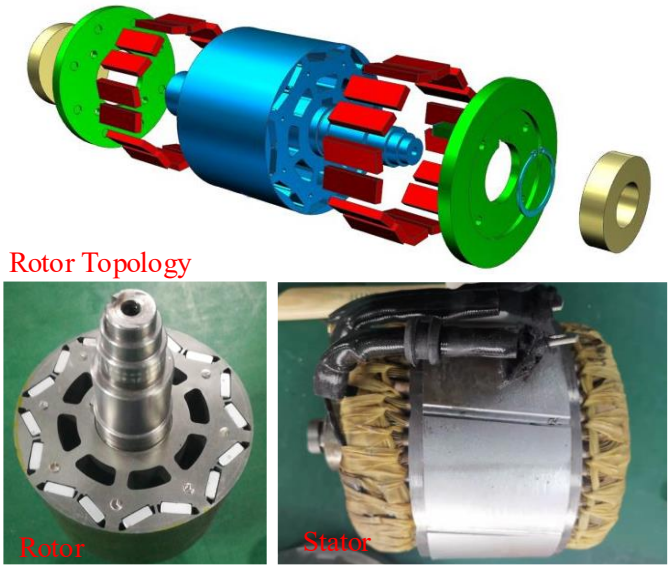

Fig. 5-1. The IPMSM structure.

Table 5-1 Key dimensions and design parameters

Dimension	Value
Number of phases	3
Number of slots	48
Number of poles	8
Number of magnets per pole	2
Core material	35WW270
Stator outer diameter (mm)	200
Stator inner diameter (mm)	135
Stator axial length (mm)	108
Rotor outer diameter (mm)	134
Air-gap length (mm)	0.5
Tooth width (mm)	6.35
Winding type	Double layer
Number of coil turns	4
Number of winding branches	4
Pitch of coil (slots)	5
Copper wire diameter (mm)	0.8

The motor is designed to have a rated speed of 3600 rpm with a rated power of 20 kW, delivering a rated torque of 53 Nm. The maximum speed is 5500 rpm, the maximum power is 40 kW, and the maximum torque is 180 Nm.

To accurately calculate the key motor parameters, the magnetic field distribution is worked out by the two-dimensional (2-D) FEA. Fig. 5-2 plots the magnetic flux density distribution at no-load, i.e., there is no current following through the stator windings.

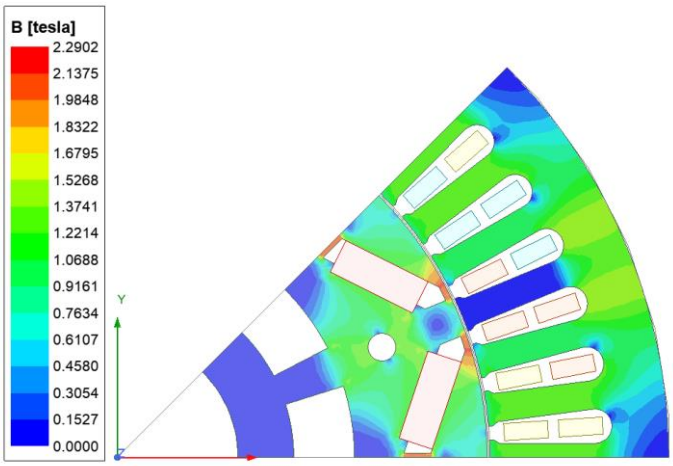

Fig. 5-2. 2D magnetic field distribution in the IPMSM.

5.2.1 Magnetic Flux and Back EMF

Based on the 2D FEA results of the magnetic flux density distribution at the no-load condition of the IPMSM, the curves of the radial and circumferential components of the air-gap magnetic flux density against rotor position in electrical degree can be obtained,

as shown in Fig. 5-3. The maximum value of the radial component of the air-gap flux density, depicted by the blue solid line, is about 0.87 T. The maximal circumferential flux density is around 0.18 T.

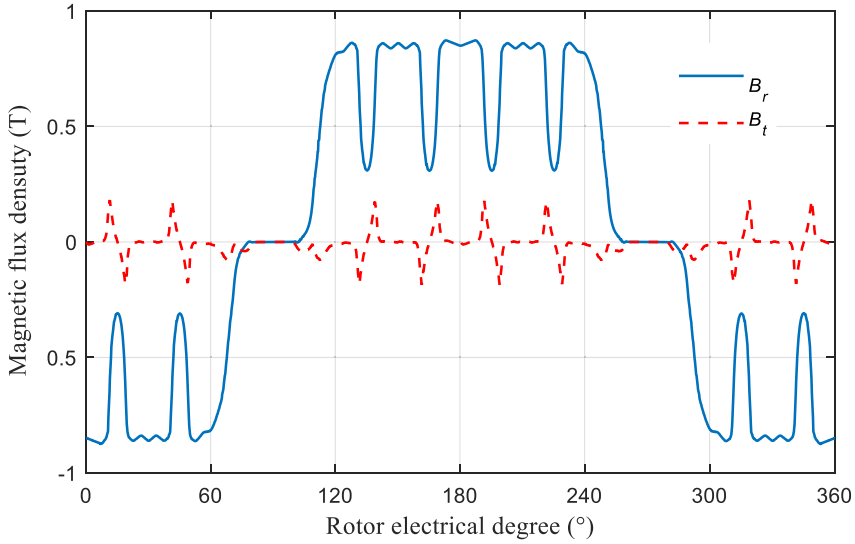

Fig. 5-3. Radial and circumferential components of air-gap magnetic flux density versus rotor position.

The V-shaped IPMSM air-gap flux density waveform can be approximately simplified as a flat-topped wave rather than the sine wave. Although there are a large amount of harmonics in the air gap flux density, the phase winding is formed with short-pitch and distributed coils, then the effect of higher-order harmonics of the flux has been greatly reduced and hence the back EMF in the phase winding approximates sinusoidal, which is shown in Fig. 5-4.

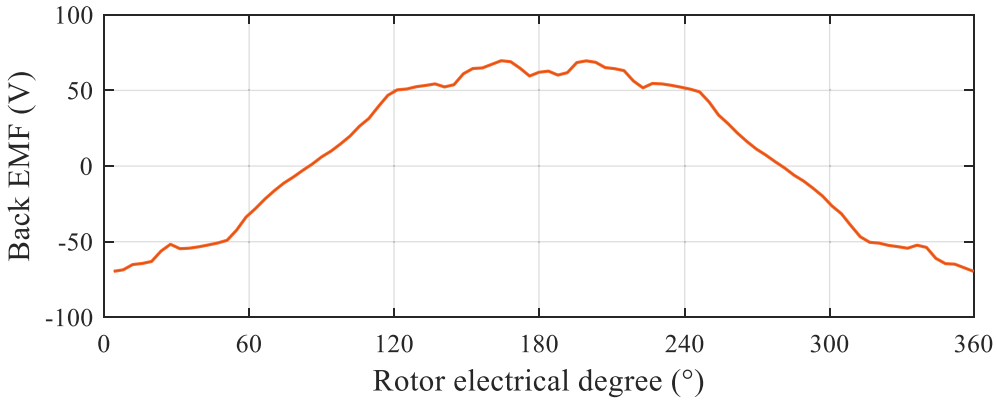

Fig. 5-4. Back EMF in per phase versus rotor position at rated speed.

The root mean square (RMS) value of the back EMF of a phase winding at the rated speed of 3600 rpm can be computed as 51.06 V. When the flux remains constant, e.g., using the

variable voltage variable frequency (VVVF) control, the EMF constant can be calculated as 0.03386 Vs by $k_{emf}=E_1/\omega_e$, where ω_e is the electrical angular speed.

5.2.2 Winding Resistance

Ignoring the skin effect of the alternating current, the phase winding resistance can be computed by the following equation

$$R_{s1}=\frac{\rho l_1}{N_b A_{cu}} \tag{5.1}$$

where ρ=1.75×10^{-8} Ωm is the electrical resistivity at the room temperature 20 ºC, l_1 is the total length of the phase winding, A_{cu} is the cross-sectional area of the copper wire, and N_b is the number of strands. The total length of one phase wining is 7.53 m, and the phase resistance is computed as 0.0699 Ω.

Generally, the rated temperature is much higher than the room temperature. Thus, taking the influence of the temperature into account, the stator winding resistance can be modified by

$$R_s=R_{s1}\frac{234.5+t_2}{234.5+t_1} \tag{5.2}$$

where t_1 is the room temperature, and t_2 the rated operation temperature. Thus, the phase resistance can be modified as 0.0974 Ω when the operational temperature is 120 ºC.

5.2.3 Winding Inductance

When calculating the winding inductances of the PM motor, incremental inductances, also called differential inductances, should be computed rather than the secant inductances [97]. Thanks to the continuous improvement of ANSYS software, the incremental inductances can be obtained conveniently via the latest versions. Fig. 5-5 illustrates the incremental self-inductances of three phase versus rotor position at the no-load condition.

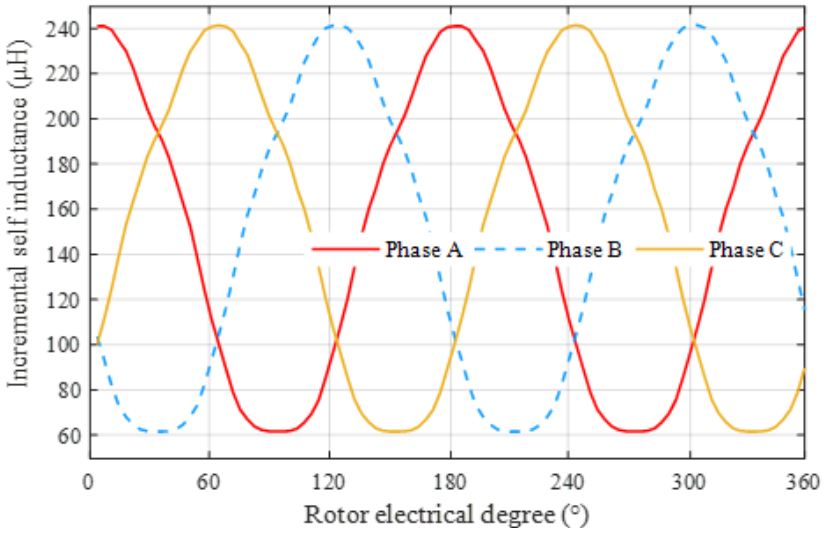

Fig. 5-5. Incremental self-inductance of three phase windings versus rotor position at no-load condition.

Taking the position of maximum self-inductance of phase A as the reference zero, the three phase incremental inductances can be written as

$$\begin{cases} L_{AA} = 149.36 + 89.74\cos 2\theta \\ L_{BB} = 149.36 + 89.74\cos 2(\theta - 120^\circ) \\ L_{CC} = 149.36 + 89.74\cos 2(\theta + 120^\circ) \end{cases} \tag{5.3}$$

where θ is the rotor position in electrical degrees, and the unit of inductance is μH.

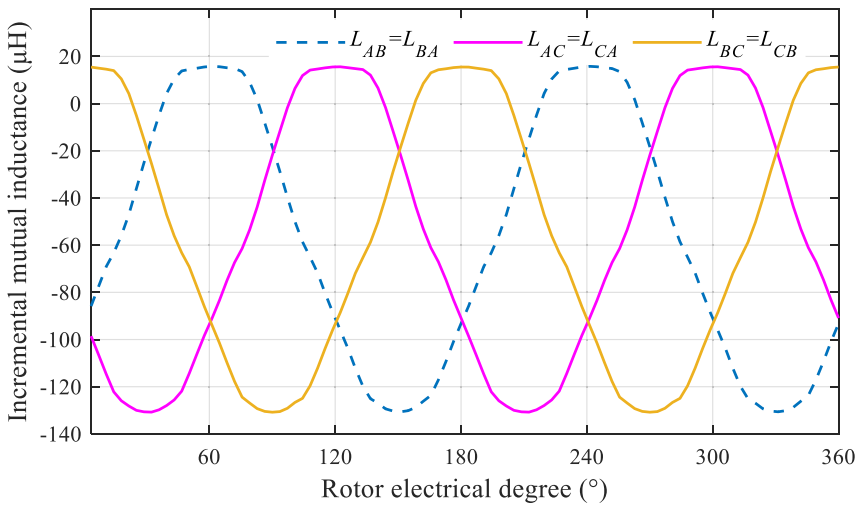

Fig. 5-6. Incremental mutual-inductance of three phase windings versus rotor position at no-load condition.

Similarly, the incremental mutual inductances of three phases at the no-load condition are shown in Fig. 5-6, and can be expressed as

$$\begin{cases} L_{AB} = L_{BA} = -56.8 + 73.2\cos 2(\theta + 120^\circ) \\ L_{BC} = L_{CB} = -56.8 + 73.2\cos 2(\theta) \\ L_{AC} = L_{CA} = -56.8 + 73.2\cos 2(\theta - 120^\circ) \end{cases} \tag{5.4}$$

Therefore, the inductance matrix can be obtained

$$L_{ABC} = \begin{bmatrix} L_{AA} & L_{AB} & L_{AC} \\ L_{BA} & L_{BB} & L_{BC} \\ L_{CA} & L_{CB} & L_{CC} \end{bmatrix} \tag{5.5}$$

In the modern motor control areas, especially in the vector control, the ECMs or mathematical models of the PMSM under the *d-q* axis reference frame are widely used.

The transformation matrix C from 3-phase rotary reference frame to 3-phase stationary reference frame and its inverse matrix C^{-1} are defined as

$$C = \begin{bmatrix} \cos\theta & -\sin\theta & 1 \\ \cos(\theta - 120^\circ) & -\sin(\theta - 120^\circ) & 1 \\ \cos(\theta + 120^\circ) & -\sin(\theta + 120^\circ) & 1 \end{bmatrix} \tag{5.6}$$

$$C^{-1} = \frac{2}{3}\begin{bmatrix} \cos\theta & \cos(\theta - 120^\circ) & \cos(\theta + 120^\circ) \\ -\sin\theta & -\sin(\theta - 120^\circ) & -\sin(\theta + 120^\circ) \\ 1/2 & 1/2 & 1/2 \end{bmatrix} \tag{5.7}$$

The currents and flux linkage of the PMSM under different reference frames have the relationship as follows

$$i_{ABC} = Ci_{dqo} \tag{5.8}$$

$$\lambda_{dqo} = C^{-1}\lambda_{ABC} = C^{-1}L_{ABC}i_{ABC} = C^{-1}L_{ABC}Ci_{dqo} = L_{dqo}i_{dqo} \tag{5.9}$$

Therefore, the inductances under 3-phase rotary reference can be calculated as

$$L_{dqo} = C^{-1}L_{ABC}C \tag{5.10}$$

Implementing the reference frame transformation, the incremental *d*-axis and *q*-axis inductances at the no-load condition are determined as L_d=83.955 μH and L_q=328.365 μH.

Actually, the inductances of the PMSM are not only determined by the PMs flux but also by the winding currents. Due to the nonlinear magnetic properties of the steel sheet, the incremental *d*-axis and *q*- axis inductances decrease with increasing winding currents, as shown in Fig. 5-7.

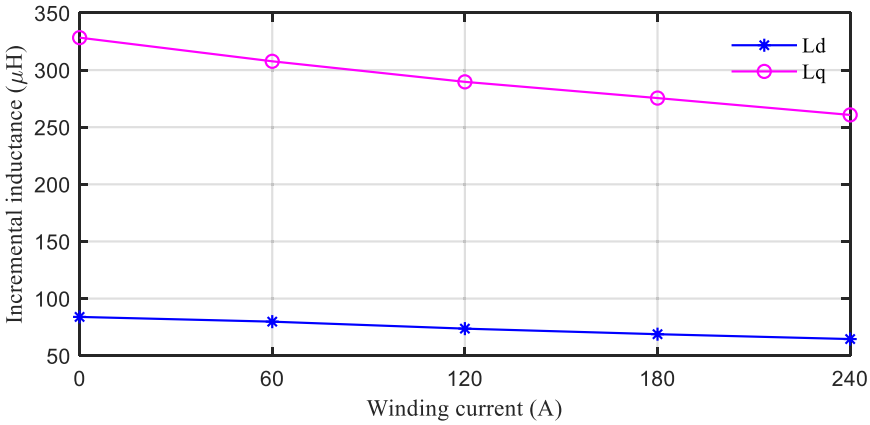

Fig. 5-7. Incremental d-axis and q- axis inductances versus winding current.

5.2.4 Electromagnetic Torque

When the motor is operated under the field-oriented control with zero *d*-axis current, the armature current is in phase with the back EMF, then electromagnetic torque constant is determined as 0.40632 Nm/A by

$$k_T = \frac{T_{em}}{I} = \frac{P_{em}}{\omega_r I} = \frac{3E_1 pI}{2\omega_e I} = 1.5P * k_{emf} \tag{5.11}$$

where ω_r is the mechanical angular speed of the rotor, and P the number of poles.

5.2.5 Core Loss

The core loss may take a significant part of the power loss, particularly when the machine operates at high speeds and with large currents. The core loss is caused by the magnetic field variation in the motor cores, and it is usually computed by the Berttoti's three-term formula [95, 126, 127], which consists of the hysteresis loss P_h, eddy current loss P_e and anomalous loss P_{an}.

$$P_c = P_h + P_e + P_{an} = k_h f B_m^{\alpha} + k_e f^2 B_m^2 + k_{an} f^{1.5} B_m^{1.5} \tag{5.12}$$

where f is the frequency of the magnetic field, and B_m the magnitude of the magnetic flux density. k_h, α, k_e, k_{an} are the loss coefficients, which can be determined by curve-fitting the core loss data measured on a standard material sample under different frequencies and magnetic flux densities.

Fig. 5-8 presents the core loss of core material (35WW270) measured by Epstein test apparatus. The core loss of sample no-oriented electrical sheet steel increases with the magnetic field frequency and density.

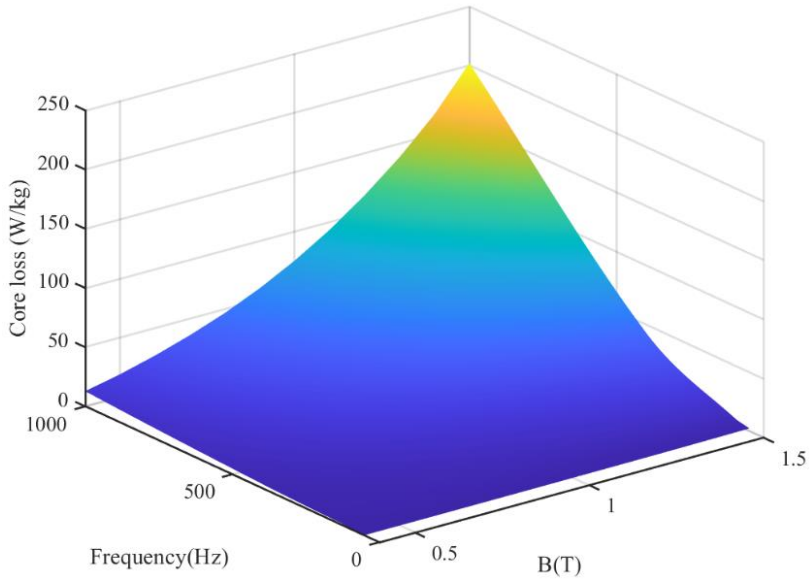

Fig. 5-8. Core loss of no-oriented electrical sheet steel (35WW270).

Fig. 5-9 illustrates the core loss of the PMSM based on the finite element method, while the motor speed is in the range of 600 - 6000 rpm, and the operating conditions cover no-load and various loads (the root mean square values of the phase currents are 60A, 120A, 180A and 240A, respectively), and the control strategy is with i_d=0. Particularly, 180A is the rated current of this PMSM prototype. Due to the no-linear magnetic characteristics of the stator core, the increment of the core loss per 60A is non-uniform. The core loss increases slightly when the winding currents rise from 180A to 240A, because the stator core is approaching magnetic saturation in this condition.

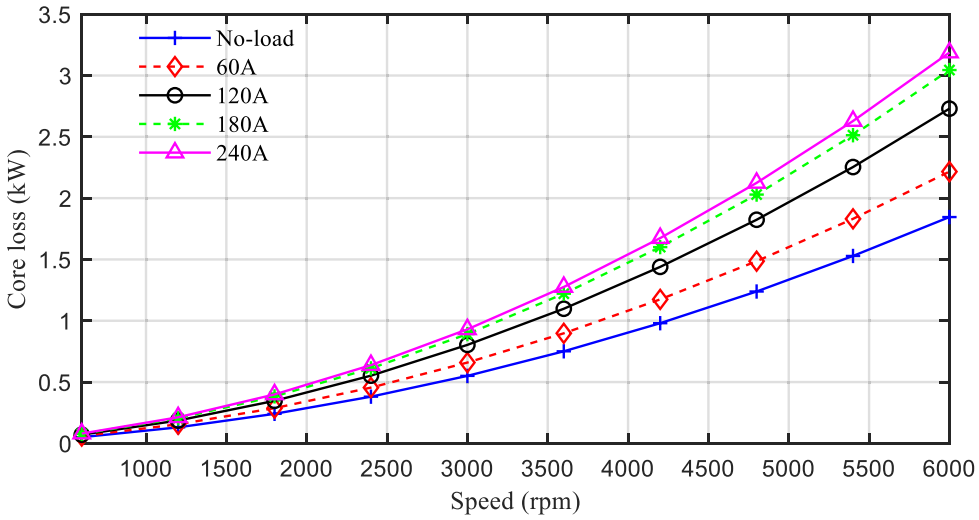

Fig. 5-9. Finite-element analysis of core loss under different working speeds and phase current conditions.

Fig. 5-10 compares the copper loss and core loss of the IPMSM at different speeds and armature currents. It is distinct that the core loss increases significantly with the motor speed, and exceeds the copper loss and becomes the dominant component of the electromagnetic loss when in the medium and high speed ranges. Obviously, ignoring the core loss during the modeling and performance analysis would lead to large errors.

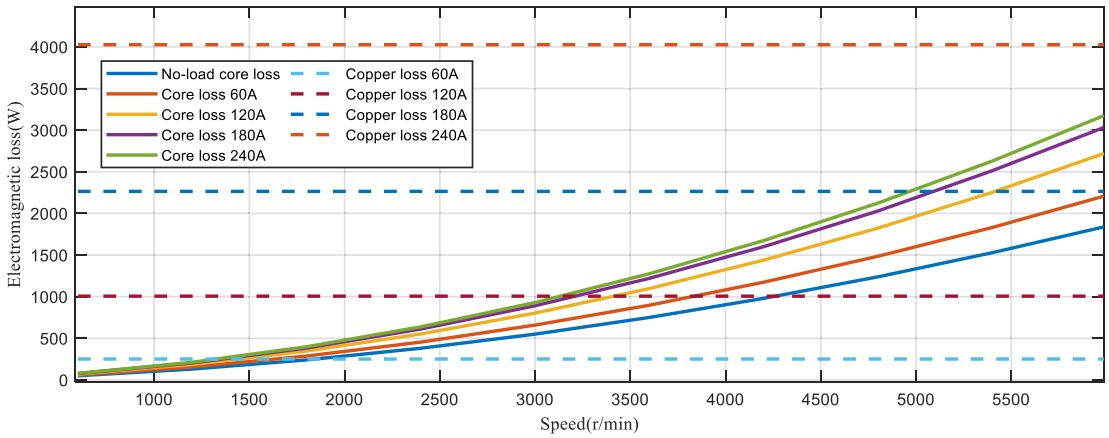

Fig. 5-10. Comparisons of the core loss and copper loss under different speeds and currents.

5.3 *d*- and *q*-axis ECMs of the PMSM with Predictable Core loss

The equivalent electrical circuit is widely applied in the motor characteristic analysis as it can provide fast computation with reasonable accuracy and the effect of motor parameters on the motor performance can be easily tracked. The traditional circuits rarely include the core loss, which may decrease the performance prediction accuracy, so some

circuit models accounting the core loss have been proposed [13, 18, 20]. However, these models mainly focus on the rated operation point and may produce large calculation errors when the motor runs with large ranges of speed and load. Therefore, an improved electrical circuit model is applied as shown in Fig. 5-11, which can consider the core loss at different speeds and load currents.

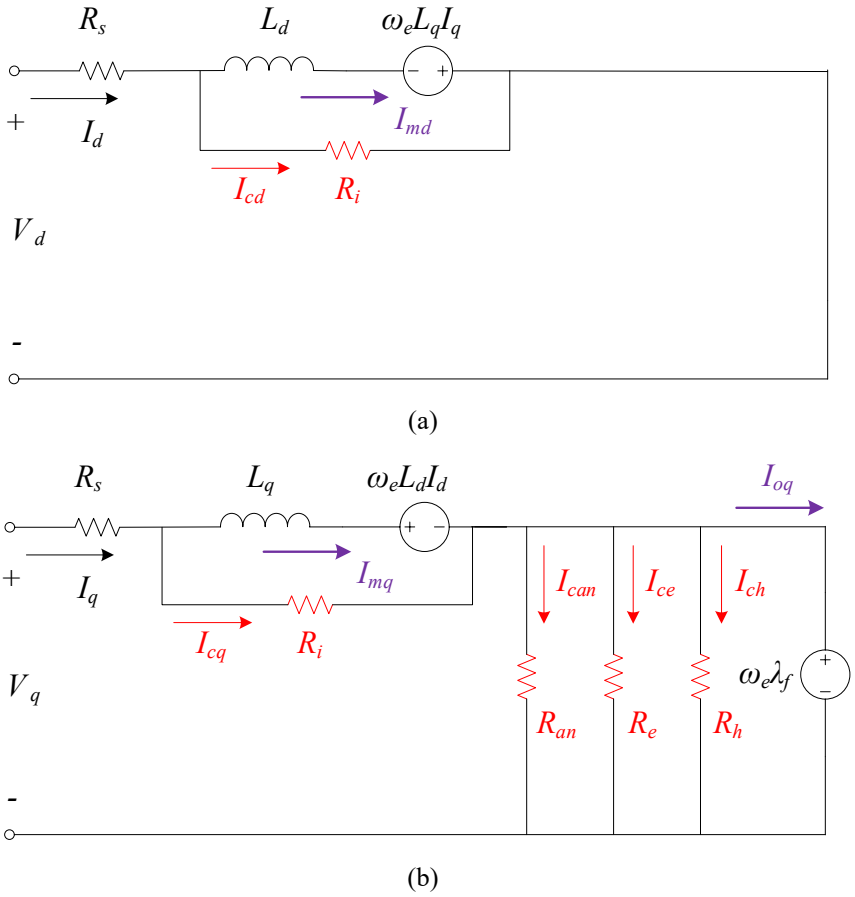

Fig. 5-11 ECM considering core loss and magnetic saturation effect: (a) *d*-axis; (b) *q*-axis.

According to Fig. 5-11, the mathematical models of the equivalent circuits for *d*- and *q*-axis voltages and currents are given as follows

$$\begin{cases} V_d = R_s I_d + pL_d I_{md} - \omega_e L_q I_q \\ V_q = R_s I_q + pL_q I_{mq} + \omega_e L_d I_d + \omega_e \lambda_f \end{cases} \tag{5.13}$$

$$\begin{cases} I_d = I_{cd} + I_{md} \\ I_q = I_{cq} + I_{mq} = I_{can} + I_{ce} + I_{ch} + I_{oq} \end{cases} \tag{5.14}$$

The currents can be calculated as follows

$$I_{cd} = -\frac{\omega_e L_q I_q}{R_i} \tag{5.15}$$

$$I_{cq} = \frac{\omega_e L_d I_d}{R_i} \tag{5.16}$$

$$I_{can} = \frac{\omega_e \lambda_f}{R_{an}} \tag{5.17}$$

$$I_{ce} = \frac{\omega_e \lambda_f}{R_e} \tag{5.18}$$

$$I_{ch} = \frac{\omega_e \lambda_f}{R_h} \tag{5.19}$$

where V_d and V_q are the *d*- and *q*-axis terminal voltages, I_d and I_q the *d*- and *q*-axis armature currents, L_d and L_q the *d*- and *q*-axis inductances, I_{cd} and I_{cq} the *d*- and *q*-axis load core loss currents, I_{md}, I_{mq}, and I_{oq} the *d*- and *q*-axis magnetizing currents, I_{can}, I_{ce}, and I_{ch} the no-load core loss currents, respectively. R_h, R_e, R_{an}, and R_i are respectively the equivalent hysteresis loss, eddy current, anomalous loss, and load core loss resistances. R_s is the armature winding resistance per phase, λ_f the permanent magnet flux linkage, ω_e the rotor speed in electrical angular frequency, and p the differential operator ($=d/dt$).

According to the improved ECM, the no-load core loss P_{co} is obtained as

$$\begin{aligned} P_{co} &= \frac{3}{2}(R_{an} I_{can}^2 + R_e I_{ce}^2 + R_h I_{ch}^2) \\ &= \frac{3}{2}(\omega_e \lambda_f)^2 (\frac{1}{R_h} + \frac{1}{R_e} + \frac{1}{R_{an}}) \end{aligned} \tag{5.20}$$

Compared with the mathematical model of the core loss (5.12), the no-load core loss P_{co} also can be written as

$$P_{co} = k_h' f + k_e' f^2 + k_{an}' f^{1.5} \tag{5.21}$$

Via curve-fitting the no-load core loss in Fig. 5-9, the coefficients can be identified as k_h'=0.8699, k_e'=0.009217, and k_{an}'=0.002913. Assuming that the PM flux is constant

during the operation and comparing (5.20) and (5.21), these equivalent core loss resistances are R_h=0.02486ω_e Ω, R_e=14.74 Ω, and R_{an}=13.1576$\omega_e^{1/2}$ Ω, respectively.

Furtherly, the load core loss P_c and the equivalent load core loss resistance R_i can be deduced as

$$\begin{aligned} P_c &= P_{co} + \frac{3}{2}[R_i(I_{cd}^2 + I_{cq}^2)] \\ &= P_{co} + \frac{3}{2}[\frac{(\omega_e L_q I_q)^2}{R_i} + \frac{(\omega_e L_d I_d)^2}{R_i}] \end{aligned} \tag{5.22}$$

$$R_i = \frac{3}{2}[\frac{(\omega_e L_q I_q)^2 + (\omega_e L_d I_d)^2}{P_c - P_{co}}] \tag{5.23}$$

Analyzing the load core loss data in Fig. 5-9, the equivalent load core loss resistance can be worked out and as shown in Fig. 5-12, and it is a function of the motor speed and winding current. However, in engineering applications, a lower-order function with exact expressions and acceptance calculation error range is prioritized. Therefore, the function of the equivalent core loss resistance can be simplified as: R_i = -8.463+0.18I_p+0.0075ω_e, and I_p is the root mean square value of the phase current.

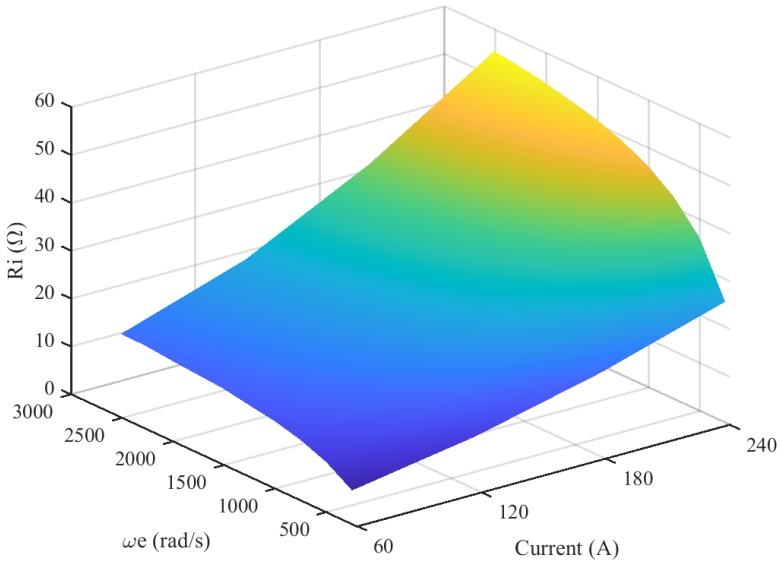

Fig. 5-12 Equivalent load core loss resistance versus winding current and speed in electrical angular frequency.

The electromagnetic power P_{em} and electromagnetic torque T_{em} of the PMSM can be determined as

$$P_{em} = \frac{3}{2}\omega_e[\lambda_f I_{oq} + L_d I_d I_{mq} - L_q I_{md} I_q] \tag{5.24}$$

$$T_{em} = \frac{P_{em}}{\omega_m} = \frac{3}{4}P[\lambda_f I_{oq} + L_d I_d I_{mq} - L_q I_{md} I_q] \tag{5.25}$$

where P is the number of poles of the PMSM, and ω_m the rotor speed in mechanical angular frequency.

The copper loss P_{cu} can be estimated using the circuit in Fig. 5-11:

$$P_{cu} = \frac{3}{2}R_s(I_d^2 + I_q^2) \tag{5.26}$$

Ignoring the eddy current loss of PMs and stray loss, the input power P_{in}, output power P_{out}, and efficiency η of the PMSM can be obtained as follows

$$P_{in} = \frac{3}{2}(V_d I_d + V_q I_q) = P_{em} + P_{cu} + P_c \tag{5.27}$$

$$P_{out} = P_{em} - P_{mech} \tag{5.28}$$

$$\eta = {P_{out}}/{P_{in}} \times 100\% \tag{5.29}$$

where P_{mech} is the mechanical loss of the PMSM.

5.4 Maximum Torque Per Ampere Current Control Considering Both the Core Loss and Copper Loss

Fig. 5-13 presents the schematic diagram of the stator current vector in the *d*- and *q*-axis reference frame.

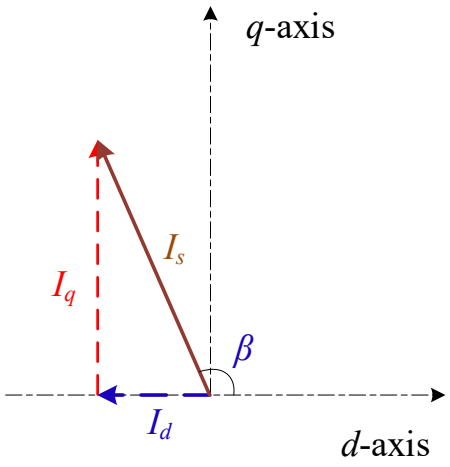

Fig. 5-13 Schematic diagram of the stator current vector.

According to Fig. 5-13, the *d*- and *q*-axis currents can be calculated as

$$\begin{cases} I_d = I_s \cos\beta \\ I_q = I_s \sin\beta \end{cases} \tag{5.30}$$

where I_s is the stator current vector, and β is the angle between the *d*-axis and the stator current vector.

To achieve the maximum torque per ampere (MTPA) current control of the PMSM is to find the minimum stator current for a certain torque. The optimization objective of the stator current can be established as follows

$$I_s = \min\sqrt{I_d^2 + I_q^2} \tag{5.31}$$

Combining (5.14) and (5.15), we have

$$I_{md} = I_d - I_{cd} = I_d + \frac{\omega_e L_q I_q}{R_i} \tag{5.32}$$

Combining (5.14) and (5.16), we have

$$I_{mq} = I_q - I_{cq} = I_q - \frac{\omega_e L_d I_d}{R_i} \tag{5.33}$$

Combining (5.14) and (5.17-5.19), we have

$$I_{oq} = I_q - I_{can} - I_{ce} - I_{ch} = I_q - \frac{\omega_e \lambda_f}{R_{an}} - \frac{\omega_e \lambda_f}{R_e} - \frac{\omega_e \lambda_f}{R_h} \tag{5.34}$$

Substituting (5.32) - (5.34) into (5.25), the torque calculation formula can be rewritten as

$$T_{em} = \frac{3}{4} P[\lambda_f I_q + L_d I_d I_q - L_q I_q I_d - \frac{\omega_e (L_d^2 I_d^2 + L_q^2 I_q^2)}{R_i} - (\frac{\omega_e \lambda_f^2}{R_{an}} + \frac{\omega_e \lambda_f^2}{R_e} + \frac{\omega_e \lambda_f^2}{R_h})] \tag{5.35}$$

Establish a helper function as shown below

$$F = I_d^2 + I_q^2 + \chi \left\{ \begin{array}{l} \frac{3}{4} P[\lambda_f I_q + L_d I_d I_q - L_q I_q I_d - \frac{\omega_e (L_d^2 I_d^2 + L_q^2 I_q^2)}{R_i} \\ -(\frac{\omega_e \lambda_f^2}{R_{an}} + \frac{\omega_e \lambda_f^2}{R_e} + \frac{\omega_e \lambda_f^2}{R_h})] - T_{em} \end{array} \right\} \tag{5.36}$$

where χ is the Lagrange multiplier.

Take the partial derivatives of the above equation with respect to the *d*- and *q*-axis currents as well as the multiplier and make each of them equals to zero, respectively.

$$\frac{\partial F}{\partial I_d} = 2I_d + \frac{3}{4} \chi P[L_d I_q - L_q I_q - \frac{2\omega_e L_d^2}{R_i} I_d] = 0 \tag{5.37}$$

$$\frac{\partial F}{\partial I_q} = 2I_q + \frac{3}{4} \chi P[\lambda_f + L_d I_d - L_q I_d - \frac{2\omega_e L_q^2}{R_i} I_q] = 0 \tag{5.38}$$

$$\begin{aligned} \frac{\partial F}{\partial \chi} = \frac{3}{4} P[\lambda_f I_q + L_d I_d I_q - L_q I_q I_d - \frac{\omega_e (L_d^2 I_d^2 + L_q^2 I_q^2)}{R_i} \\ -(\frac{\omega_e \lambda_f^2}{R_{an}} + \frac{\omega_e \lambda_f^2}{R_e} + \frac{\omega_e \lambda_f^2}{R_h})] - T_{em} = 0 \end{aligned} \tag{5.39}$$

Note that L_d<L_q, and solving the above formula can obtain

$$I_d = \frac{-[\lambda_f + \frac{2\omega_e}{R_i}(L_d^2 - L_q^2) I_q] + \sqrt{[\lambda_f + \frac{2\omega_e}{R_i}(L_d^2 - L_q^2) I_q]^2 + 4(L_d - L_q)^2 I_q^2}}{2(L_d - L_q)} \tag{5.40}$$

$$I_q = \frac{[\frac{2\omega_e}{R_i}(L_d^2 - L_q^2)I_d] - \sqrt{[\frac{2\omega_e}{R_i}(L_d^2 - L_q^2)I_d]^2 + 4(L_d - L_q)[\lambda_f I_d + (L_d - L_q)I_q^2]}}{2(L_d - L_q)} \tag{5.41}$$

Substituting (5.40) into (5.35) yields

$$T_{em} = \frac{3}{4}P[\lambda_f I_q - (L_d - L_q)(\alpha I_q + \beta I_q^2 + I_q\sqrt{(\alpha + \beta I_q)^2 + I_q^2}) - \frac{\omega_e(L_d^2\Delta + L_q^2 I_q^2)}{R_i} - (\frac{\omega_e\lambda_f^2}{R_{an}} + \frac{\omega_e\lambda_f^2}{R_e} + \frac{\omega_e\lambda_f^2}{R_h})] \tag{5.42}$$

where

$$\alpha = \frac{\lambda_f}{2(L_d - L_q)} \tag{5.43}$$

$$\beta = \frac{\omega_e}{R_i}(L_d + L_q) \tag{5.44}$$

$$\Delta = (2\beta^2 + 1)I_q^2 + 4\alpha\beta I_q + (2\beta I_q + 2\alpha)\sqrt{(\alpha + \beta I_q)^2 + I_q^2} + 2\alpha^2 \tag{5.45}$$

From (5.42) - (5.45), the *q*-axis current can be obtained for a given torque, and hence the *d*-axis current is solved by (5.40) and the optimal stator current is calculated by (5.31).

Fig. 5-14 shows the schematic diagram of the improved MTPA drive system. This improved MTPA control strategy takes into account not only the copper loss but also the core loss, and has higher accuracy and reliability in guiding practical applications than the traditional one. The outer loop of the drive system is the motor speed loop, in which a PI controller is employed to regulate the stator current. The inner loops of the proposed drive system are the *d*- and *q*-axis currents loops. For a given torque, the reference values of the d-axis and q-axis currents are derived by the improved MPTA controller, and the errors between the reference values and the actual values collected by the sensor will enter the two PI controllers to generate voltage signals respectively. Furtherly, the switch signals of the inverter are obtained via the space vector pulse width modulation (SVPWM), and hence drive the PMSM to acquire the maximum torque per ampere current.

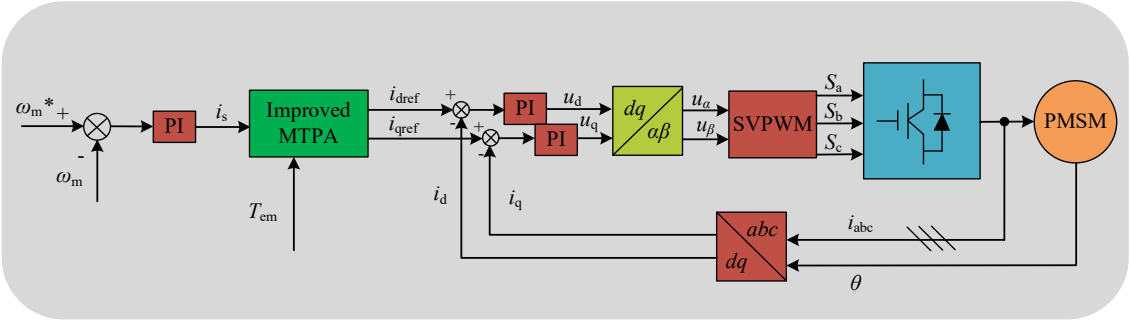

Fig. 5-14 Schematic diagram of the improved MTPA drive system.

The designed IPMSM has been fabricated and some experimental results on the motor prototype have been obtained. Fig. 5-15 shows the testing setup, where the prototype is connected to another electrical machine as the load or driver via a torque/speed transducer.

(a) Stator and rotor structure

(b) Experimental platform

Fig. 5-15 Testing setup of prototype.

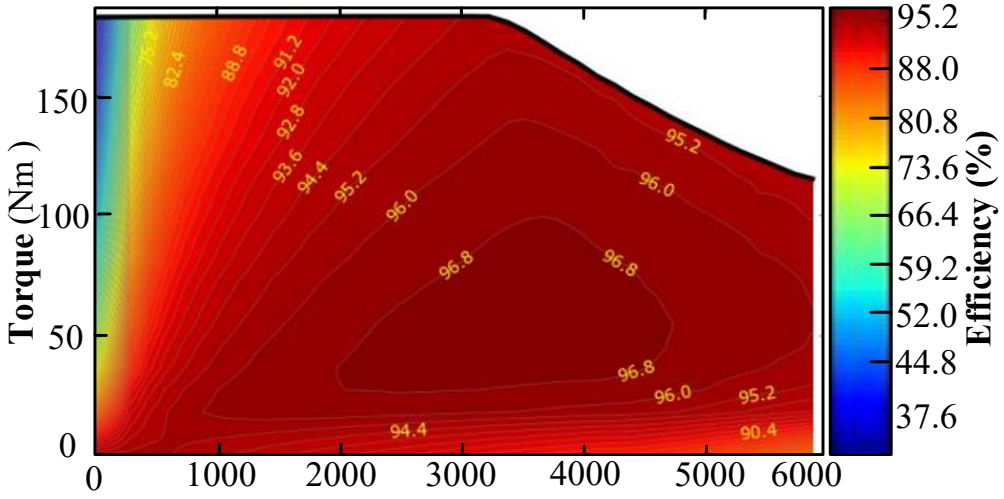

Fig. 5-16 Measured efficiency map of the IPMSM.

As the first step of this study, the efficiency map of the IPMSM in the speed range of 0-6000 r/min is measured under the i_d=0 control strategy, as shown in Fig. 5-16. The maximum torque of the IPMSM could reach 180 Nm, while the maximum efficiency is 96.8%, which well satisfied the design requirements.

5.5 Conclusion

This chapter analyses the electromagnetic characteristic and parameters of an IPMSM prototype with the assistance of the 2-D FEM. Particularly, due to the magnetic saturation effect, the incremental *d*-axis and *q*- axis inductances decrease with increasing winding currents. However, the influence of the magnetic saturation of the stator core is not only on incremental inductances but also on the core loss. Not only does the core loss increase with motor speed, it also increases with stator current, but with a nonlinear characteristic. When the magnetic flux density in the stator core approaches the saturation value, the core loss increases slowly. Thus, to model these special properties of the core loss, an improved *d*-axis and *q*- axis ECMs of the core loss considering the magnetic saturation effect is presented. Correspondingly, the calculation formulas of electromagnetic power, electromagnetic torque, efficiency, etc. have been modified. The proposed *d*-axis and *q*-axis ECMs and parameter identification methods are general to other prototypes of the PMSM, such as the surface-mounted PMSM, interior PMSM, claw-pole PMSM, transverse flux PMSM, and axial flux PMSM.

Finally, this chapter theoretically establishes the maximum torque per ampere current control of the PMSM considering both the core loss and copper loss. Simulations and experiments of the proposed control method will be conducted in future work.

CHAPTER 6. CONCLUSION AND FUTURE WORKS

6.1 Conclusion

ECM is able to calculate the electromagnetic properties of the PMSM in an intuitive way. However, the conventional ECMs ignore the core loss, resulting in low accuracy and difficulty to control and optimize the core loss. This thesis investigated the development of the PMSM ECMs with predictable core loss, and it is noted that generally the equivalent core loss resistance is connected in parallel with the magnetizing branch. This is based on the assumption that the core loss is approximately proportional to the square of the flux density and the machine runs at a fixed speed, e.g., synchronous speed. However, modern PMSMs often operate with variable frequency (speed) and variable flux density (e.g., changing load condition), so the core loss would change accordingly. In addition, a brief review of core loss measurement methods is introduced to help understanding the coupled mechanical loss and core loss of the PMSM.

Core loss in the PMSM is caused by the alternating magnetic flux, of which only the magnitude varies with time, and rotational magnetic flux, of which both the magnitude and direction of the magnetic flux vary with time. Therefore, according to the flux density vectors in the PMSM, the core loss can be divided into alternating core loss and rotational core loss, and their mechanisms and mathematical models are completely different. Each kind of core loss consists of three parts: hysteresis loss, eddy current loss, and anomalous loss. In this thesis, the core loss with 3-D rotating magnetic field is investigated, and then the core loss is modelled into the ECM of the PMSM. To imitate the core loss in a wide speed range, the equivalent core loss resistance is modelled as a function of the motor speed, which effectively enhances the prediction accuracy. Furtherly, an improved DPCC with the novel predictive model to enhance the performance of the PMSM drive system is established. Simulations suggest that the dynamic speed response and the torque robustness of the drive system with this improved DPCC are enhanced effectively.

ECM with predictable core loss has not been limited to a standard topology, since the mechanism of the core loss has not been fully understood yet, hence its modeling in the ECM is also a pending issue. To overcome the drawback that the previous proposed ECM overestimates the core loss caused by the armature current, a novel generalized per-phase

ECM of the PMSM with predictable core loss is proposed. When the PMSM operates at no-load condition, three equivalent resistances R_h, R_e and R_{an} are adopted to respectively present the hysteresis loss, eddy current loss and anomalous loss at no-load conditions. When the PMSM operates at loading conditions, an equivalent resistance R_i connected in parallel with the synchronous inductance L_s is adopted to depict the extra core loss due to the load current and take the magnetic saturation effect into consideration. The summation of the power loss in R_i, R_h, R_e and R_{an} represents the core loss when the PMSM operates at loading conditions. Experimental tests of the PMSM prototype validate the excellence of the proposed ECM.

Furtherly, the generalized *d*-axis and *q*- axis ECMs of the PMSM with predictable core loss is also developed, which benefit motor control and enable the core loss management. The equivalent resistances R_h, R_e and R_{an}, which stand for the hysteresis loss, eddy current loss and anomalous loss at no-load conditions, are connected in parallel with the electromotive force $\omega_e\lambda_f$ in the *q*-axis ECM, respectively. The equivalent resistance R_i, which represents the extra core loss due to the load current, is connected in parallel with the series branch of L_d and $\omega_e L_q I_q$ in the *d*-axis ECM, while with the series branch of L_q and $\omega_e L_d I_d$ in the *q*-axis ECM, respectively. Moreover, based on the proposed *d*- and *q*-axis ECMs with predictable core loss, an improved maximum torque per ampere current control of the PMSM considering both the core loss and copper loss is established theoretically.

6.2 Possible Future Works

This thesis mainly focusses on the equivalent circuit models of the permanent magnet synchronous motor with predictable core loss, including the per-phase circuit model and the *d*- and *q*-axis circuit models. A few of the possible future works are listed below:

(1) The mathematical models of the core loss in this thesis, including those with the 1-D alternating, 2-D rotating, and 3-D rotating magnetic field, ignore the effect of temperature. Further works should incorporate the temperature as a factor of the core loss.

(2) The core loss measurement is very tough and demanding work, but it is of great significance. In particular, the core loss measurement under various load conditions is urgently required.

(3) Per-phase equivalent circuit model facilitates motor design, but the saliency of the PMSM cannot be reflected in the proposed equivalent circuit models of this thesis. An improved per-phase model with predictable core loss and salient effect would greatly benefit.

(4) More simulations/experiments on the robustness of the proposed equivalent circuit models and the equivalent core loss resistances identification methods should be included.

(5) Investigate more applications of the proposed equivalent circuit models of the permanent magnet synchronous motor with predictable core loss, not only as the predictive model of the model predictive control but also in field-oriented control and direct torque control.

(6) Core loss optimization and management strategies can be established based on the proposed equivalent circuit models in this thesis, and hence the efficiency of the PMSM can be boosted.

REFERENCE

[1] C. He and T. Wu, "Analysis and design of surface permanent magnet synchronous motor and generator," *CES Transactions on Electrical Machines and Systems,* vol. 3, no. 1, pp. 94-100, 2019.

[2] C. Liu, Y. Xu, J. Zou, G. Yu, and L. Zhuo, "Permanent magnet shape optimization method for PMSM air gap flux density harmonics reduction," *CES Transactions on Electrical Machines and Systems,* vol. 5, no. 4, pp. 284-290, 2021.

[3] Y. Guo, J. Si, C. Gao, H. Feng, and C. Gan, "Improved fuzzy-based taguchi method for multi-objective optimization of direct-drive permanent magnet synchronous motors," *IEEE Transactions on Magnetics,* vol. 55, no. 6, pp. 1-4, 2019.

[4] B. Ozdincer and M. Aydin, "Design of innovative radial flux permanent magnet motor alternatives with non-oriented and grain-oriented electrical steel for servo applications," *IEEE Transactions on Magnetics,* vol. 58, no. 2, pp. 1-4, 2022.

[5] Z. Q. Zhu and D. Howe, "Electrical machines and drives for electric, hybrid, and fuel cell vehicles," *Proceedings of the IEEE,* vol. 95, no. 4, pp. 746-765, 2007.

[6] K. T. Chau, C. C. Chan, and C. Liu, "Overview of permanent-magnet brushless drives for electric and hybrid electric vehicles," *IEEE Transactions on Industrial Electronics,* vol. 55, no. 6, pp. 2246-2257, 2008.

[7] M. Onsal, Y. Demir, and M. Aydin, "A new nine-phase permanent magnet synchronous motor with consequent pole rotor for high-power traction applications," *IEEE Transactions on Magnetics,* vol. 53, no. 11, pp. 1-6, 2017.

[8] Y. Xu, M. Ai, Z. Xu, W. Liu, and Y. Wang, "Research on interior permanent magnet synchronous motor based on performance matching of electric bus," *IEEE Transactions on Applied Superconductivity,* vol. 31, no. 8, pp. 1-4, 2021.

[9] M. Polat, A. Yildiz, and R. Akinci, "Performance analysis and reduction of torque ripple of axial flux permanent magnet synchronous motor manufactured for electric vehicles," *IEEE Transactions on Magnetics,* vol. 57, no. 7, pp. 1-9, 2021.

[10] V. Honsinger, "Performance of polyphase permanent magnet machines," *IEEE Transactions on Power Apparatus and Systems,* no. 4, pp. 1510-1518, 1980.

[11] R. S. Colby and D. W. Novotny, "Efficient operation of surface-mounted PM synchronous motors," *IEEE transactions on industry applications,* no. 6, pp. 1048-1054, 1987.

[12] J. Hur, "Characteristic analysis of interior permanent-magnet synchronous motor in electrohydraulic power steering systems," *IEEE Transactions on Industrial Electronics,* vol. 55, no. 6, pp. 2316-2323, 2008.

[13] J. Y. Lee, S. H. Lee, G. H. Lee, J. P. Hong, and J. Hur, "Determination of parameters considering magnetic nonlinearity in an interior permanent magnet synchronous motor," *IEEE Transactions on Magnetics,* vol. 42, no. 4, pp. 1303-1306, 2006.

[14] J. Song *et al.*, "Power density improvement design of the traction motor for the hybrid electric vehicle," in *INTELEC 2009-31st International Telecommunications Energy Conference*, 2009, pp. 1-4: IEEE.

[15] F. Fernandez Bernal, A. Garcia Cerrada, and R. Faure, "Determination of parameters in interior permanent-magnet synchronous motors with iron losses without torque measurement," *IEEE Transactions on Industry Applications,* vol. 37, no. 5, pp. 1265-1272, 2001.

[16] C. Dutta and S. Tripathi, "Comparison between conventional and loss dq model of PMSM," in *2016 International Conference on Emerging Trends in Electrical Electronics & Sustainable Energy Systems (ICETEESES)*, 2016, pp. 256-260: IEEE.

[17] M. N. Uddin, M. M. Rahman, B. Patel, and B. Venkatesh, "Performance of a loss model based nonlinear controller for IPMSM drive incorporating parameter uncertainties," *IEEE Transactions on Power Electronics,* vol. 34, no. 6, pp. 5684-5696, 2019.

[18] A. Consoli and G. Renna, "Interior type permanent magnet synchronous motor analysis by equivalent circuits," *IEEE Transactions on Energy Conversion,* vol. 4, no. 4, pp. 681-689, 1989.

[19] A. Consoli and A. Raciti, "Analysis of permanent magnet synchronous motors," *IEEE Transactions on Industry Applications,* vol. 27, no. 2, pp. 350-354, 1991.

[20] X. Ba, Y. Guo, J. Zhu, and C. Zhang, "An equivalent circuit model for predicting the core loss in a claw-pole permanent magnet motor with soft magnetic composite core," *IEEE Transactions on Magnetics,* vol. 54, no. 11, pp. 1-6, 2018.

[21] B. H. Lee, S. O. Kwon, T. Sun, J. P. Hong, G. H. Lee, and J. Hur, "Modeling of core loss resistance for d-q equivalent circuit analysis of IPMSM considering harmonic linkage flux," *IEEE Transactions on Magnetics,* vol. 47, no. 5, pp. 1066-1069, 2011.

[22] W. Xie, X. Wang, F. Wang, W. Xu, R. Kennel, and D. Gerling, "Dynamic loss minimization of finite control set-model predictive torque control for electric drive system," *IEEE Transactions on Power Electronics,* vol. 31, no. 1, pp. 849-860, 2016.

[23] O. Ojo, F. Osaloni, Z. Wu, and M. Omoigui, "A control strategy for optimum efficiency operation of high performance interior permanent magnet motor drives," in *38th IAS Annual Meeting on Conference Record of the Industry Applications Conference, 2003.*, 2003, vol. 1, pp. 604-610: IEEE.

[24] O. Solomon and P. Famouri, "Control and efficiency optimization strategy for permanent magnet brushless AC motors," in *2009 IEEE International Symposium on Industrial Electronics*, 2009, pp. 505-512: IEEE.

[25] Z. Huang, J. Fang, X. Liu, and B. Han, "Loss calculation and thermal analysis of rotors supported by active magnetic bearings for high-speed permanent-magnet electrical machines," *IEEE Transactions on Industrial electronics,* vol. 63, no. 4, pp. 2027-2035, 2016.

[26] X. Liu, G. Liu, and B. Han, "A loss separation method of a high-speed magnetic levitated PMSM based on drag system experiment without torque meter," *IEEE Transactions on Industrial Electronics,* vol. 66, no. 4, pp. 2976-2986, 2019.

[27] J.-H. Park, T.-Y. Lee, and J.-M. Kim, "Analysis and design of high speed permanent magnet synchronous motor for turbo blower system," in *2015 9th International Conference on Power Electronics and ECCE Asia (ICPE-ECCE Asia)*, 2015, pp. 1718-1723: IEEE.

[28] K. Yamazaki and H. Takeuchi, "Impact of mechanical stress on characteristics of interior permanent magnet synchronous motors," *IEEE Transactions on Industry Applications,* vol. 53, no. 2, pp. 963-970, 2017.

[29] S. Rahman and A. Knight, "Impact of heat treatment on core properties and IPMSM performance," in *IECON 2012-38th Annual Conference on IEEE Industrial Electronics Society*, 2012, pp. 1829-1834: IEEE.

[30] Z. Gmyrek and A. Cavagnino, "Assembly effects on stator cores of small synchronous reluctance motors," in *2017 IEEE Energy Conversion Congress and Exposition (ECCE)*, 2017, pp. 3179-3186: IEEE.

[31] S. W. Hwang, M. S. Lim, and J. P. Hong, "Hysteresis torque estimation method based on iron-loss analysis for permanent magnet synchronous motor," *IEEE Transactions on Magnetics,* vol. 52, no. 7, pp. 1-4, 2016.

[32] Y. An *et al.*, "Open-circuit air-gap magnetic field calculation of interior permanent magnet synchronous motor with V-shaped segmented skewed poles using hybrid analytical method," *IEEE Transactions on Magnetics,* vol. 57, no. 12, pp. 1-9, 2021.

[33] C. Liu, J. Lu, Y. Wang, G. Lei, J. Zhu, and Y. Guo, "Design issues for claw pole machines with soft magnetic composite Cores," *Energies,* vol. 11, no. 8, p. 1998, 2018.

[34] C. Liu, G. Lei, T. Wang, Y. Guo, Y. Wang, and J. Zhu, "Comparative study of small electrical machines with soft magnetic composite cores," *IEEE Transactions on Industrial Electronics,* vol. 64, no. 2, pp. 1049-1060, 2017.

[35] J. Zhao, M. Hua, and T. Liu, "Research on a sliding mode vector control system based on collaborative optimization of an axial flux permanent magnet synchronous motor for an electric vehicle," *Energies,* vol. 11, no. 11, p. 3116, 2018.

[36] F. F. Bernal, A. Garefa Cerrada, and R. Faure, "Loss-minimization control of synchronous machines with constant excitation," in *PESC 98 Record. 29th Annual IEEE Power Electronics Specialists Conference (Cat. No. 98CH36196)*, 1998, vol. 1, pp. 132-138: IEEE.

[37] S. Deleanu, D. Carpenter, and M. Lau, "Determination of parameters of a synchronous motor with radial permanent magnets and rotor damper bar cage," in *2012 25th IEEE Canadian Conference on Electrical and Computer Engineering (CCECE)*, 2012, pp. 1-6: IEEE.

[38] F. Fernández Bernal, A. Garcia Cerrada, and R. Faure, "Model-based loss minimization for DC and AC vector-controlled motors including core saturation," *IEEE Transactions on industry Applications,* vol. 36, no. 3, pp. 755-763, 2000.

[39] S. Morimoto, Y. Tong, Y. Takeda, and T. Hirasa, "Loss minimization control of permanent magnet synchronous motor drives," *IEEE Transactions on industrial electronics,* vol. 41, no. 5, pp. 511-517, 1994.

[40] R. Monajemy and R. Krishnan, "Control and dynamics of constant-power-loss-based operation of permanent-magnet synchronous motor drive system," *IEEE Transactions on Industrial Electronics,* vol. 48, no. 4, pp. 839-844, 2001.

[41] U. Schaible and B. Szabados, "Dynamic motor parameter identification for high speed flux weakening operation of brushless permanent magnet synchronous machines," *IEEE Transactions on Energy Conversion,* vol. 14, no. 3, pp. 486-492, 1999.

[42] Y. Tong, S. Morimoto, Y. Takeda, and T. Hirasa, "Maximum efficiency control for permanent magnet synchronous motors," in *Proceedings IECON'91: 1991 International Conference on Industrial Electronics, Control and Instrumentation*, 1991, pp. 283-288: IEEE.

[43] A. A. Adam, "Accurate modeling of PMSM for differential mode current and differential torque calculation," in *2013 INTERNATIONAL CONFERENCE ON COMPUTING, ELECTRICAL AND ELECTRONIC ENGINEERING (ICCEEE)*, 2013, pp. 103-109: IEEE.

[44] N. Boubaker, D. Matt, P. Enrici, F. Nierlich, and G. Durand, "Measurements of Iron Loss in PMSM Stator Cores Based on CoFe and SiFe Lamination Sheets and Stemmed From Different Manufacturing Processes," *IEEE Transactions on Magnetics,* vol. 55, no. 1, pp. 1-9, 2019.

[45] N. Denis, K. Fujitani, Y. Kato, M. Ieki, and K. Fujisaki, "Core loss increase due to inverter carrier frequency in an interior permanent magnet synchronous motor," in *2015 18th International Conference on Electrical Machines and Systems (ICEMS)*, 2015, pp. 795-800: IEEE.

[46] N. Denis, M. Inoue, K. Fujisaki, H. Itabashi, and T. Yano, "Iron loss reduction in permanent magnet synchronous motor by using stator core made of nanocrystalline magnetic material," *IEEE Transactions on Magnetics,* vol. 53, no. 11, pp. 1-6, 2017.

[47] N. Denis, S. Odawara, and K. Fujisaki, "Attempt to evaluate the building factor of a stator core in inverter-fed permanent magnet synchronous motor," *IEEE Transactions on Industrial Electronics,* vol. 64, no. 3, pp. 2424-2432, 2017.

[48] N. Denis, Y. Wu, and K. Fujisaki, "Impact of the Inverter DC Bus Voltage on the Iron Losses of a Permanent Magnet Synchronous Motor at Constant Speed," *IEEJ Journal of Industry Applications,* vol. 6, no. 6, pp. 346-352, 2017.

[49] K. I. Laskaris and A. G. Kladas, "Permanent-magnet shape optimization effects on synchronous motor performance," *IEEE Transactions on Industrial Electronics,* vol. 58, no. 9, pp. 3776-3783, 2011.

[50] L. Ma, M. Sanada, S. Morimoto, and Y. Takeda, "Prediction of iron loss in rotating machines with rotational loss included," *IEEE transactions on Magnetics,* vol. 39, no. 4, pp. 2036-2041, 2003.

[51] C. Mi, G. R. Slemon, and R. Bonert, "Modeling of iron losses of permanent-magnet synchronous motors," *IEEE Transactions on Industry applications,* vol. 39, no. 3, pp. 734-742, 2003.

[52] D. Miyagi, N. Maeda, Y. Ozeki, K. Miki, and N. Takahashi, "Estimation of iron loss in motor core with shrink fitting using FEM analysis," *IEEE Transactions on Magnetics,* vol. 45, no. 3, pp. 1704-1707, 2009.

[53] Y. Okada, H. Dohmeki, and S. Konushi, "Proposal of 3D-stator structure using soft magnetic composite for PM motor," in *The XIX International Conference on Electrical Machines-ICEM 2010*, 2010, pp. 1-6: IEEE.

[54] S. Okamoto, N. Denis, Y. Kato, M. Ieki, and K. Fujisaki, "Core loss reduction of an interior permanent-magnet synchronous motor using amorphous stator core," *IEEE Transactions on Industry Applications,* vol. 52, no. 3, pp. 2261-2268, 2016.

[55] S. A. Rahman and A. M. Knight, "Performance and core loss of concentrated winding IPMSM with different core treatment," in *2014 IEEE Energy Conversion Congress and Exposition (ECCE)*, 2014, pp. 5587-5594: IEEE.

[56] G. R. Slemon and X. Liu, "Core losses in permanent magnet motors," *IEEE Transactions on Magnetics,* vol. 26, no. 5, pp. 1653-1655, 1990.

[57] N. Takahashi and D. Miyagi, "Effect of stress on iron loss of motor core," in *2011 IEEE International Electric Machines & Drives Conference (IEMDC)*, 2011, pp. 469-474: IEEE.

[58] A. Yao, T. Sugimoto, S. Odawara, and K. Fujisaki, "Core Loss Properties of a Motor With Nanocrystalline Rotor and Stator Cores Under Inverter Excitation," *IEEE Transactions on Magnetics,* no. 99, pp. 1-5, 2018.

[59] Y. Guo, J. Zhu, P. Watterson, and W. Wu, "Development of a Claw Pole Permanent Magnet Motor with Soft Magnetic Composite Core," *Australian Journal of Electrical & Electronic Engineering,* 2005.

[60] Y. Guo, J. G. Zhu, P. A. Watterson, and W. Wu, "Development of a PM transverse flux motor with soft magnetic composite core," *IEEE Transactions on Energy Conversion,* vol. 21, no. 2, pp. 426-434, 2006.

[61] M.-S. Lim, J.-H. Kim, and J.-P. Hong, "Experimental characterization of the slinky-laminated core and iron loss analysis of electrical machine," *IEEE Transactions on Magnetics,* vol. 51, no. 11, pp. 1-4, 2015.

[62] C.-W. Kim, J.-M. Kim, S.-W. Seo, J.-H. Ahn, K. Hong, and J.-Y. Choi, "core loss analysis of permanent magnet linear synchronous generator considering the 3-D flux path," *IEEE Transactions on Magnetics,* vol. 54, no. 3, pp. 1-4, 2018.

[63] K.-J. Tseng and S.-B. Wee, "Analysis of flux distribution and core losses in interior permanent magnet motor," *IEEE Transactions on Energy Conversion,* vol. 14, no. 4, pp. 969-975, 1999.

[64] J. G. Zhu and V. S. Ramsden, "Improved formulations for rotational core losses in rotating electrical machines," *IEEE Transactions on Magnetics,* vol. 34, no. 4, pp. 2234-2242, 1998.

[65] R. Lateb and J. Da Silva, "Indirect testing to determine losses of high speed synchronous permanent magnets motors," in *2014 17th International Conference on Electrical Machines and Systems (ICEMS)*, 2014, pp. 1520-1526: IEEE.

[66] S. Zhu, Y. Hu, C. Liu, and K. Wang, "Iron loss and efficiency analysis of interior PM machines for electric vehicle applications," *IEEE Transactions on Industrial Electronics,* vol. 65, no. 1, pp. 114-124, 2017.

[67] S. Xue *et al.*, "Iron loss model for electrical machine fed by low switching frequency inverter," *IEEE Transactions on Magnetics,* vol. 53, no. 11, pp. 1-4, 2017.

[68] K. Yamazaki, T. Fukuoka, K. Akatsu, N. Nakao, and A. Ruderman, "Investigation of locked rotor test for estimation of magnet PWM carrier eddy current loss in synchronous machines," *IEEE Transactions on Magnetics,* vol. 48, no. 11, pp. 3327-3330, 2012.

[69] S. Kahourzade, N. Ertugrul, and W. L. Soong, "Loss analysis and efficiency improvement of an axial-flux PM amorphous magnetic material machine," *IEEE Transactions on Industrial Electronics,* vol. 65, no. 7, pp. 5376-5383, 2017.

[70] T. Sakaue and K. Akatsu, "Stator iron loss measurement method in permanent magnet synchronous motor to remove the mechanical loss effect," in *2014 17th International Conference on Electrical Machines and Systems (ICEMS)*, 2014, pp. 3131-3135: IEEE.

[71] Z. Gmyrek and A. Cavagnino, "Influence of Punching, Welding, and Clamping on Magnetic Cores of Fractional KiloWatt Motors," *IEEE Transactions on Industry Applications,* vol. 54, no. 5, pp. 4123-4132, 2018.

[72] J. Chen, D. Wang, Y. Jiang, X. Teng, S. Cheng, and J. Hu, "Examination of Temperature-Dependent Iron Loss Models Using a Stator Core," *IEEE Transactions on Magnetics,* no. 99, pp. 1-7, 2018.

[73] A. Krings, J. Soulard, and O. Wallmark, "Influence of PWM switching frequency and modulation index on the iron losses and performance of slot-less permanent magnet motors," in *2013 International Conference on Electrical Machines and Systems (ICEMS)*, 2013, pp. 474-479: IEEE.

[74] A. Al-Timimy, P. Giangrande, M. Degano, M. Galea, and C. Gerada, "Investigation of AC Copper and Iron Losses in High-Speed High-Power Density PMSM," in *2018 XIII International Conference on Electrical Machines (ICEM)*, 2018, pp. 263-269: IEEE.

[75] A. Al-Timimy, G. Vakil, M. Degano, P. Giangrande, C. Gerada, and M. Galea, "Considerations on the effects that core material machining has on an electrical machine's performance," *IEEE Transactions on Energy Conversion,* vol. 33, no. 3, pp. 1154-1163, 2018.

[76] B. Tekgun, Y. Sozer, I. Tsukerman, P. Upadhyay, and S. Englebretson, "Core loss estimation in electric machines with flux controlled core loss tester," *IEEE Transactions on Industry Applications,* 2018.

[77] W. L. Lorimer and D. K. Lieu, "Method for measuring and characterizing core loss in a motor," *IEEE transactions on magnetics,* vol. 35, no. 4, pp. 2146-2151, 1999.

[78] M. Veigel, P. Winzer, J. Richter, and M. Doppelbauer, "New FPGA-based and inline-capable measuring method for the identification of magnetic losses in electrical steel," in *2015 5th International Electric Drives Production Conference (EDPC)*, 2015, pp. 1-6: IEEE.

[79] M. Veigel, A. Krämer, G. Lanza, and M. Doppelbauer, "Investigation of the impact of production processes on iron losses of laminated stator cores for electric machines," in *2016 IEEE Energy Conversion Congress and Exposition (ECCE)*, 2016, pp. 1-5: IEEE.

[80] Y. Guo, J. Zhu, P. Watterson, W. Holliday, and W. Wu, "Improved design and performance analysis of a claw pole permanent SMC motor with sensorless brushless DC drive," in *The Fifth International Conference on Power Electronics and Drive Systems, 2003. PEDS 2003.*, 2003, vol. 1, pp. 704-709: IEEE.

[81] A. G. Jack, B. C. Mecrow, C. P. Maddison, and N. A. Wahab, "Claw pole armature permanent magnet machines exploiting soft iron powder metallurgy," in *1997 IEEE International Electric Machines and Drives Conference Record*, 1997, pp. MA1/5.1-MA1/5.3: IEEE.

[82] R. Blissenbach, G. Henneberger, U. Schäfer, and W. Hackmann, "Development of a transverse flux traction motor in a direct drive system," in *International conference on electrical machines*, 2000, pp. 1457-1460.

[83] Y. Chen and P. Pillay, "Axial-flux PM wind generator with a soft magnetic composite core," in *Fourtieth IAS Annual Meeting. Conference Record of the 2005 Industry Applications Conference, 2005.*, 2005, vol. 1, pp. 231-237: IEEE.

[84] A. Jack, B. Mecrow, and C. Maddison, "Combined radial and axial permanent magnet motors using soft magnetic composites," 1999.

[85] J. Cros, P. Viarouge, Y. Chalifour, and J. Figueroa, "A new structure of universal motor using soft magnetic composites," *IEEE Transactions on Industry Applications,* vol. 40, no. 2, pp. 550-557, 2004.

[86] A. Jack, B. Mecrow, P. Dickinson, P. Jansson, and L. Hultman, "Design and testing of a universal motor using a soft magnetic composite stator," in *Conference Record of the 2000 IEEE Industry Applications Conference. Thirty-Fifth IAS Annual Meeting and World Conference on Industrial Applications of Electrical Energy (Cat. No. 00CH37129)*, 2000, vol. 1, pp. 46-50: IEEE.

[87] !!! INVALID CITATION !!! {Tao, 2020 #234;Ji, 2021 #235;Jikai, 2018 #236;Balamurali, 2018 #237;Yao, 2018 #239}.

[88] A. Balamurali, G. Feng, C. Lai, J. Tjong, and N. C. Kar, "Maximum efficiency control of PMSM drives considering system losses using gradient descent algorithm based on DC power measurement," *IEEE Transactions on Energy Conversion,* 2018.

[89] Jikai *et al.*, "Analysis of temperature field for a surface-mounted and interior permanent magnet synchronous motor adopting magnetic-thermal coupling method," *CES Trans. on Electrical Machines and Systems,* vol. 2, no. 1, p. 9, 2018.

[90] D. Tao *et al.*, "Magnetic field characteristics and stator core losses of high-speed permanent magnet synchronous motors," *Energies,* vol. 13, no. 3, 2020.

[91] W. Ji, F. Ni, D. Gao, S. Luo, Q. Lv, and D. Lv, "Electromagnetic design of high-power and high-speed permanent magnet synchronous motor considering loss characteristics," *Energies,* vol. 14, no. 12, 2021.

[92] Y. Zhang, Y. Liu, Y. Li, D. Xie, and B. Bai, "A complex-valued rotating magnetic property model and its application to iron core loss calculation," *IEEE Transactions on Magnetics Mag,* vol. 50, no. 2, pp. 397-400, 2014.

[93] S. Urata, M. Enokizono, T. Todaka, and H. Shimoji, "Magnetic characteristic analysis of the motor considering 2-D vector magnetic property," *IEEE TRANSACTIONS ON MAGNETICS MAG,* vol. 42, no. 4, pp. p.615-618, 2006.

[94] X. Zhao, H. Xu, Y. Li, L. Zhou, and D. Yuan, "Improved Preisach model for vector hysteresis property of soft magnetic composite materials based on the hybrid technique of SA-NMS," *IEEE Transactions on Industry Applications,* vol. PP, no. 99, pp. 1-1, 2021.

[95] Y. Guo, J. Zhu, H. Lu, Z. Lin, and Y. Li, "Core loss calculation for soft magnetic composite electrical machines," *IEEE Transactions on Magnetics,* vol. 48, no. 11, pp. 3112-3115, 2012.

[96] M. Gyimesi and D. Ostergaard, "Inductance computation by incremental finite element analysis," *IEEE Transactions on Magnetics,* vol. 35, no. 3, pp. P.1119-1122, 1999.

[97] Y. G. Guo, J. G. Zhu, and H. Y. Lu, "Accurate determination of parameters of a claw-pole motor with SMC stator core by finite-element magnetic-field analysis," *Electric Power Applications, IEE Proceedings -,* vol. 153, no. 4, pp. 568-574, 2006.

[98] Y. Guo, "Development of low cost high performance permanent magnet motors using new soft magnetic composite materials

" Doctor of Philosophy, Electrical Engineering, University of Technology Sydney, 2003.

[99] R. S. Dastjerdi, M. A. Abbasian, H. Saghafi, and M. H. Vafaie, "Performance improvement of permanent-magnet synchronous motor using a new deadbeat-direct current controller," *IEEE Transactions on Power Electronics,* vol. 34, no. 4, pp. 3530-3543, 2019.

[100] X. Zhang, B. Hou, and Y. Mei, "Deadbeat predictive current control of permanent-magnet synchronous motors with stator current and disturbance observer," *IEEE Transactions on Power Electronics,* vol. 32, no. 5, pp. 3818-3834, 2017.

[101] L. Springob and J. Holtz, "High-bandwidth current control for torque-ripple compensation in PM synchronous machines," *IEEE Transactions on Industrial Electronics,* vol. 45, no. 5, pp. 713-721, 1998.

[102] Y. Guo, J. Zhu, H. Lu, Y. Li, and J. Jin, "Core loss computation in a permanent magnet transverse flux motor with rotating fluxes," *IEEE Transactions on Magnetics,* vol. 50, no. 11, pp. 1-4, 2014.

[103] X. Ba, Z. Gong, Y. Guo, C. Zhang, and J. Zhu, "Development of equivalent circuit models of permanent magnet synchronous motors considering core loss," *Energies,* vol. 15, no. 6, 2022.

[104] B. Dianati, S. Kahourzade, and A. Mahmoudi, "Optimization of axial-flux induction motors for the application of electric vehicles considering driving cycles," *IEEE Transactions on Energy Conversion,* vol. 35, no. 3, pp. 1522-1533, 2020.

[105] J. Mei, Y. Zuo, C. H. T. Lee, and J. L. Kirtley, "Modeling and optimizing method for axial flux induction motor of electric vehicles," *IEEE Transactions on Vehicular Technology,* vol. 69, no. 11, pp. 12822-12831, 2020.

[106] J. Zhu, K. W. E. Cheng, X. Xue, and Y. Zou, "Design of a new enhanced torque in-wheel switched reluctance motor with divided teeth for electric vehicles," *IEEE Transactions on Magnetics,* vol. 53, no. 11, pp. 1-4, 2017.

[107] X. Sun, K. Diao, G. Lei, Y. Guo, and J. Zhu, "Study on segmented-rotor switched reluctance motors with different rotor pole numbers for BSG system of hybrid electric vehicles," *IEEE Transactions on Vehicular Technology,* vol. 68, no. 6, pp. 5537-5547, 2019.

[108] A. Credo, G. Fabri, M. Villani, and M. Popescu, "Adopting the topology optimization in the design of high-speed synchronous reluctance motors for electric vehicles," *IEEE Transactions on Industry Applications,* vol. 56, no. 5, pp. 5429-5438, 2020.

[109] G. V. Kumar, C. H. Chuang, M. Z. Lu, and C. M. Liaw, "Development of an electric vehicle synchronous reluctance motor drive," *IEEE Transactions on Vehicular Technology,* vol. 69, no. 5, pp. 5012-5024, 2020.

[110] J. Wang, X. Yuan, and K. Atallah, "Design optimization of a surface-mounted permanent-magnet motor with concentrated windings for electric vehicle applications," *IEEE Transactions on Vehicular Technology,* vol. 62, no. 3, pp. 1053-1064, 2013.

[111] L. Dang, N. Bernard, N. Bracikowski, and G. Berthiau, "Design optimization with flux weakening of high-speed PMSM for electrical vehicle considering the driving cycle," *IEEE Transactions on Industrial Electronics,* vol. 64, no. 12, pp. 9834-9843, 2017.

[112] X. Sun, Z. Shi, G. Lei, Y. Guo, and J. Zhu, "Analysis and design optimization of a permanent magnet synchronous motor for a campus patrol electric vehicle," *IEEE Transactions on Vehicular Technology,* vol. 68, no. 11, pp. 10535-10544, 2019.

[113] M. Kimiabeigi *et al.*, "High-performance low-cost electric motor for electric vehicles using ferrite magnets," *IEEE Transactions on Industrial Electronics,* vol. 63, no. 1, pp. 113-122, 2016.

[114] X. Zhu, X. Wang, C. Zhang, L. Wang, and W. Wu, "Design and analysis of a spoke-type hybrid permanent magnet motor for electric vehicles," *IEEE Transactions on Magnetics,* vol. 53, no. 11, pp. 1-4, 2017.

[115] Y. Jung, M. Park, and M. Lim, "Asymmetric rotor design of IPMSM for vibration reduction under certain load condition," *IEEE Transactions on Energy Conversion,* vol. 35, no. 2, pp. 928-937, 2020.

[116] X. Liu, H. Chen, J. Zhao, and A. Belahcen, "Research on the performances and parameters of interior PMSM used for electric vehicles," *IEEE Transactions on Industrial Electronics,* vol. 63, no. 6, pp. 3533-3545, 2016.

[117] D. G. Dorrell, M. Hsieh, and A. M. Knight, "Alternative rotor designs for high performance brushless permanent magnet machines for hybrid electric vehicles," *IEEE Transactions on Magnetics,* vol. 48, no. 2, pp. 835-838, 2012.

[118] X. Sun, M. Wu, G. Lei, Y. Guo, and J. Zhu, "An improved model predictive current control for PMSM drives based on current track circle," *IEEE Transactions on Industrial Electronics,* vol. 68, no. 5, pp. 3782-3793, 2021.

[119] C. Ma *et al.*, "Analytical calculation of no-load magnetic field of external rotor permanent magnet brushless direct current motor used as in-wheel motor of electric vehicle," *IEEE Transactions on Magnetics,* vol. 54, no. 4, pp. 1-6, 2018.

[120] Y. Liu, L. Li, Q. Gao, J. Cao, and Z. Sun, "An analytical model and optimization of a novel hybrid rotor machine for high torque density," *IEEE Transactions on Energy Conversion,* vol. 36, no. 1, pp. 230-241, 2021.

[121] B. N. Cassimere, S. D. Sudhoff, and D. H. Sudhoff, "Analytical design model for surface-mounted permanent-magnet synchronous machines," *IEEE Transactions on Energy Conversion,* vol. 24, no. 2, pp. 347-357, 2009.

[122] S. Zhu, M. Cheng, W. Hua, X. Cai, and M. Tong, "Finite element analysis of flux-switching PM machine considering oversaturation and irreversible demagnetization," *IEEE Transactions on Magnetics,* vol. 51, no. 11, pp. 1-4, 2015.

[123] W. Zhao, F. Xing, X. Wang, T. A. Lipo, and B. Kwon, "Design and analysis of a novel PM-assisted synchronous reluctance machine with axially integrated magnets by the finite-element method," *IEEE Transactions on Magnetics,* vol. 53, no. 6, pp. 1-4, 2017.

[124] F. Marignetti, V. D. Colli, and Y. Coia, "Design of axial flux PM synchronous machines through 3-D coupled electromagnetic thermal and fluid-dynamical finite-element analysis," *IEEE Transactions on Industrial Electronics,* vol. 55, no. 10, pp. 3591-3601, 2008.

[125] D. M. Ionel and M. Popescu, "Ultrafast finite-element analysis of brushless PM machines based on space–time transformations," *IEEE Transactions on Industry Applications,* vol. 47, no. 2, pp. 744-753, 2011.

[126] G. Bertotti, "General properties of power losses in soft ferromagnetic materials," *ieee trans magn,* 1988.

[127] M. I. Dan, M. Popescu, M. I. Mcgilp, T. Miller, and R. J. Heideman, "Computation of core losses in electrical machines using improved models for laminated steel," *IEEE Transactions on Industry Applications,* vol. 43, no. 6, pp. 1554-1564, 2007.